The Design and Construction of a Bulge Testing Device Platform for Human Skin Tissue Applications

Dustin Fischer

Dissertation presented in partial fulfilment of the requirements

of the degree of Master of Science

Blast Impact and Survivability Research Unit

Department of Mechanical Engineering

University of Cape Town

September 2020

Plagiarism Declaration

I know the meaning of plagiarism and declare that all the work in the document, save for that which is properly acknowledged, is my own. This thesis/dissertation has been submitted to the Turnitin module (or equivalent similarity and originality checking software) and I confirm that my supervisor has seen my report and any concerns revealed by such have been resolved with my supervisor.

Signed on 10 September 2020

Signed by candidate

Dustin Fischer

Abstract

Limited standard mechanical testing practises and stress-strain data are available for anisotropic human skin tissue in biaxial loading configurations to suitably represent skin *in vivo*. Inconsistencies in mechanical and physical properties in the literature due to numerous physiological factors have restricted development of biaxial testing equipment in laboratories to *ad hoc* research solutions having limited modifiability and parametric control. This project aims to develop a biaxial tensile testing device and testing platform which can be used in a research laboratory setting to provide a springboard to expediate mechanical skin tissue testing. The device can be easily reconfigured to accommodate a range of bulge pressures, while being driven via a 10bar compressed air supply.

Based on simplified modelling of skin as an elastomer, mechanical and pneumatic resistive-capacitive pressure vessel models are developed. These are used respectively to initially specify a modifiable piston-cylinder bulge testing apparatus, and to design a customisable discrete proportional-integral closed-loop feedback pressurisation rate control system and software control environment. Pressure-time histories were successfully collected and stored on a dedicated computer for silicone sheet samples of 50mm diameter, as a surrogate for skin, that were tested using the platform to maximum pressures of about 200 kPa, at rates set between 2 – 20 kPa/s. The efficacy of the rate control system was affected by resolution of discrete pressurisation components that were used. The described platform is currently suitable for controlled and measured bulge pressurisation of elastomers. It is recommended to extend facility of the current platform by integrating 3D imaging and measurement technologies, to evaluate deformation of bulged anisotropic skin tissue and map inhomogeneous stress-strain fields for complex tensile stress-strain evaluations.

Acknowledgements

To my parents, thank you for your interminable and unconditional love and support. You have imparted in me your immense strength and resilience. You have provided me with the major advantages that I have gained in life.

Thank you to my project supervisor, Dr. Reuben Govender, for your constant support and navigation throughout this challenging journey.

To Martin, thank you for showing me how to embrace inner strength, and for supporting me to the very end of my postgraduate journey.

To Sherlyn, thank you for the long talks, sage advice, and kicks-in-the-pants that I needed on so many occasions.

Thank you to my mentors and colleagues at the Blast Impact and Survivability Research Unit at the University of Cape Town. Good luck with every success in life.

I would like to thank everyone who has afforded me their support, time, wisdom, and/or encouragement during this dissertation.

Dustin Fischer

Contents

Figures

Tables

Abbreviations

Abbreviation	Description
1D	One Dimensional
3D	Three Dimensional
ADC	Analog to Digital Convertor
CMD	Command
DAC	Digital to Analog Converter
DC	Direct Current
DIC	Digital Image Correlation
EPR	Electronic Pressure Regulator
GUI	Graphical User Interface
I/O	Input / Output
ISR	Interrupt Service Routine
K	Proportional gain
MCU	Micro Controller Unit
P	Proportional (control)
PC	Personal Computer
PCB	Printed Circuit Board
PI	Proportional-Integral (control)
PID	Proportional-Integral-Derivative (control)
RC	Resistive Capacitive
Ref	Reference
SS	Steady state
τ	RC time constant
UART	Universal Asynchronous Receiver/Transmitter
UTS	Ultimate Tensile Strength

Chapter 1

Introduction

Human skin is the largest organ in the human body, which provides a critical interface barrier for potential environmental, chemical, pollutant, projectile, and many other intrusions to the human body. It stands to reason then that skin, as a mechanical material, would be well studied and understood for predicting its loaded mechanical response. However, there exists a stark gap in the wealth of catalogued data and information describing the mechanical characteristics and properties of human skin tissue. A major contributing factor is a lack of standard material testing procedures for membranous skin tissue (and planar elastomeric materials in general) experiencing large deformations. Militaries, research institutions, and defence and automotive industries have interests in developing skin simulants with realistic compliance, enabling them to study and predict the transmission of blunt force trauma using more realistic test dummies [1]. Continual improvement of computational biomechanical models and skin simulations in its contribution to a complete human body predictive models are of particular interest to the current broader research goals of the Blast Impact and Survivability Unit (BISRU) at the University of Cape Town.

Numerical modelling of elastomers provides a mechanism for mechanical characterisation by fitting experimental data to mathematical models. Uniaxial tensile testing is a fundamental and popular method for collecting data to fit such models, for isotropic materials such as engineering metals. Realistically skin tissue is not likely to be loaded uniaxially, rather skin is more likely to be loaded biaxially *in situ*. Model parameters obtained using uniaxial data only are insufficient to describe an elastomeric material undergoing large deformations in complex

loading configurations. To properly describe incompressible rubber-like materials, a combination of uniaxial and biaxial tensile data is required. From this, a more representative estimation of realistic complex loading model parameters may be obtained for modelling purposes. For example ABAQUS, a popular numerical modelling software, provisions and promotes including a combination of uniaxial and biaxial tensile stress-strain data so that it may better estimate elastomeric model parameters [2].

Biaxial mechanical testing for most materials is not well standardised as it is for uniaxial testing. This leads to most instances of its use in research being performed using *ad hoc* solutions. It was therefore advantageous, in a research laboratory environment context, to develop an in-house testing device and testing platform that could structure internal instrumentation and testing procedures. While alternative contemporary biaxial testing methods such as planar testing exist, the bulge testing technique which infers mechanical properties of a material by inflating a material specimen, was considered for this project.

1.1 Scope

The purpose of this project was to create a pressure loading rate configurable bulge testing device and testing platform which would pose minimal start up development time for future research applications involving skin tissue tensile testing. The platform was intended to be used as a slow to mid-range rate device which could be used to produce biaxial stress-strain data for materials experiencing large deformations. Rate control is provisioned for the platform design in this report and is presented as a design feature only. The rate control facility was not used to investigate material rate dependency in any capacity in the context of this report.

The design and intended application of the device and platform presented in this report is for use with human skin tissue, but due to ethical approval and material sourcing barriers, skin tissue was not tested. The potential for use of the bulge testing device extends past skin to elastomeric materials in general. For this project, only isotropic synthetic elastomer materials were intended to be tested, for the purposes of developing the platform to a point where it may be useful to subsequently advance to skin tissue applications.

1.2 Report Outline

This report is ordered primarily chronologically. The nature of the project was to design, construct, and evaluate both a mechanical bulge testing apparatus and an associated testing platform. The report presents the major individual systems and subsystems and components which were developed throughout the project in order to fulfil the intended aim. The brief content of the report is presented as follows:

- Chapter 2 Literature Review:

  Discusses the studied mechanical behaviour of skin tissue, presents the historical and contemporary state-of-the-art for biaxial testing of skin tissue, and reviews feedback control system design techniques fort rate control applications.

- Chapter 3 Mechanical System Design:

  Describes the initial specification modelling of the mechanical requirements for the bulge testing apparatus, and subsequent concept development and design of a pneumatically driven piston-cylinder bulge testing apparatus.

- Chapter 4 Feedback Control System Design:

  Presents a discrete proportional-integral feedback control system design strategy which was employed to track a constant bulge-pressure pressurisation rate.

- Chapter 5 Instrumentation and Controls:

  Outlines the actuation and sensor instrumentation which were used and integrated, as well as touches on the necessary electronic circuitry interfaces. The automation software control system architecture and implementation are also briefly discussed.

- Chapter 6 Platform Testing and Evaluation:

  Presents results of tests which were performed to assess the efficacy of the feedback control system design, and to assess the potential ability of the platform to obtain stress-strain data for an elastomeric material.

- Chapter 7 Conclusions:

  Summarises the performance of the bulge testing apparatus and testing platform and recommends improvements and suggestions for future research and development of the bulge testing platform.

Discussion and analysis are presented at the end of each chapter, where relevant, as this afforded a more logical flow of the decision making related to each subsystem.

Chapter 2

Literature Review

Human skin tissue is a complex, non-uniform soft connective tissue whose mechanical characteristics and properties have been subject to investigation for well over 100 years [3].

This chapter presents some of the literature which has been reviewed that describes the nature of skin both in physical structure, and as a material whose response requires non-trivial modelling. The physical structure and characteristic mechanical properties of skin tissue are presented first. The significance and application of biaxial mechanical testing methods for characterising soft elastic materials and biological tissues is reviewed in subsequently.

A common characteristic of many soft elastomeric materials is rate dependency which often requires controlled parametric sensitivity study and was required of the bulge testing device developed in this report. Finally, a brief review of the control theory and methodology for feedback control system design for settable parameter control is included.

2.1 Structure of Human Skin Tissue

The biomechanics of human skin are closely linked with the microstructural composition of the tissue. Human skin is a stratified soft connective tissue which is composed of three distinguishable layers being the epidermis, dermis, and hypodermis [4]. The epidermis is the thin outer layer of the skin which acts as the external permeability layer and protrusion barrier, as well as being an interfacial surface for regulatory functions such as thermal regulation and cellular regeneration. The adjacent dermis is a blood rich, fibre dense layer

from which skin gains most of its mechanical strength and elasticity. The combined epidermis and dermis (a.k.a. the cutis) average thickness has been found to be somewhere in the range of 1.5 – 2.6mm [5], varying most significantly with anatomical site. The underlying hypodermis is an interfacial layer which stores fatty tissue. The relevant microstructure of skin is illustrated in Figure 2-1.

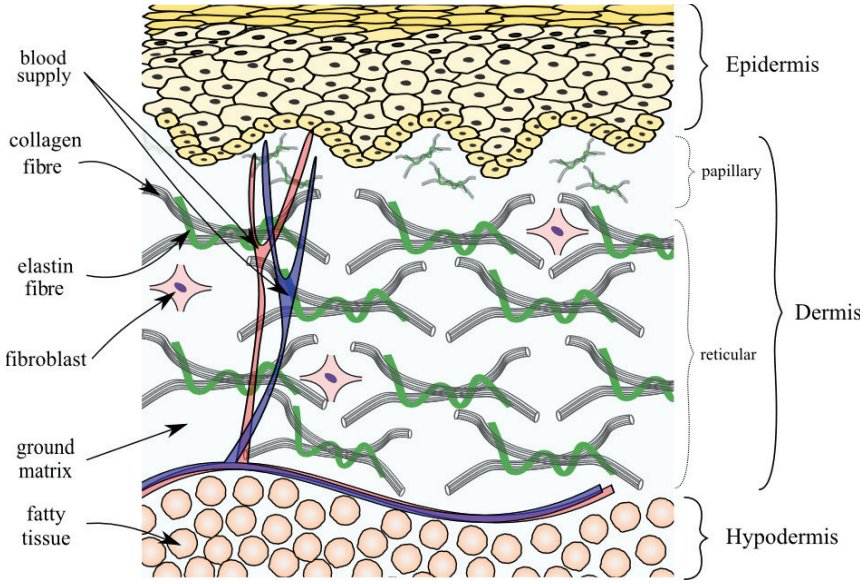

Figure 2-1: Microstructure of human skin tissue. Produced from information reported in [4]

Collagen is the most abundant extracellular protein found throughout the body, present extensively throughout the dermis. Collagen is a strong, stiff fibrillar bundled fibre which provides skin with high tensile strength. Elastin is a highly compliant, less abundant protein fibre which is also present in the dermis, found interwoven between the collagen fibre bundles to form complex fibre networks. Elastin has been attributed with retaining the undeformed shape of skin [6].

Collagenous fibre networks are found densely packed throughout the reticular dermal sublayer of skin. Collagen has been observed to be preferentially planar, oriented on average horizontally parallel to the surface with apparently random packing [7]. Penetrative studies have suggested a more regular resultant lattice network (for example [8]). A finer fibre network is present nearer to the epidermal interface in the papillary sublayer, which is primarily a region for terminating of capillaries and nutritive supply to surrounding cells.

The dermal fibre networks are contained within a hydrophilic proteinous ground substance matrix which provides hydration and lubrication to the fibres and surrounding tissue. The bulk volume of the ground substance comprises of water, making skin essentially incompressible. Collagen and the ground substance are formed by fibroblast cells in the dermis.

2.2 Mechanical Characteristics of Skin Tissue

2.2.1 Tensile Stress-Strain Response

The general stress-strain behaviour of skin tissue has been well established in terms of fibrous reactions to load. The typical nonlinear 'J-shape' elastic stress-strain response for skin tissue under axial tensile load is shown in Figure 2-2.

Daly (1982) [9] reported that stiffness increases with increasing load and strain, occurring in three stages related to the unbundling of initially randomly oriented 'coiled' collagen fibre bundles (Figure 2-2 region A). Oxlund et. al. [6] attributed the loading of elastin fibres in this region to the high initial compliance observed. Further loading gradually straightens and aligns the collagen fibres in the direction of loading (seen in the 'toe region' of Figure 2-2 B), until fully straightened and aligned with the load to fully support it (Figure 2-2 C). Frankel et. al. [10] reported collagen fibres breaking at extensions of approximately 10%, and elastic fibres at extensions of 200%.

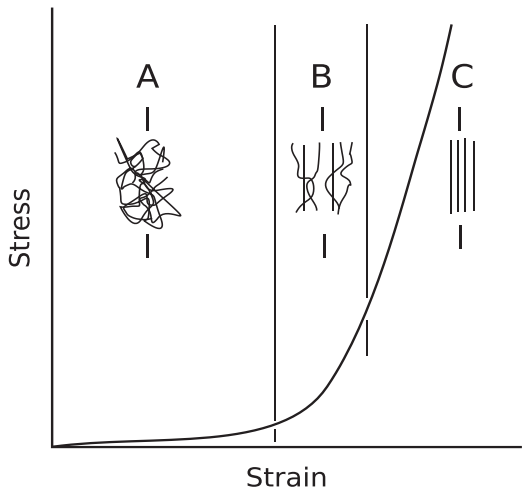

Figure 2-2: Typical J-shape stress-strain response for skin tissue in axial tension. Image reproduced from [9]

2.2.2 Anisotropy

Skin tissue exhibits anisotropic mechanical behaviours which have been attributed to the fibrous constitution of the material. Human skin tissue is in tension in vivo, found with varying preferential orientation at different anatomical sites due to natural alignment of the collagen fibres. The earliest topological mappings of these orientations across the human body, commonly referred to as Langer's lines, were produced by Karl Langer (1861) [3] by puncturing skin tissue with a circular awl and observing the directionality of the resultant elliptical cleft.

Ridge et. al. (1966) [8] postulated a theoretical two-dimensional collagen lattice structure with a mean fibre angle less than 45° to visualise and interpret directionally dependent behaviours observed for skin tissue (see Figure 2-3). Samples cut and loaded parallel to the preferred orientation of the collagen lattice experience higher stresses at lower strains than those cut and loaded perpendicularly as illustrated in Figure 2-3. Skin specimens loaded in these configurations will ultimately exhibit equal initial and final stiffnesses but occurring at different comparative strains [9].

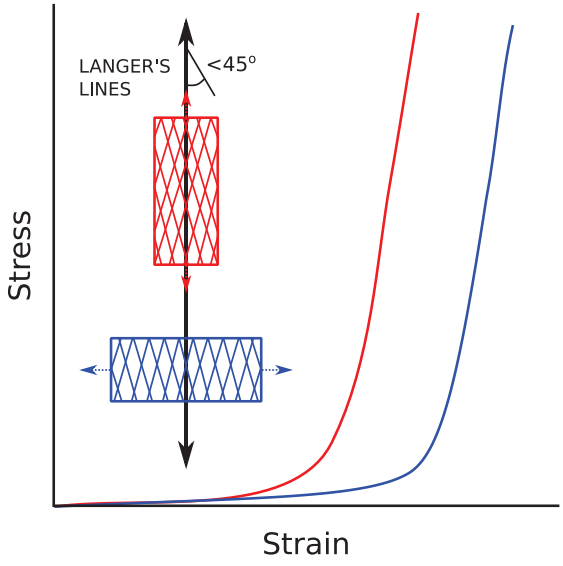

Figure 2-3: Anisotropic mechanical response for skin tissue loaded parallel and perpendicular to the preferred fibre network orientation. Adapted from images produced in [8], [9]

2.2.3 Viscoelasticity

Skin tissue (and collagenous soft tissue in general) has been shown to exhibit viscoelastic mechanical behaviours. These have largely been attributed to interactions between collagen fibrils and fibre mesh interactions with the containing ground substance matrix and fluidic cellular components [9], [11]–[13].

Hysteresis in the axial loading and unloading strain paths has been observed with viscoelastic interactions in skin tissue. In addition to single cycle hysteresis, skin tissue is also subject to preconditioning in which cyclic loading and unloading manifest along different return paths until a repeatable response may be obtained [6],[8]. The hysteresis and preconditioning phenomena are illustrated in Figure 2-4. Liu et. al. [12] investigated preconditioning of pig skin tissue in uniaxial tension which showed that the number of required uniaxial preconditioning cycles was related to the collagen content and original fibre orientation.

Shergold *et. al.* [15] and Zhou *et. al.* [11] investigated the strain rate dependency of pig skin tissue stiffness in uniaxial compression and tension. Both studies observed a significant increase in stiffness with increasing strain rate.

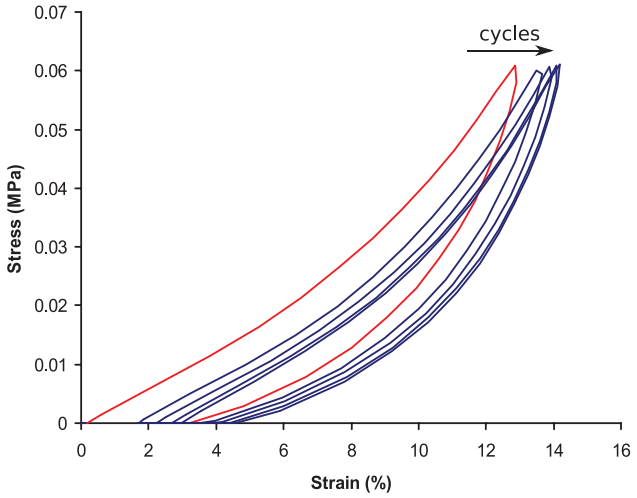

Figure 2-4: Typical hysteresis loop (red) and preconditioning (all) observed in (porcine) skin at low strains. Adapted from images produced in [12]

2.2.4 Uniaxial Tensile Properties

Comprehensive mechanical property data for human skin is lacking in the literature, due to limited availability of material for testing *in vitro*. The subsequent absence of standardised test methods for soft tissues, and inherent variability between test subjects, leads to a lack of consistency. Shown in Table 2-1 is a summary of some of the salient mechanical property data which was found in the literature. For the context of this report, the data shown is limited to quasistatic uniaxial tensile data obtained from in vitro experimental testing.

The property data given vary significantly both intra-study and inter-study. The dependency of the mechanical properties of skin with age, location on the body, loading and fibre orientations [16], [17], as well as many other physiological and experimental factors contribute to the large inconsistencies encountered throughout the literature.

Table 2-1: Summary of the mechanical properties found in literature for human skin in quasistatic uniaxial tension

Source		Elastic Modulus (MPa)		UTS (MPa)	Final Stretch (-)
		Initial	Final		
Annaidh et.	[17]	0.98 – 1.63	58.2 – 93.3	12.6 – 24.0	1.5 – 1.65
Edwards et.	[18]	-	15.0 – 150.0	5.0 – 30.0	1.4 – 2.2
Ottenio et. al.	[19]	-	76.7 ± 40.3	15.9 ± 5.7	1.5 ± 0.1
Silver et. al.	[20]	0.1	18.8	-	-

2.2.5 Mechanical Characterisation of Soft Elastic Materials

Most approaches to modelling the mechanical characteristics of skin found in the literature treat skin as an incompressible elastomeric material whose mechanical behaviour can be described by a strain energy density function. Numerous models for collagenous soft tissues based on strain energy have been developed, to various degrees of complexity, to model nonlinear orthotropic or anisotropic behaviours with fibrous descriptions.

Isotropic models have been used throughout the literature to replicate experimental mechanical responses of biological skin tissue in biaxial loading to give an estimated equibiaxial response [15], [21]–[24]. The use of isotropic strain energy models is also

particularly useful for modelling the mechanical response of synthetic polymeric materials which are treated as skin simulants, such as silicone rubber (for example [25]). This allows for simplified parameter identification for quantitative mechanical property evaluation and comparison.

2.2.6 Hyperelastic Material Description

The nonlinear finite strain theory presented in this section is well established; the information presented is unpacked in detail in [26]. An isotropic hyperelastic material is defined with a scalar strain energy density function W which depends upon the principal stretch invariants I_{1-3} only, such that

$$W = W(I_1, I_2, I_3) \tag{2.1}$$

Here, I_{1-3} are the principal strain invariants of the Cauchy-Green deformation tensors where

$$I_1 = \lambda_1^2 + \lambda_2^2 + \lambda_3^2 \tag{2.2}$$

$$I_2 = \lambda_1^2\,\lambda_2^2 + \lambda_2^2\,\lambda_3^2 + \lambda_3^2\,\lambda_1^2 \tag{2.3}$$

$$I_3 = \lambda_1^2\,\lambda_2^2\,\lambda_3^2 \tag{2.4}$$

in which λ_{1-3} are the stretches in the principal directions.

For an incompressible (implying $I_3 = 1$) isotropic hyperelastic material it follows that

$$W = W(I_1, I_2) \tag{2.5}$$

where the principal (Cauchy) stress tensor is given by

$$\boldsymbol{\sigma} = -p\mathbf{1} + 2\frac{\partial W}{\partial I_1}\boldsymbol{B} - 2\frac{\partial W}{\partial I_2}\boldsymbol{B} \tag{2.6}$$

where $\boldsymbol{p}$ is an arbitrary hydrostatic pressure and $\boldsymbol{B}$ is the left Cauchy-Green deformation tensor. The principal Cauchy stresses components for an incompressible isotropic hyperelastic material whose stress state is described by (2.6) can be written as

$$\sigma_i = -p + \lambda_i \frac{\partial W}{\partial \lambda_i} \;\; | \;\; i = \{1, 2, 3\} \tag{2.7}$$

2.2.7 Common Hyperelastic Models

Mooney-Rivlin Isotropic Hyperelastic Model

The Mooney-Rivlin strain energy density function which was first proposed by Mooney (1940) [27], and written in terms of the principal strain invariants by Rivlin (1948) [28] is given as

$$W(\bar{I}_1, \bar{I}_2) = C_1(\bar{I}_1 - 3) + C_2(\bar{I}_2 - 3) \tag{2.8}$$

where the isochoric terms $\bar{I}_i$ are equal to I_i for incompressible materials. The coefficients C_1 and C_2 are constants which are determined experimentally. This model remains popular for its simplicity in characterising the mechanical response for many isotropic hyperelastic materials experiencing moderately large strains.

Ogden Isotropic Hyperelastic Model

Ogden (1972) [29] proposed a more generalised model for nearly compressible hyperelastic materials which can be given in terms of the principal stretches $\lambda_i\,,\ i = 1,2,3$ as

$$W(\lambda_1, \lambda_2, \lambda_3) = \sum_{p=1}^{N} \frac{\mu_p}{\alpha_p} \left(\sum_{i=1}^{3} \lambda_i^{\alpha_p} - 3 \right) \tag{2.9}$$

where N, μ_p and α_p are experimentally determined material constants. The complexity of parameter identification increases with the number of terms used to represent the material.

Holzapfel-Gasser-Ogden Anisotropic Model

Holzapfel et. al. [30] proposed an anisotropic, planar, bidirectional fibre-reinforced composite hyperelastic strain energy model to account for collagenous fibre present in soft tissues. The incompressible strain energy density function proposed by the authors is decomposed into isotropic and anisotropic components to give

$$W(\bar{I}_1, \bar{I}_4, \bar{I}_6) = \frac{C_1}{2}(\bar{I}_1 - 3) + \frac{k_1}{2k_2} \sum_{k=4,6}^{N} \left[e^{k_2(\bar{I}_i - 1)^2} - 1 \right] \tag{2.10}$$

Here, the first term is isotropic component an is a single term Ogden (a.k.a. neo-Hookean) strain energy model. The second term is the anisotropic component where k_i are experimentally derived parameters, and $\bar{I}_4$, $\bar{I}_6$ are invariants related to the reference configuration of the fibre families.

2.2.8 Biaxial Loading Characterisation

Treloar (1944) [31] reported a comprehensive set of experimental mechanical test data for vulcanised rubber under various loading conditions. Much of the seminal work attempting to model elastomeric rubber-like materials has used this data as a benchmark for validating and comparing model performance (some notable authors being Rivlin [32], Ogden [33], and Arruda et. al. [34]). Figure 2-5 shows a reproduction of some of Treloar's experimental data which indicates an increase in stress and reduction in the ultimate strength for biaxial loading configurations. This illustrates the dependence of an elastomeric material's mechanical behaviour on the type of loading imposed.

Figure 2-6 shows the plane of principal strain invariants that contains possible deformation states for an incompressible material. Uniaxial loading represents only a single line on the plane; characterisations based solely on uniaxial tests are not likely to accurately predict mechanical response under more complex loading situations [35]. Characterisations based on biaxial data at different deformation states across the plane produce more insightful data for the complex loading behaviour of the material in developing accurate predictive models.

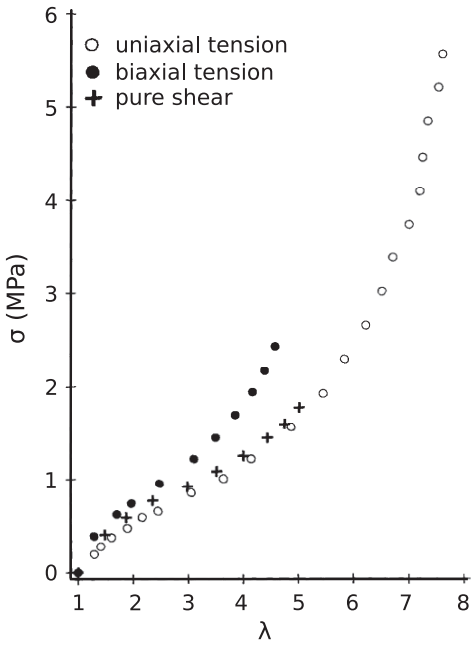

Figure 2-5: Test data reported for vulcanised rubber in different loading configurations [31]. Reproduced from [34]

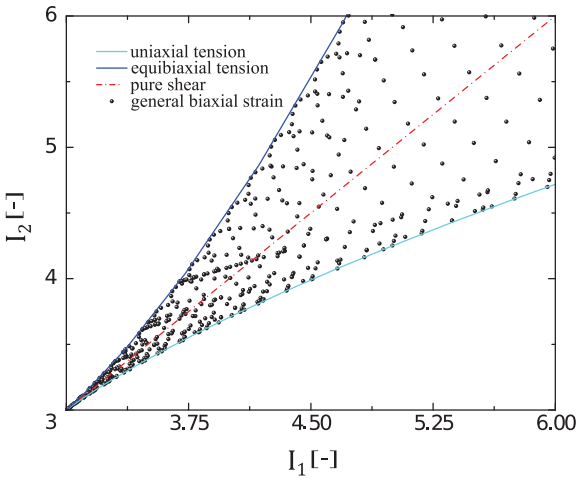

Figure 2-6: Plane of possible invariants for an incompressible material. Adapted from [36]

2.2.9 Planar Biaxial Testing

Rivlin et. al. (1951) [32] reported some of the earliest usage of square specimens for planar biaxial testing of rubber-like materials using the configuration shown in Figure 2-7. Manual biaxial load adjustments (measured via calibrated springs) on square specimens, marked with grids, were made independently through tensioned strings attached to control the consistency of the strain invariants. An exhaustive investigation into the dependency of the hyperelastic strain energy function partial components $\partial W/\partial I_{1,2}$ (evaluated similarly to using (2.5) and (2.6)) with the principal strain invariants indicated a coupling of the partial derivative terms; a pointer to the necessity of biaxial data for hyperelastic material characterisation.

A major advantage of the planar configuration is the capability to closely and independently control heterogeneous strain fields as was demonstrated by the work of Rivlin et. al. This has led to planar biaxial testing being a common biaxial testing method used for characterising the mechanical behaviour of isotropic hyperelastic materials.

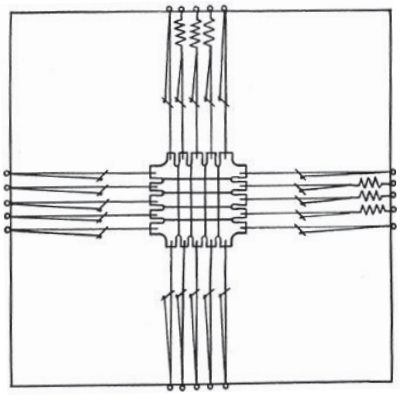

Figure 2-7: Early planar biaxial testing configuration used by Rivlin et. al. [32]

Technological advancements in automatic actuation control, transducer load measurement, and detailed deformation evaluation using monoscopic digital imaging techniques has made planar biaxial testing popular for testing hyperelastic materials. A typical modern example is shown in Figure 2-8, where planar deformation of a cruciform silicone rubber specimen is recorded with a digital camera and load is measured with load cells. In-plane strain fields are evaluated graphically using gridded point mapping in this case. A typical set of biaxial deformation states captured by planar biaxial testing is illustrated in Figure 2-8 (c).

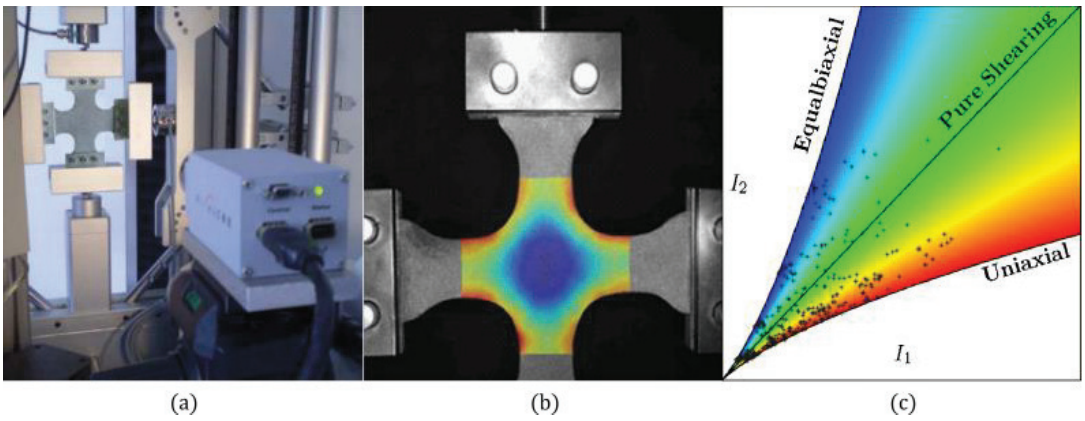

Figure 2-8: Typical modern planar biaxial test for a cruciform specimen as reported by [37] with: (load cell measurement and single camera in-plane deformation evaluation configuration; (b) a uniformly loaded specimen strain field superimposed; (c) associated deformations represented on the incompressible plane of strain invariants

Boundary conditions can be difficult to define in the region of interest for planar specimens. The traction distribution resulting from clamped edges from is not necessarily distributed

uniformly. Scrutiny of the cruciform geometry for different materials is important to ensure uniform stress and strain in the region of interest for testing [38].

2.2.10 Bulge Testing

The benchmark biaxial extension data that was reported by Treloar [31] was obtained using bulge (a.k.a. inflation) tests. These were some of the earliest reported tests (1944) which utilised the technique for testing and characterising materials experiencing large elastic deformations.

The conventional bulge testing principle is shown in Figure 2-9 (presented for a circular isotropic membrane). An undeformed clamped specimen with width and thickness $(a, t)_0$ is inflated by a pressurised medium at pressure P. In the case of earlier studies such as Treloar's, manual measurements of the vertical pole deflection h were taken to estimate the spherical radius of curvature r near the pole. The complex deformation resulting from boundary clamping, illustrated by the radial and circumferential strain characteristic shown in Figure 2-9, shows that the homogeneity of the principal stresses and strains is compromised toward the clamped boundaries.

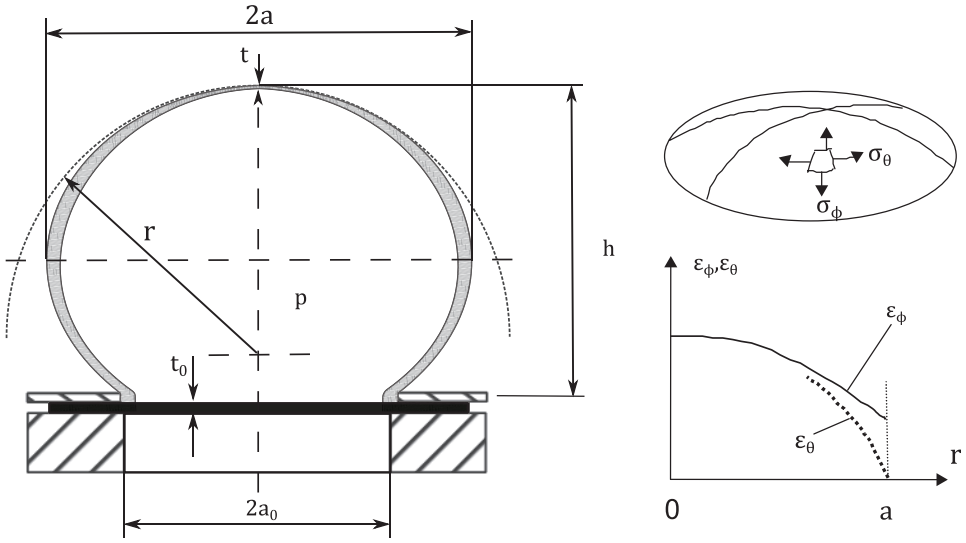

Figure 2-9: Bulge test schematic (left) adapted from [39],
(right) deviation from equibiaxiality away from the pole. Reproduced from [40]

Near the pole there is a large region of uniform spherical inflation which is in pure equibiaxial tension. Herein lies a major advantage of the bulge testing method over the planar biaxial testing method; a uniformly clamped boundary ensures a uniform distribution of the traction applied in all directions around the central region. Design and preparation of the sample geometry is therefore much simpler than is the case for planar biaxial cruciform specimens. Heterogeneous strain fields are more difficult to impose than in planar biaxial testing configurations but may be achieved using elliptical die configurations to control deformation.

Contemporary bulge testing applications for soft material testing have utilised more sophisticated instrumentation and methods for measuring load and out-of-plane deformations. Pressure load is measured ubiquitously using electronic pressure transducers. Large apex displacements for rubber materials have been measured using laser extensometers [41]. Figure 2-10 shows the more current and commonly adopted approach for measuring large out-of-plane displacement fields using stereoscopic cameras and digital image processing techniques [42].

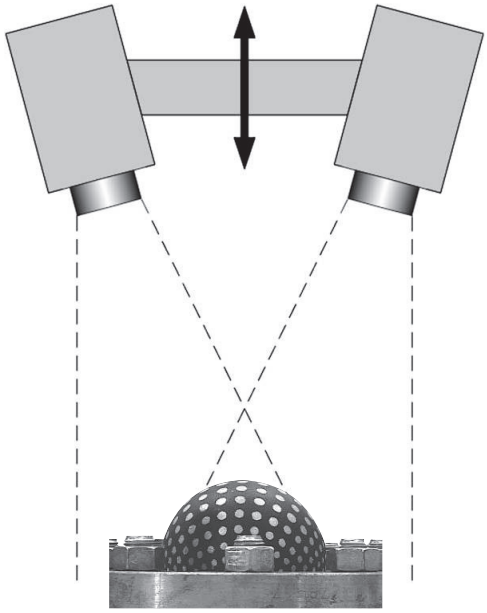

Figure 2-10: Typical modern bulge test for materials with large out-of-plane deformations recorded via stereoscopic imaging. Adapted from images presented in [42]

2.2.11 Application of Biaxial Mechanical Testing of Skin and Soft Tissues

Although skin tissue is a complex three-dimensional material, it is commonly accepted that since it can be considered almost incompressible, planar principal deformation may be used to completely describe deformation in all principal directions. Consequently, biaxial test data can be used to extrapolate fully to three-dimensional constitutive models.

Lanir and Fung (1974) [43] reported the earliest usage of a planar biaxial testing configuration to investigate the in vitro mechanical characteristics of skin tissue in biaxial tension. In the study, square rabbit skin specimens were suspended in a saline bath solution and tethered by sutured threads along all four edges. The specimens were then loaded via the threads in two mutually orthogonal directions, and forces and displacements measured. The study found that skin behaviour was orthotropic, stiffness increased slightly increasing strain rate, and that preconditioning was independent of strain rate.

The characteristics observed by Fung *et. al.* are typical of most soft planar tissues. A conventional planar biaxial testing configuration for soft planar tissues is shown in Figure 2-11. A sample is supported *in situ* by a saline bath, held at body temperature [9]. Inelastic deformations experienced during mounting and preconditioning leave the sample deformed from its original state [14].

Sacks *et. al.* [24] and Waldman et. al [44] investigated the effect of boundary conditions of clamped cruciform and tethered square soft planar tissue samples. Both studies reported significant discrepancies in material properties (specifically stiffness) based on the choice of loading attachment. Sacks et. al. concluded that tethering with threads produces the most uniform traction distribution in the region of interest. Repeatable uniform tethering may be difficult to achieve experimentally following the authors' methodology.

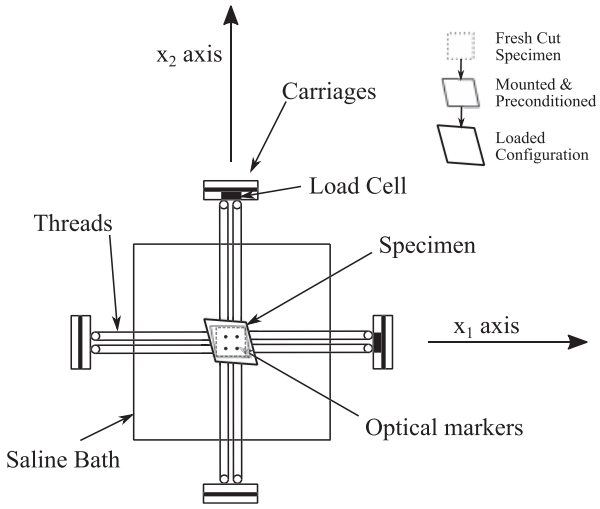

Figure 2-11: Typical planar biaxial mechanical testing configuration for soft planar tissues. Adapted from images produced in [14], [24]

Reihsner *et. al.* [16] developed a 6-axis radial loading configuration to restore in situ loading conditions to excised human skin samples as illustrated in Figure 2-12. Excised circular samples contracted elliptically after excision indicating direction of the Langer's lines. The samples were returned to their original circular configurations with careful loading at 12 independent sites around the circumference. The study found that the evaluated maximum principal in situ stresses occurred within $\pm\ 10°$ of the Langer's lines which thus coincided with the mean collagen fibre direction.

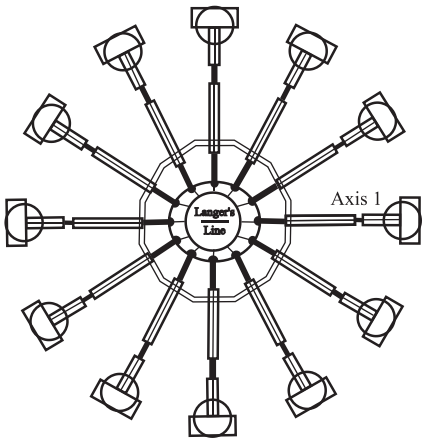

Figure 2-12: Planar testing configuration used by Reihsner *et. al.* to restore *in situ* loading conditions of excised skin samples. Image reproduced from [16]

Histological analysis of soft tissues is typically necessary to determine quantitative information about the preferred planar fibre orientations prior to uniaxial and planar tensile testing. This is necessary to obtain repeatable and comparable test result data which refer to the natural principal configuration of the fibres [45], [46].

Ziopous *et. al.* (1992) [47] used the bulge testing configuration shown in Figure 2-13 to identify the mechanical properties of soft collagenous bovine pericardium tissue. This early study used a non-destructive qualitative approach to determine the orientation of elastic symmetry in inflated specimens using moiré shadow topography. The major axis of the oval contours projected from the deformed surface coincided with the mean collagen fibre orientation.

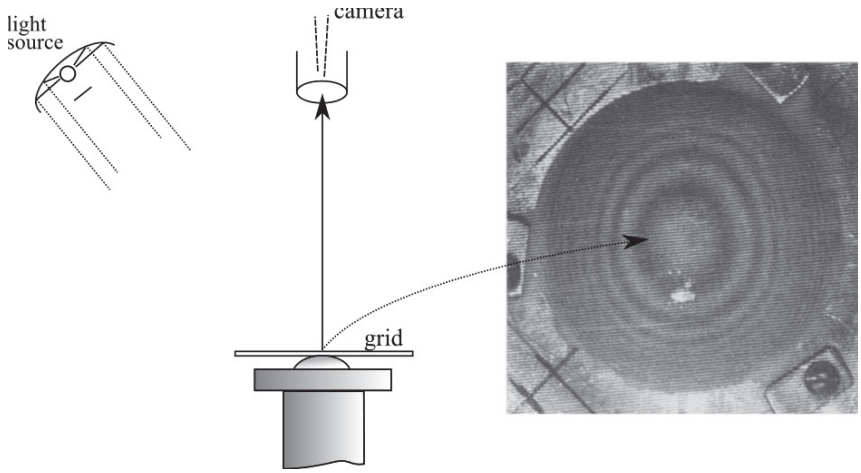

Figure 2-13: Bulge testing configuration used by Ziopous et. al. using moiré fringe projection to determine fibre orientation in bovine pericardium. Reproduced and adapted from [47]

Tonge *et. al.* (2013) [48] reported a bulge test study for human skin which also adopted optical methods to determine the mean fibre and cross-fibre orientations. The study setup was very similar to the configuration shown in Figure 2-10. Stereoscopic cameras were used to record the anisotropic ellipsoidal bulging of circular skin samples at low inflation pressures (up to 5.5 kPa). Displacement was measured using 3D Digital Image Correlation (DIC) and subsequently used to fit an ellipsoid to the deformed position. The minor and major ellipsoid axes were assumed to coincide with the mean fibre and cross-fibre orientations respectively.

A subsequent study by Tonge *et. al.* [49] which investigated human and porcine skin tissue reported negligible preconditioning effects in bulge testing configurations. This was attributed to the clamping around the entire perimeter, limiting the rearrangement of collagen fibres under load.

2.3 Feedback Control System Theory

Strain rate sensitivity of skin as discussed in (§2.2.3) motivates for the active control of deformation or loading rate in any mechanical characterisation test. Closed-loop feedback control design constitutes a significant component of this report. This section provides a brief review of some of the relevant theory and fundamental methodology for continuous and discrete feedback control system design.

2.3.1 Continuous Feedback Control System Design Background

Closed-loop negative feedback control of continuous-time signals is well established in classical control theory. The continuous-time control theory background that presented in this section (represented in the complex Laplace 's-domain') has been heavily summarised from information presented in [50].

A simple feedback control system loop with unity-gain negative feedback is illustrated in Figure 2-14. The negative feedback controller with transfer function $G_c(s)$ aims to minimize the system error $e(t) = u(t) - y(t)$ for a defined reference signal $u(t)$ and measured process output $y(t)$. The controller therefore modifies $e(t)$ to adjust the process input $c(t)$ in order to correctively adjust the system output towards the reference signal.

Feedback control system design requires *a priori* knowledge of the response dynamics of the process that is being controlled. If the process dynamics cannot be experimentally derived, the process is modelled mathematically to obtain a transfer function model $G_p(s)$ of the process. The feedback controller is designed to satisfy desirable transient and/or frequency response characteristics for the control system with estimated process dynamics. Suitable design and analysis methods such as the frequency response and/or root-locus method can be employed to adjust the system until it meets performance specifications.

Steady-state error of the controlled system, given by

$$e_{ss} = \lim_{t \to \infty} e(t) \tag{2.11}$$

is an important indicator of system performance for control system design. The magnitude of the error depends on both the nature of the reference signal $u(t)$, and the number of integrating poles N (where $s = 0 + j0$). The magnitude of the steady state error for some common reference signals is summarised in Table 2-2 in terms of the proportional gain K.

Ensuring stability during control system design is paramount. Stability implies that system outputs $y(t)$ are bounded for all bounded inputs $u(t)$. Closed-loop negative feedback response for a system with open-loop gain $L(s)$ is given by the transfer function

$$\frac{Y(s)}{U(s)} = \frac{L(s)}{1 + L(s)} \tag{2.12}$$

The system is considered stable if its closed-loop poles lie in the left-half plane in the s-domain.

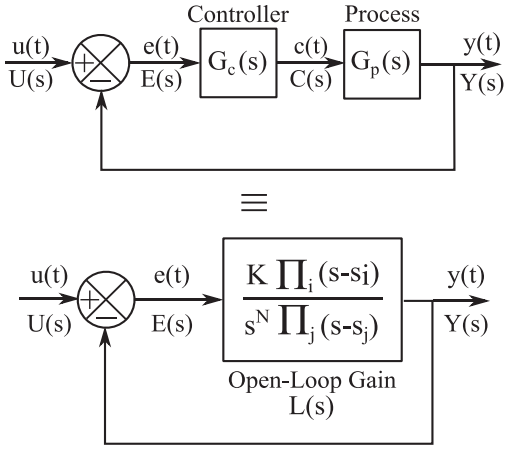

Figure 2-14: Generalised continuous negative feedback loop with unity gain

Table 2-2: Summary of unity gain feedback system steady-state error in terms of K [49]

Type (N)	**Reference Signal | $u(t)$**		
	Step (1)	Ramp (t)	Parabolic (t^2)
0	1/(1+K)	∞	∞
1	0	1/K	∞
2	0	0	**1/K**

2.3.2 Discrete Feedback Control System Design Background

Modern computerization of feedback control processes has well established discrete-time feedback control in modern control theory. The background presented has been heavily summarised from information presented in [51]. The discrete control theory (represented in

the complex sampled 'z-domain') is a continuation of the continuous control theory presented so far.

Figure 2-15 illustrates a conventional discrete-control feedback loop equivalent for the continuous feedback control system shown in Figure 2-14. Sampling of the system output at sample $[k]$ is performed by an Analog-to-Digital Converter (ADC) at a rate T (Hz). The sampled system error $e[k] = y[k] - u[k]$ is routinely evaluated by a computer. The sampled controller output $c[k]$ is converted to a continuous output signal by a Digital-to-Analog Converter (DAC). Quantization from the DAC output is modelled as a zero-order hold given by transfer function

$$G_{zoh}(s) = \frac{1 - e^{-sT}}{s} \tag{2.13}$$

Combination of the analog process $G_p(s)$ with the ADC sampling, and zero-order hold from the DAC gives a discrete transfer function equivalent for the sampled and held process

$$G_{zas}(z) = (1 - z^{-1})\, \mathcal{Z}\left\{\frac{G_p(s)}{s}\right\} \tag{2.14}$$

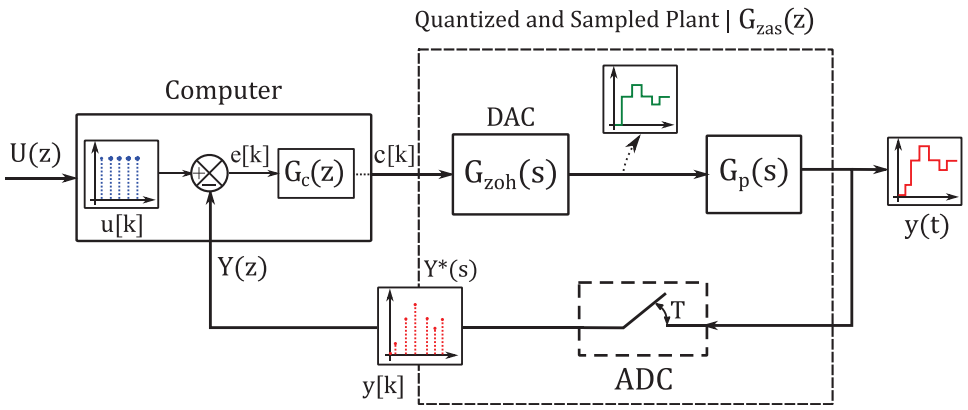

Figure 2-15: Typical discrete control system (elements inside the dashed box are continuous)

Once a suitable analog controller $G_c(s)$ is designed, it may be mapped to the discrete domain by mapping the left-half s-plane inside the unit circle of the z-plane via the bilinear transform

$$s = \frac{2}{T}\left(\frac{z-1}{z+1}\right) \tag{2.15}$$

which preserves the stability of a continuous designed controller, as well as its dynamic performance (provided $\omega_{system} \ll \pi/T$).

The discrete feedback-control loop is then adjusted to compensate for changes in performance which are incurred in the shift from analog to discrete implementations.

The inverse z-transform of the discrete controller transfer function $G_c(z)$ is ultimately evaluated to obtain a computable difference function equivalent for the controller

$$c[k] = \mathcal{Z}^{-1}\{G_c(z)\} \tag{2.16}$$

2.3.3 Proportional-Integral-Derivative Control Approach

The most common feedback-control approach is to employ some combination of Proportional (P), Integral (I), and Derivative (D) control action to correctively modify the process input signal $c(t)$. A conventional PID control system is illustrated in Figure 2-16. The term 'plant' refers to an actuated process.

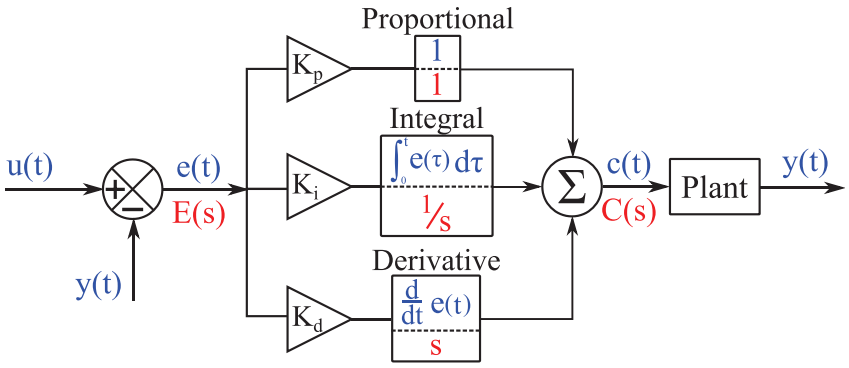

Figure 2-16: Conventional PID feedback control system block diagram

Proportional action allows for the modification of transient dynamics to improve initial system response. *Integral action* improves steady-state error performance by including effects of historical error and raising the system type by at least one. Used alone, it is typically slow in its initial response. *Derivative action* improves dynamic performance by mitigating the rate of change of the error signal. Derivative action is often not employed as signal noise is exacerbated by differentiation. This introduces complications that may not be necessary to

achieve a desired response. The transfer function for a conventional PID controller in given by the following

$$G_c(s) = \left(K_p + \frac{K_i}{s} + K_d s\right) E(s) \tag{2.17}$$

Manual parameter tuning methods based on experimentally evaluated plant dynamics are commonly used for design process simplification (for example the Ziegler-Nichols tuning rules). However, this can be difficult to achieve in practise for systems whose dynamic response is difficult to systematically measure or predict.

2.4 Summary

The literature that was reviewed and discussed in this chapter describes the historical and contemporary state of the art for biaxial mechanical experimentation, characterisation and modelling of human skin tissue. The focus thereof was broadened to include general elastomeric materials which experience large deformations. According to the literature, biaxial testing is required to accurately characterise an elastomeric material under complex loading conditions.

Literature which utilized biaxial testing methods to obtain the mechanical properties and response of skin were few and far between. Uniaxial testing was more commonplace, but suffered from uncertainties due to collagen fibre orientation, and unrealistic boundary conditions for the clamped specimens compared to biaxial testing. Numerous studies were encountered which utilised planar biaxial tests on skin. The studies frequently cited issues regarding difficulties in clamping samples without creating localised stresses by sutured boundaries or poor sample geometry design. They also suffered from uncertainty surrounding (or difficulty in obtaining) the natural collagen fibre orientation. Planar biaxial tests were also found to require cyclic preloading (called preconditioning) to remove hysteresis from the samples prior to experimental testing.

The bulge testing method which is the focus of this report was found to be underutilized in the literature for biaxially testing skin. The bulge testing method was found to be an effective testing method for large elastic deformations for elastomeric materials such as silicone rubber.

The sample geometries for bulge testing were simple and ostensibly required far less design and analysis compared to cruciform specimens for planar biaxial testing. For studies which did use bulge testing to test skin reported that prior knowledge of collagen fibre orientation was not necessary as it could be determined in post processing of experimental data. It was also reported in one study that the preconditioning of skin samples had little effect on repeatability of bulge. The reduced complexity and time saving impact from using the bulge testing technique was evident from the literature.

Since there has been little study in this regard for bulge testing on skin, the apparatuses which were used and described in the literature were basic and *ad hoc* in nature. The solutions were typically bound to singular pressurisation rates (i.e. to a single deformation rate scheme) and were typically application-specific and not reusable across different material and load configurations. In reflection of the literature, a lack of a standardized experimental testing equipment within an institution could make it difficult to compare data across experiments.

Biological skin tissue was shown in multiple studies to be strain rate sensitive. This precedented the review of some basic feedback-control background and theory that would subsequently be used to develop a more sophisticated bulge testing apparatus which could facilitate rate controllability.

Chapter 3

Mechanical System Design

This chapter presents the conceptual development and mechanical design of the prototype bulge testing device apparatus that was undertaken for this project. Most of the bulge testing devices encountered in the literature were *ad hoc* solutions which were purpose built to suit a specific testing configuration. The intended material testing application for this project was human skin tissue which governed the foundation for the design requirements of the apparatus. However, the platform design included adaptability to a larger range of hyperelastic materials under biaxial tension.

Presented first is a simplified phenomenological skin tissue membrane model which was developed to more accurately estimate provisional device design requirements, such as inflation pressure, volumetric displacement and specimen clamp radius. Subsequently the piston actuated pneumatic-hydraulic cylinder concept development and design is presented for the apparatus.

3.1 Skin Membrane Bulge Modelling

The literature review showed that skin mechanical properties can vary significantly. A basic parametric study was performed to investigate some of the mechanical and testing configuration property variabilities (including sample diameter, sample stiffness, and mechanical response shape) to loosely predict design requirements. An isotropic, piecewise linear elastic model was developed to represent skin tissue based on mechanical response behaviour and properties presented in the literature. The maximum bulge pressure and volumetric supply requirements to rupture skin samples were primarily investigated and presented in the section.

3.1.1 Bulge Membrane Theory

A general axisymmetric bulged membrane is illustrated in Figure 3-1. If bending stresses are negligible, the equilibrium of membrane stresses and pressure is given by ([52], [53])

$$\frac{\sigma_\theta}{\rho_\theta} + \frac{\sigma_\phi}{\rho_\phi} = \frac{p}{t} \tag{3.1}$$

where σ_θ and σ_ϕ are the circumferential and meridional stresses respectively, and ρ_θ and ρ_ϕ are local curvatures at the stress element as depicted in Figure 3-1 (instantaneous thickness is denoted t).

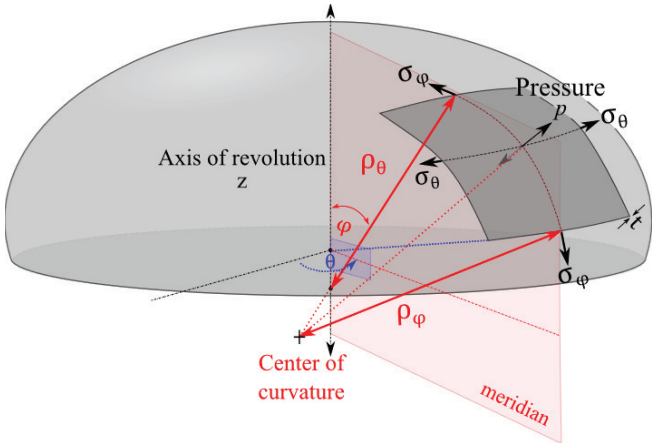

Figure 3-1: Loaded axisymmetric membrane. Adapted from information described in [53]

Spherical isotropic inflation was assumed for model simplification. In this case the curvature is $\rho_\theta = \rho_\phi = \rho$ at any point, and the stresses are equal in either (principal) direction θ, ϕ

$$\begin{bmatrix}\sigma_\theta \\ \sigma_\phi\end{bmatrix} = \frac{p}{2t}\begin{bmatrix}\rho \\ \rho\end{bmatrix} \tag{3.2}$$

3.1.2 Spherical Bulge Modelling

The cross-section geometry for a spherically bulged isotropic membrane is illustrated in Figure 3-2. A spherical inflation assumption, ignoring any local effects at the clamp boundary, was adopted to simplify the modelling for design purposes.

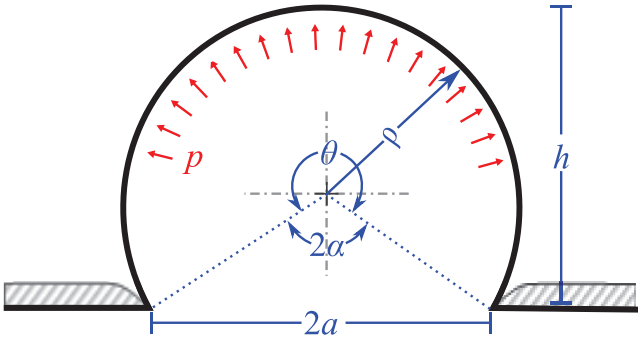

Figure 3-2: Cross-section geometry of a spherically bulged isotropic membrane

The instantaneous radius of curvature ρ can be derived geomtrically in terms of the clamped specimen radius a and vertical apex deflection h

$$\rho = \frac{a^2 + h^2}{2h} \tag{3.3}$$

Similarly, the deformed bulge angle θ can be derived geomtrically in terms of a and ρ

$$\theta = 2(\pi - \alpha) = \begin{cases} 2\,\mathrm{asin}(a/\rho)\,, & h \le a \\ 2\pi - 2\,\mathrm{asin}(a/\rho)\,, & h > a \end{cases} \tag{3.4}$$

Stretch is a measure of deformation defined as the ratio of the deformed and undeformed lengths l and l_0 respectively, where $l_0 = 2a$

$$\lambda = \frac{l}{l_o} = 1 + \varepsilon \tag{3.5}$$

and ε is nominal strain. Circumferential stretch is therefore given for the geometry shown in Figure 3-2 by

$$\lambda_c = \frac{\rho\theta}{2a} \tag{3.6}$$

Skin is commonly considered to be incompressible. Hence the through-thickness stretch may be given in terms of the circumferential stretch as follows

$$\lambda_t = \frac{1}{\lambda_\theta \lambda_\phi} = \frac{1}{\lambda_c^2} \tag{3.7}$$

Giving instantaneous membrane thickness in terms of original thickness t_0,

$$t = t_o\lambda_t = \frac{t_o}{\lambda_c^2} \tag{3.8}$$

Subtituting (3.3) and (3.8) into either component of (3.2) gives the circumferential spherical membrane stress equation

$$\begin{aligned}\sigma_c &= \frac{p\rho}{2t_0}\lambda_c^2 \\ &= \frac{p(h^2 + a^2)}{4ht_o}\lambda_c^2\end{aligned} \tag{3.9}$$

3.1.3 Piecewise Linear Elastic Pressure Model for Skin Tissue

Skin tissue exhibits a nonlinear anisotropic mechanical response due to its fibrous constituency. The consequent mechanical response has a characteristic 'J-shaped' curve as is illustrated in Figure 3-3. The response is characterised by a highly compliant initial linear response with stiffness E_1, followed by a much stiffer linear elastic region with stiffness E_2. A transitional toe region (referred to at a single inflection point) occurs between the two linear regions.

For pressure modelling, equibiaxial skin bulging was presumed to be isotropic, spherical, and with a piecewise bilinear mechanical response as has been described. Variation of the stiffness inflection point was investigated. The inflection point was located at an arbitrary stress $k_\sigma\sigma_{uts}$ where k_σ is a ratio of the tensile strength σ_{uts}. Referring to Figure 3-1 in a plane-stress configuration, a conventional near elastic relationship, neglecting shear strains, is given [54]

$$\begin{bmatrix}\varepsilon_\theta \\ \varepsilon_\phi \\ \varepsilon_t\end{bmatrix} = \frac{1}{E}\begin{bmatrix}1 & -\upsilon & -\upsilon \\ -\upsilon & 1 & -\upsilon \\ -\upsilon & -\upsilon & 1\end{bmatrix}\begin{bmatrix}\sigma_\theta \\ \sigma_\phi \\ 0\end{bmatrix} \tag{3.10}$$

where the Poisson's ratio υ was set with a value of 0.47. Young's modulus is denoted E.

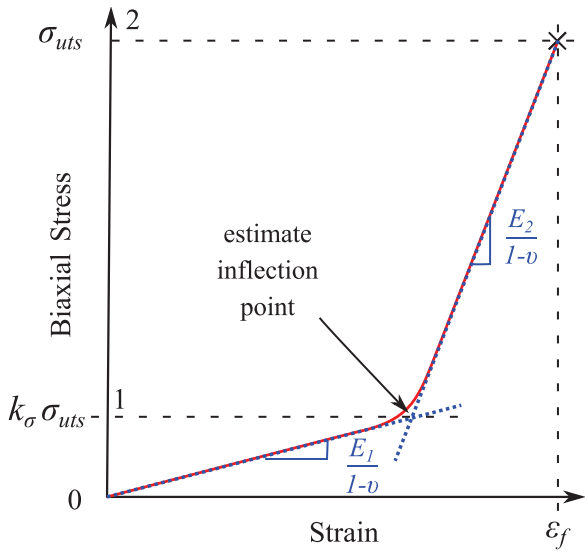

Figure 3-3: Description of piecewise linear elastic model used to estimate the mechanical response of skin tissue (in equibiaxial loading)

Referring to the plane-stress linear elastic relation given by (3.10), the stress at an arbitrary n^{th} piecewise state is given by the cumulative sum of the individual deformation contributions

$$\begin{aligned}\begin{bmatrix}\sigma_\theta \\ \sigma_\phi\end{bmatrix} &= \frac{1}{1-\upsilon}\sum_{i=1}^{n} E_i \begin{bmatrix}1 & 0 \\ 0 & 1\end{bmatrix}\begin{bmatrix}\varepsilon_\theta \\ \varepsilon_\phi\end{bmatrix} \\ &= \frac{1}{1-\upsilon}\sum_{i=1}^{n} E_i \begin{bmatrix}1 & 0 \\ 0 & 1\end{bmatrix}\begin{bmatrix}\varepsilon \\ \varepsilon\end{bmatrix}\end{aligned} \tag{3.11}$$

where $E_i/(1-\upsilon)$ is the biaxial modulus for each consecutive linear region.

Referring to the circumferential spherical bulge membrane stress given by (3.9), the plane stress at the arbitrary n^{th} state may also be given by the following relation

$$\begin{bmatrix}\sigma_\theta \\ \sigma_\phi\end{bmatrix}_n = \frac{p_n \rho_n}{2t_0}\begin{bmatrix}\lambda_c^2 \\ \lambda_c^2\end{bmatrix}_n \tag{3.12}$$

Equating either linear elastic stress component in (3.11) with either membrane stress component in (3.12) gives the following linear elastic membrane relation

$$\begin{aligned}\frac{1}{1-\upsilon}\sum_{i=0}^{n} E_i \varepsilon_i &= \frac{p_n \rho_n \lambda_{c_n}^2}{2t_0} \\ &= \frac{p_n \rho_n (1+\sum_{i=0}^{n}\varepsilon_i)^2}{2t_0}\end{aligned} \tag{3.13}$$

where ε_i are the respective piecewise circumferential strain contributions for each stiffness E_i.

Rearranging (3.13) to solve for pressure in terms of deformation gives the objective linear elastic piecewise pressure model for a spherically inflated membrane

$$p_n = \frac{2t_0}{1-\upsilon}\,\frac{\sum_{i=0}^{n} E_i \varepsilon_i}{\rho_n (1+\sum_{i=0}^{n} \varepsilon_i)^2} \tag{3.14}$$

where ρ_n and ε_i are both geometric terms which depend on the vertical apex displacement h_n and the fixed undeformed specimen radius a (see (3.3) to (3.6)).

The bulged membrane was modelled as a spherical cap whose volume can be shown to be given by the following geometric relation

$$V_{sb_n} = \pi h_n^2 (\rho_n - h_n/3) \tag{3.15}$$

3.1.4 Provisional Requirements Modelling

A basic parametric study was performed based on the preceding models to provide provisional system requirement estimates. Model parameters were based on the initial specifications given in Table 3-1, which were based on the uniaxial mechanical data which were reported in the literature (refer to Table 2-1 in Chapter 2). The corresponding results were presumed for a range of behaviours anticipated for skin.

3.1.4.1 Methodology

Circular specimens with variable sample diameter $2a$ were considered. The initial stiffness E_1 was set at a fixed value and the final stiffness E_2 was set as a free parameter as more quantitative data was reported in the literature for the final stiffness than for the initial stiffness. The inflection stress ratio parameter k_σ was varied as little substantive data was found in the literature regarding the inflection region. The range for k_σ given in Table 3-1 was chosen arbitrarily as a starting point that would subsequently be constrained to maintain the specifications in Table 3-1.

Final stiffness was increased incrementally between $E_2 = \{10, 25, 50, 75, 100\}$ MPa. For each stiffness the sample radius was increased in 5mm increments in its prescribed range. For each

sample size increment the inflection ratio parameter k_σ was evaluated at 0.5% increments within its prescribed range.

The linear elastic strain contributions ε_1 and ε_2 were evaluated individually per (3.10). The stress components were set as piecewise stress contributions $\sigma_{0\to1} = k_\sigma \sigma_{uts}$ and $\sigma_{1\to2} = \sigma_{uts}(1 - k_\sigma)$ with respective uniaxial stiffnesses E_1 and E_2 (see Figure 3-3). At the respective stretches λ_{c_1} and λ_{c_2} the corresponding curvatures ρ_1 and ρ_2 were numerically evaluated according to (3.6). Hence the described strains and curvatures were used to model pressure according to the linear elastic bulge pressure model given by (3.14). The corresponding deflections h_1 and h_2 were evaluated numerically according to (3.3) in order to estimate the geometric bulge volume according to (3.15).

Table 3-1: Initial pressure modelling properties and specifications

Initial Model Specifications				
Parameter	Description	Type	Value	Unit
σ_{uts}	Failure stress in either principal direction	maximum	30	MPa
E_1	Initial young's modulus	maximum	1	MPa
E_2	Final young's modulus	free	10 - 100	MPa
ε_f	Biaxial failure strain (in either direction)	range	0 - 1	$^{mm}/_{mm}$
k_σ	% of σ_{uts} at which inflection occurs	free	0 - 10	$\%_{uts}$
a	Undeformed circular specimen radius	free, provisional	10 - 50	mm
t_0	Undeformed specimen thickness	provisional	1	mm
p_t	Bulge pressure per original thickness	maximum	10	$^{bar}/_{mm}$

3.1.4.2 Results

Failure strains which were evaluated at σ_{uts} are shown in Figure 3-4 for the range of k_σ which fell within the prescribed 100% strain range. When $k_\sigma = 0$ the response is entirely linear elastic with stiffness E_2. The results show that the predicted failure strain increases linearly with increasing inflection stress and decreases with increasing final stiffness. Skin will probably fail before 100% strain, but other hyperelastic materials can exceed this. Failure strains for $E_2 = 10\ MPa$ were higher than 100% and were omitted for falling out of prescribed bounds.

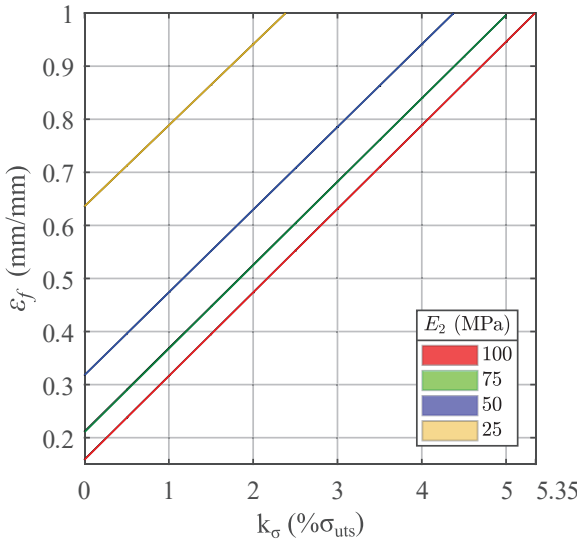

Figure 3-4: Predicted failure strain vs. inflection stress ratio percentage

The reported thickness of skin samples varied widely across the literature with numerous situational and physiological factors. Bulge pressure p_t was considered per millimeter thickness since the thickness is unknown *a priori* and the pressure model given by (3.14) is proportional with thickness.

The modelled pressures which were presumably sufficient to rupture skin are shown in Figure 3-5. The results show that the maximum pressure is mostly influenced by sample size, where decreasing sample size increases the rupture pressure substantially. Reducing low complaince strain and increasing E_2 appreciably increased the bulge pressure required. The range of modelled rupture pressures varies between about 250 – 1000 kPa (per mm undeformed thickness).

Figure 3-6 shows the modelled pressure-strain response for a 1mm thick ∅50mm specimen. The intermediate inflection behaviours shown are more likely representative of skin since the prescribed 100% biaxial strain limit which determined the upper values of k_σ was conservative. The results indicated it is likely that a combination of large deformations at low pressures and small deformations at high pressures can be expected for skin tissue deformation.

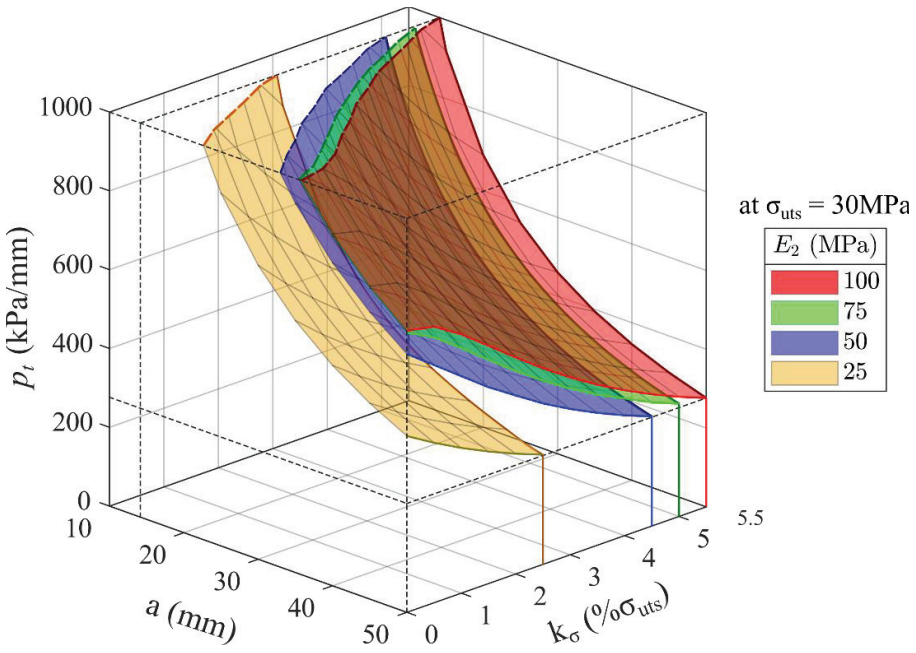

Figure 3-5: Modelled rupture pressure for an arbitrary spherical specimen

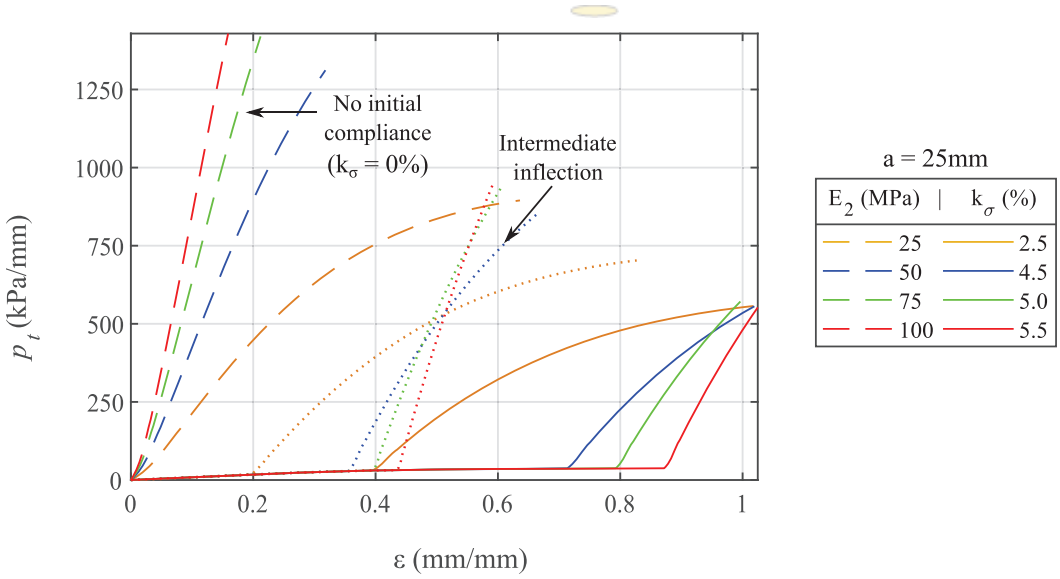

Figure 3-6: Pressure vs. strain model behaviour for a ∅50mm circular specimen

The estimated spherical bulge volumes at rupture were modelled according to (3.15) and are shown in Figure 3-7. The results suggest that the volume is influenced predominantly by the extent of the initial compliance, and the clamped sample diameter. The volume required also

increases appreciably with lower final stiffness. The results suggested that the geometric bulge membrane volume may be expected to fall anywhere within a range of $10 - 500\ m\ell$.

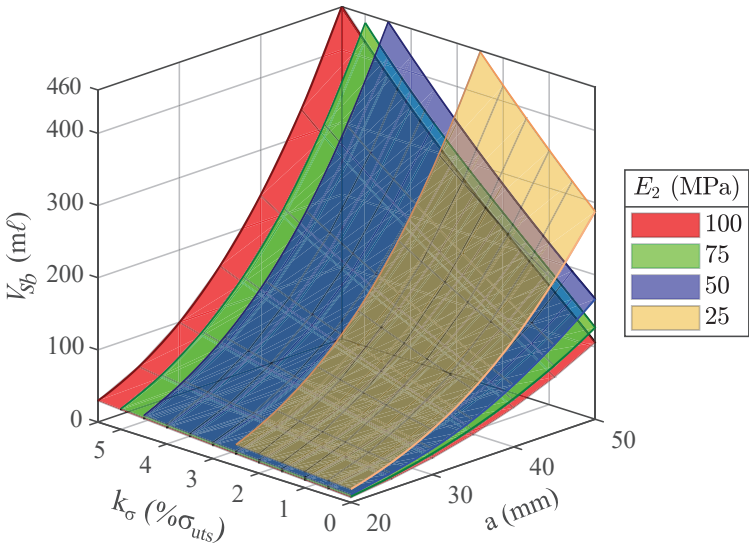

Figure 3-7: Predicted rupture volume of spherical bulge at a 30Mpa bulge stress

3.2 Bulge Testing Apparatus Design

A 10bar pneumatic pressure supply which is typical in a laboratory environment was readily available for the project. It was evident from the earlier modelling that control over a wider range of pressures was required, necessitating some leveraging of the supply pressure range.

Pressure intensification is illustrated in Figure 3-8. Balance of the forces acting on either piston head results in the pressure being multiplied by the ratio of the cross-sectional areas

$$p_2 = \frac{A_1}{A_2} p_1 \tag{3.16}$$

This solution has two primary advantages:

1. the cylinder geometry is easily configurable into either a pressure intensification or reduction arrangement.
2. the pressurising and pressurised fluid media are separable

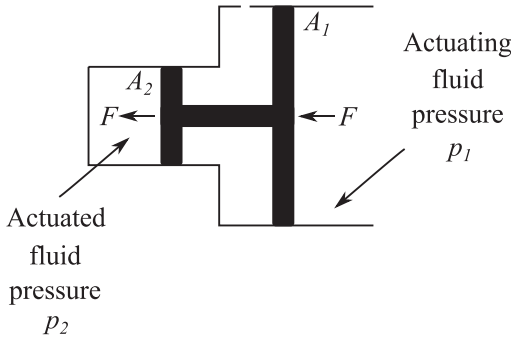

Figure 3-8: Pressure intensification schematic

The separation of pressure media allowed for hydraulic pressurisation in the closed volume chamber (p_2) which had two notable advantages. Hydration of biological tissues during testing was frequently encountered in the literature to simulate *in situ* conditions *in vitro*. Also, gas pressurisation results in rapid gas expansion after a sample ruptures which may lead to unintended secondary post rupture damage effects on the material samples.

The arrangement shown in Figure 3-8 can also be configured in a pressure intensification configuration by making the pressurised cylinder's cross-section smaller than the pressurising cylinder. In a reducing configuration the pressurising cylinder's cross-section is kept smaller than the pressurised cylinder. A pressure reducing configuration has the benefit of reducing pressure step resolution if a discrete electronic pressure actuator is used to control pressurisation. A modular diameter configuration was therefore considered for customisable pressure modification in orderto best suit particular pressurisation needs of an application.

The prototype piston-cylinder apparatus model is shown in Figure 3-9 in a pressure reducing configuration. The design was intended to be modular so that the configuration may easily be adapted to accommodate higher or lower pressure configuration by adjusting the diameters of the upper and lower cylinders. Detailed mechanical drawings for the fabriacted mechanical assemblies, subassemblies, and indivdual components are presented in Appendix A.

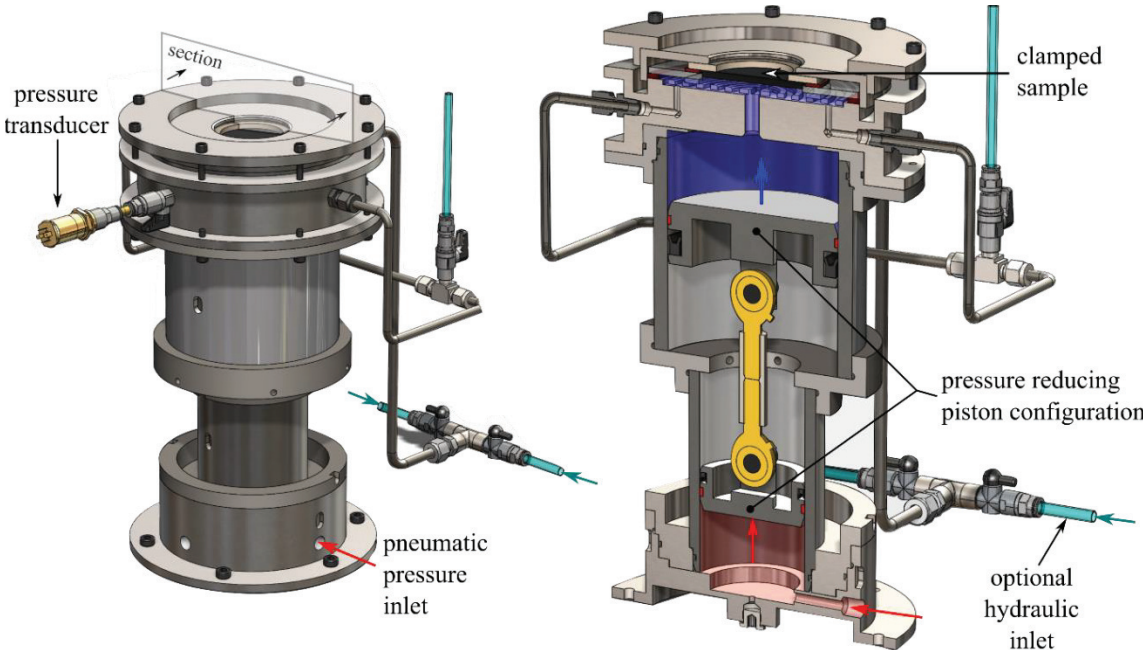

Figure 3-9: CAD rendering of the bulge testing piston-cylinder device prototype

3.2.1 Sample Clamping and Pressurisation

The current method that was employed for clamping samples with variable size configurations is illustrated in Figure 3-10. The clamp manifold plate provides a fixed interface between the actuated cylinder's pressure medium and the clamped sample, as well as provides accessory ports that could be used for pressure measurement and hydraulic supply.

The top face of the manifold plate was designed with concentric channels which were initially intended to provide support against sagging for thin membranes, with the sample providing sealing at the clamping interface and a similar thickness silicone rubber gasket to seal at the adapter perimeter. However, sample deformation occurred when applying clamping force directly to the specimen without any additional pressure load as shown in Figure 3-11.

The clamping method shown in Figure 3-10 was an *ad hoc* solution to expediate platform development. A material sample is affixed to a laser cut Masonite™ wood board backing ring with a chosen aperture geometry. The sample is bonded to the ring using an appropriate bonding agent (this may cause chemical interactions which may not be permissible when testing with skin tissue). In this configuration clamping force is applied to the board instead

of the sample, thereby avoiding premature deformation. The clamping cap was designed to transfer clamping force from the clamping bolts to the adapter without requiring a unique clamping cap design for an arbitrary sample diameter. The adapters were intended to be simple to design and fabricate, to accommodate varying sample diameters as required.

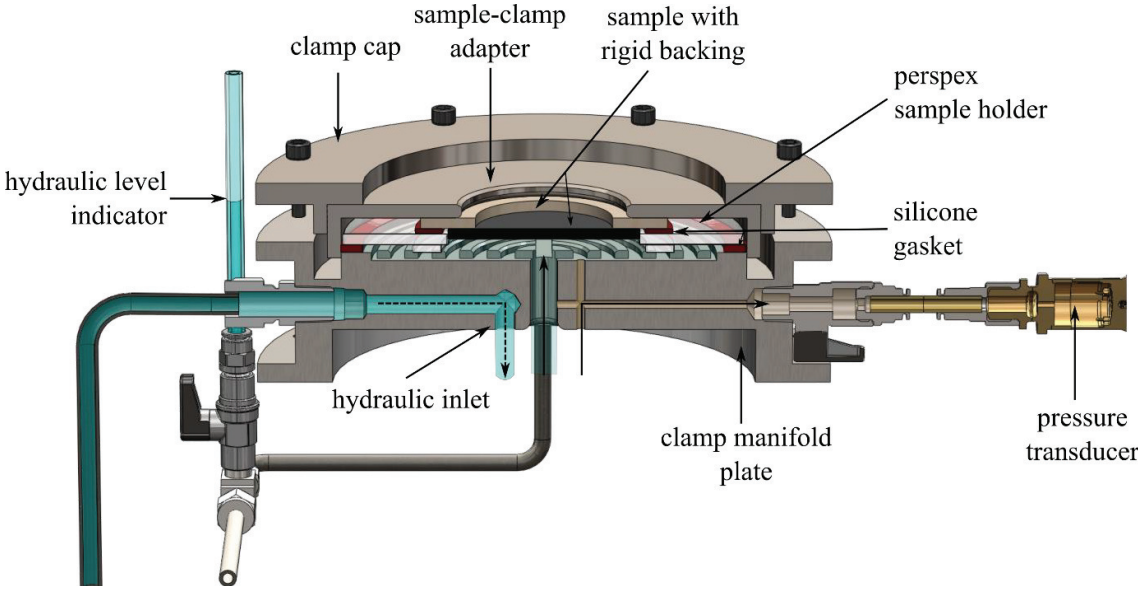

Figure 3-10: CAD rendering of the prototype sample clamping and pressure interface

Figure 3-11: Photo of unpressurised sample deformation caused by material boundary clamping (generic neoprene rubber sheet specimen)

Stainless steel tubing was connected to the manifold plate to support a hydraulic filling interface. The hydraulic inlet was made from ∅8mm tubing which was intended to be gravity fed manually from an external hydraulic source. Smaller ∅6mm tubing was used to provide an accessory port which was used to gauge the hydraulic level. In addition to the filling inlet, a clear Perspex tube is connected to the chamber, to act as a level indicator during initial filling and venting operations. The level indicator is isolated from the main chamber prior to starting pressurisation.

3.2.2 Piston-Cylinder Apparatus

The prototype pressure reducing bulge testing piston-cylinder apparatus is shown in Figure 3-12. The low- and high-pressure cylinders have ∅120mm and ∅75mm respectively, resulting in a pressure reduction ratio of 2.56 [as per (3.16)] and a maximum attainable bulge pressure of 3.9bar. All fabricated components were manufactured using mild steel. The cylinder tubes were made from honed mild steel tubing. Corrosion of the mild steel components was not considered critical, as the device is easily drained and dried between use and is stored in a climate-controlled laboratory. Components that contact biological tissue can be manufactured from stainless steel later if required for hygienic reasons.

The pneumatic inlet/outlet interface is at a fixed base plate. The adjacent pneumatic cylinder is connected to the baseplate using an appropriate adapter. The cylinder tubes are connected to each other with an appropriately sized and vented adapter. The upper cylinder is connected to the manifold via a cylinder-specific adapter. All components were designed with threaded connections so that easy modification could be achieved in future work. Slots were machined into each concentric cylinder so that custom C-shaped spanners with a hooked end could be used to manually tighten the threaded components. Where necessary, radial O-ring seals were used to seal components which contained pressurised media.

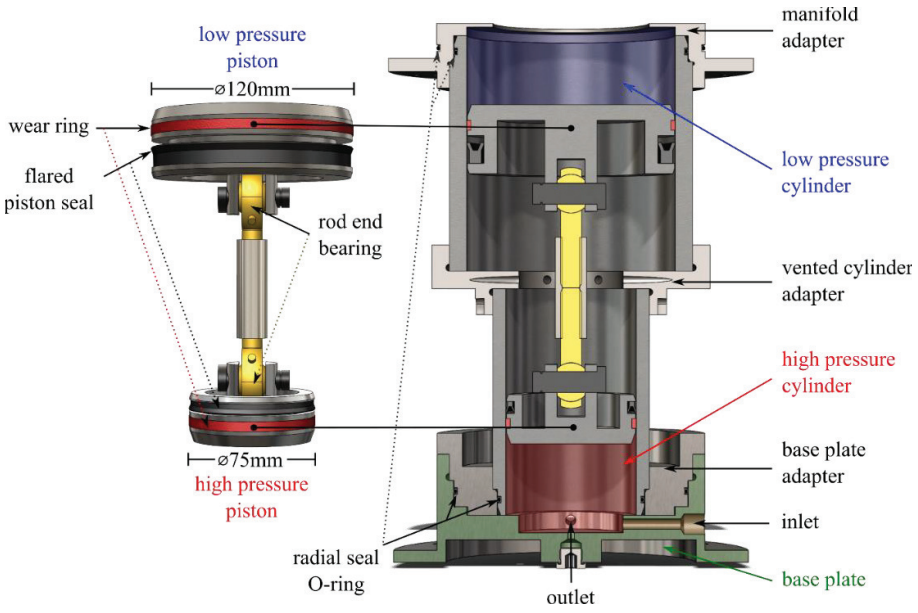

Figure 3-12: CAD rendering of the piston-cylinder configuration

Both piston heads were connected to orbital rod end bearings for self-alignment of the heads if the cylinders. Radial PTFE-material wear rings on the piston heads were used to avoid metal on metal contact between the piston and the cylinders. Flared rubber U-seals with a maximum pressure rating of 40bar were used to seal between the pistons and the cylinders.

A total piston stroke of about 90mm was practically achieved for this prototype piston-cylinder configuration. In the enclosed ∅120mm cylinder there is an available initial fluid storage volume of 1ℓ. Referring to the preceding modelled bulge volumes presented Figure 3-7, this volume of fluid would be adequate provided an incompressible medium was used in the pressurised cylinder for a ∅50mm specimen. However, if pneumatic pressursation is required, compression of the gas will substantially reduce the full scale volume capacity of the cylinder.

3.2.3 Selection of the Pressurisation Actuator

An off-the-shelf component solution was required to automatically control inflation pressure in the cylinder. A digital proportional servo valve for pressure control was primarily considered [55]. The operation of the pressure regulation valve as shown in Figure 3-13 produces a setpoint output pressure signal by adjusting an analog servo piloted control valve using a PID control system, the combination which allows for precision control of the output pressure. This solution was optimal for the application as it could produce a linearly proportional output pressure signal for a tracked setpoint pressure function. Unfortunately, the solution was not within the budget of this research project.

As an alternative, a proportional solenoid piloted pressure regulator was investigated. The theory of operation is similar to the servo valve regulator shown in Figure 3-13, but uses balancing solenoid valves to regulate the pressure (see Appendix C). This solution is cost-effective but has an associated minimum pressure output, and an output resolution as a result of the balancing of the solenoid valves.

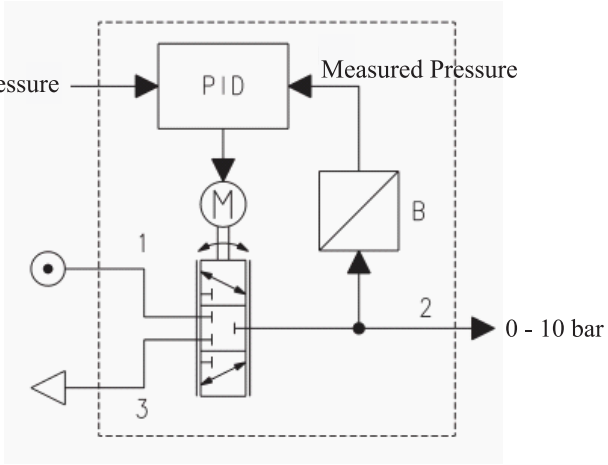

Figure 3-13: Operation of a digital proportional servo valve for pressure control (adapted from [55])

A Camozzi MX-PRO series solenoid piloted pressure regulator was sourced within budget. The device has a reported minimum realisable output of 0.bar (50 kPa) and a reported output resolution of 5kPa [56]. The resolution was expected to degrade the low-range performance of the pressurisation control system as fine control and compensation would be difficult to achieve for the discrete pressure steps. However, for proof of concept of the platform for further development, this regulator was chosen as a compromise. The expectations for low-range performance were thus limited by constraints set by the resolution.

3.2.4 Pneumatic Circuitry

Integration of automatable pneumatic pressurisation control functionality and manual control intervention for the piston-cylinder apparatus was paramount for an effective bulge testing platform. The pneumatic circuitry that was designed for semi-automatability of pneumatic control of the piston-cylinder apparatus is shown in Figure 3-14 (the corresponding components are given in Table 3-2). Four paths are indicated:

- Supply (red) - constant regulated 10bar pneumatic pressure supply to the primary pneumatic control components

- Control (green) - automatically controlled and varied pressure output signal. Pressure is set by a closed loop feedback controlled electronic control signal which is input to an electronic pressure regulator (EPR)
- Return (blue) - returns the piston to the bottom of the cylinder. An inline venturi vacuum generator (#13 in Figure 3-14) was used to generate a negative pressure in the lower cylinder to overcome piston friction
- Exhaust (yellow) - purges the pneumatic pressure in the lower cylinder

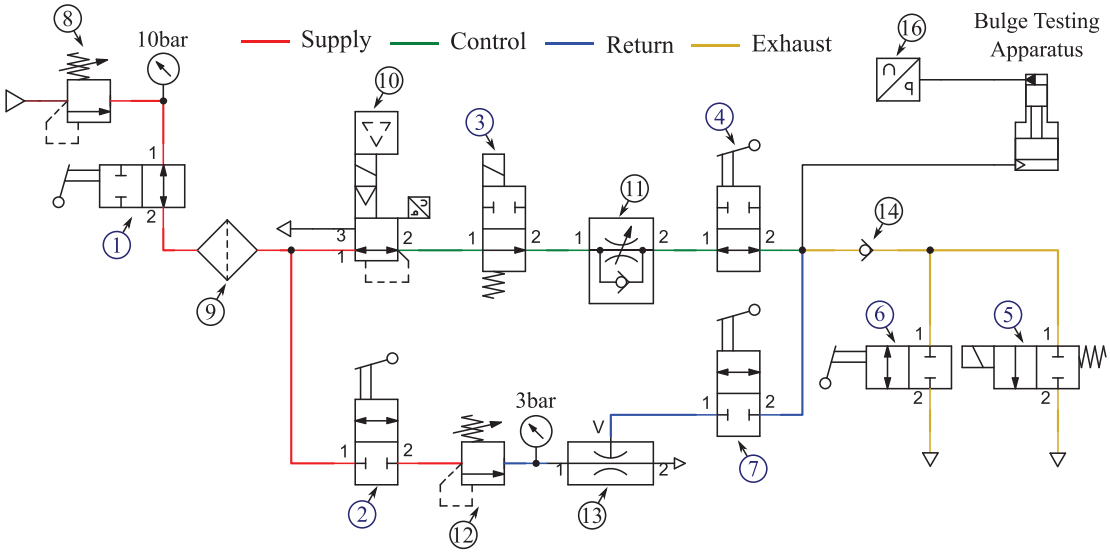

Figure 3-14: Pneumatic circuit diagram

Table 3-2: Pneumatic circuitry components

No.	Component	Description
1, 2, 4, 6, 7	Isolating valve	Manual ball toggle
3, 5	Isolating valve	Automatic solenoid toggle: Supply: *SMC VDW250* [57] Exhaust: *SMC VX210* [58]
8	Pressure regulator	10bar supply regulator
9	Pneumatic filter	-
10	Camozzi MX-PRO series EP Regulator	Input: 0.5 – 10V DC Output: 0.5 – 10bar
11	Flow control valve	Adjustable needle valve
12	Pressure regulator	Manual 3 bar regulator
13	Vacuum generator	Venturi vacuum generator: *Piab piINLINE® MICRO* [59]
14	Non-return valve	-
15	Accessory port	Discretionary use
16	Gems 31IS series 4-20mA pressure transducer	0 – 10bar

The physical configuration of the pneumatic circuitry corresponding to Figure 3-14 is shown in Figure 3-15. A laser-cut folded sheet metal base box was manufactured to house the listed components. The pneumatic component thread sizes were standardised where possible to G1/4-inch British standard pipe threads. Flexible polyurethane tubing with an outer diameter of 6mm and a maximum pressure rating of 12bar was run between interconnecting components.

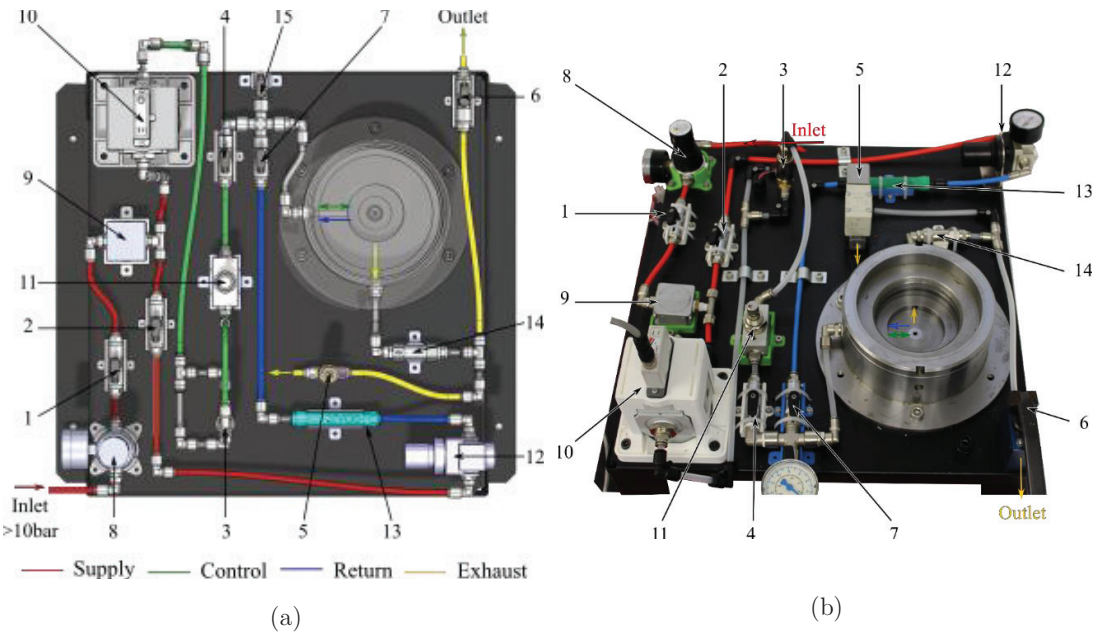

Figure 3-15: Pneumatic circuit configuration (a) CAD rendering (b) Photo of the constructed prototype

A flow restricting needle valve was installed in the control path to reduce flow rate into the cylinder to smoothing abrupt changes experienced in pressure due to the pressure regulator actuator's output resolution. Multiple isolating valves, including two automatically controlled solenoid valves and five manually controlled ball valves (# 1 to 7 in Figure 3-14), were used to manage the mode of the pneumatic supply.

provides a valve logic table which describes the valve positions depending on the mode of supply required. *Idle* mode implies the apparatus is not currently being used for testing. *Active* mode implies that a bulge test is in progress. *Purge* mode implies rapid exhausting of all pneumatic pressure in the system. *Return* mode implies return of the piston to resting position by generating a small vacuum in the lower cylinder.

Table 3-3: Pneumatic supply mode valve logic table
'O' = Open, 'C' = Closed, '-' = Neutral

Mode	**Supply**		**Control**		**Exhaust**		**Return**
Valve No.:	1	2	3[a]	4	5[a]	6	7
Idle	C	C	C	C	O	O	C
Active	O	C	O	O	C	C	C
Purge	-	-	-	C	O/C	C/O[b]	C
Return	O	O	C	C	O	O	O

[a] Automatic solenoid toggle

[b] Only if manual override is necessary

Figure 3-16: Photo of the constructed and assembled mechanical bulge testing apparatus

3.3 Summary

A basic parametric study was performed to analyse the pressure requirements for rupturing a range of skin samples, whose mechanical response was modelled as piecewise bi-linear. Sample diameter and final stiffness were found to most impact the pressure requirements. Rough pressure requirement estimates were identified (per mm sample thickness) between 250 kPa/mm at sample ⌀30mm and 1000 kPa/mm at sample ⌀100mm. A mechanical piston-cylinder apparatus was designed which is capable of proportionally reducing or intensifying the supply pressure in a concentric separately sealed cylinder of different piston-cylinder diameter connected to a supply piston-cylinder. The configuration described in this chapter achieved a pressure reduction ratio of 2.56. Pneumatic circuitry was designed to control pressurisation in the system. Automation adjustment and control of the pressure regulation

was based on an electronic proportional pressure regulator which was installed in the pneumatic supply path to supply pressure between 0.5 - 10 bar. Pressure measurement was performed with a single 0 – 10 bar pressure transducer.

Chapter 4

Feedback Control System Design

Skin tissue has been previously described in the literature as a rate dependent material which may affect its mechanical properties. Implementation of a controllable mechanical rate parameter was therefore required for the bulge testing device. This chapter describes the detailed design of a closed loop feedback control system used to implement a fixed operating pressure-loading rate for the bulge testing apparatus. A digital proportional-integral (PI) closed-loop negative feedback controller was ultimately designed to be implemented as part of an embedded control system which is described in the proceeding chapter. In this chapter an appropriate analog controller design is first described. This is followed by description of an equivalent digital controller implementation which maps the original analog domain controller to the discrete domain.

Relevant control theory and background is presented in the literature review, (§2.3). In this report, the term 'dynamics' is used to describe the time response of a system in general. System dynamics refers to the time response characteristics of a system which may be described by a (linear) differential equation of n^{th} order. Transient dynamics refers to the time response characteristics of a system during a change from an initial equilibrium state to a final settled state.

4.1 Pressurisation Rate Control Concept

Skin was shown in the literature to exhibit rate dependent mechanical characteristics. As this design was intended to provide a general use mechanical testing platform for skin tissue, a predominant design feature that was to be incorporated was facility for some form of

parametric rate controllability. In the case of conventional uniaxial tensile testing, constant strain rate is typically controlled via controlled specimen grip separation rate.

Skin exhibits large anisotropic deformations, implying strain is inhomogeneous for biaxial configurations. Large strains are typically digitally imaged during testing and measured subsequently in post-processing using digital imaging techniques. For conventional uniaxial tests, axial strain rate is typically set by fixing the grip separation rate. For biaxial (bulge) testing, independent multiaxial deformations and a corresponding lack of accessible analog measurement technologies makes strain rate a complicated parameter to model and measure in real-time. Hence strain rate is not as straight-forward parameter to control for the biaxial bulge testing device as it is for uniaxial testing. Rate control was therefore chosen to be implemented via the controlled rate of pressurisation of the bulge testing fluid medium.

Figure 4-1 shows the bulge testing apparatus in a closed loop negative feedback pressurisation rate control application. The driven cylinder pressure is measured using a pressure transducer and compared with the reference pressure input. The corresponding reference error is evalauted and compensated for by a digital feedback control software algorithm which is designed to minimse the error signal. The digital controller output is converted to a electronic control signal which is input to an electronic pressure regulator. Here the electronic control signal is converted to a corresponding actuating mechanical pressure which drives the piston-cylinder apparatus.

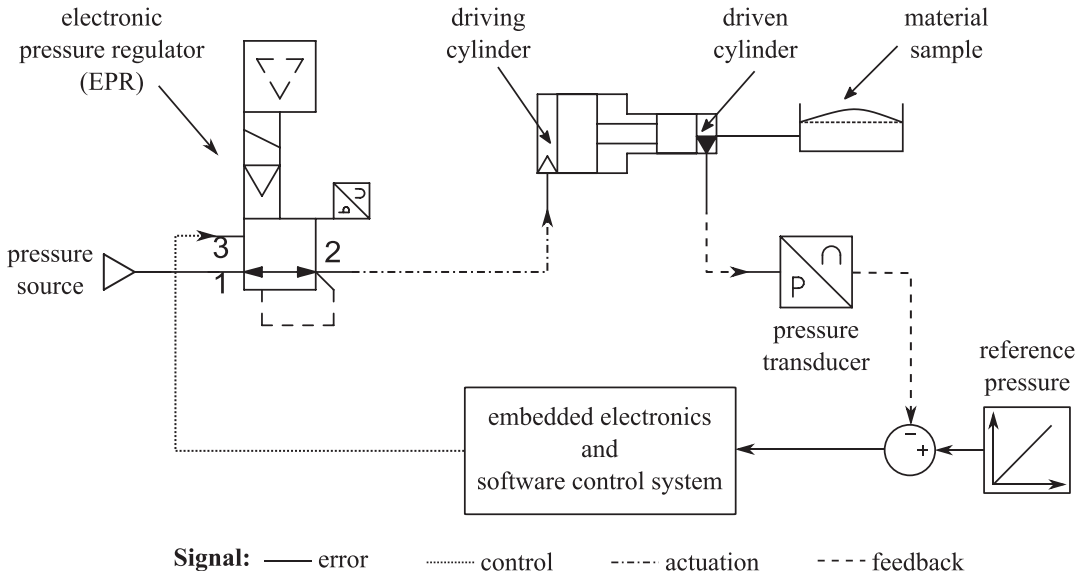

Figure 4-1: Closed loop negative feedback pressurisation rate control concept

4.2 Mechanical System Transfer Function Model

A transfer function model of the bulge testing apparatus' vessel pressurisation dynamics was initially required for the feedback control system design. The mechanical system was modelled as a pneumatic pressure vessel system that is actuated by the electropneumatic pressure regulator. The modelling approach that is presented was adopted from a pneumatic modelling approach described by Ogata [60]. The transfer function model that is presented in summary in this section is developed in detail in Appendix B.

4.2.1 Deformable Pressure Vessel Model

A pressure vessel system with a deformable boundary is illustrated in Figure 4-2. The system is at an equilibrium pressure $\overline{P}$ and is disturbed by an input pressure stimulus p_i, resulting in a dynamic pressure change p_o in the vessel. Mass flows across flow resistance R between the pressure source and vessel which has total fluid capacitance C.

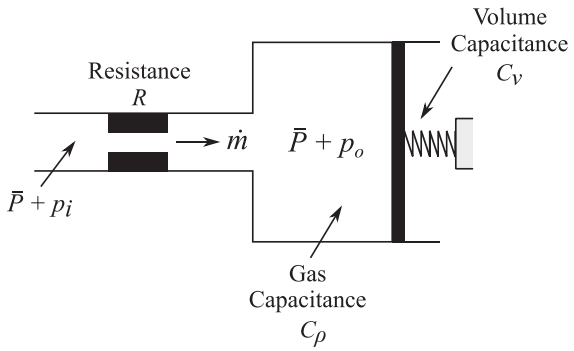

Figure 4-2: Schematic of a pneumatic pressure vessel with a deformable boundary. Adapted from information produced in [60]

Flow resistance R is the gradient of change in pressure differential with a change in mass flow, which for small changes in pressure may be given by the following

$$R = \frac{p_i - p_o}{\dot{m}} \tag{4.1}$$

Fluid capacitance C of a volume is the gradient of mass stored with the corresponding change in pressure in the volume, which for an incremental mass $(\dot{m} \times dt)$ may be given by the following

$$\begin{aligned} C &= \frac{dm}{dp} \\ \Rightarrow \dot{m} &= C\frac{dp_0}{dt} \end{aligned} \tag{4.2}$$

The compressible gas and deformable vessel volume shown in Figure 4-2 each have respective capacity for mass storage, whose individual effect on total capacitance is additive. Flow resistance and total capacitance values are nonlinear and variable but may be considered constant about an operating point. The system may be described by the first order transfer function

$$\begin{aligned} \frac{P_o(s)}{P_i(s)} &= \frac{1}{sR\left(C_v + C_\rho\right) + 1} \\ &= \frac{1}{RCs + 1} \end{aligned} \tag{4.3}$$

4.2.2 Bulge Testing Apparatus Model

The pressure vessel schematic for the bulge testing apparatus is shown in Figure 4-3. The configuration is similar to Figure 4-2 but includes an additional sealed chamber. The transfer function between pressure in the upper chamber and the inlet pressure in the lower chamber includes the piston gain k as follows

$$\frac{P'_o(s)}{P_i(s)} = \frac{k}{(RC')s + k} \tag{4.4}$$

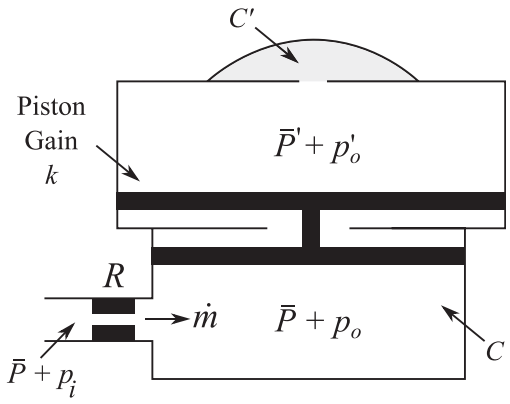

Figure 4-3: Pressure vessel schematic for the bulge testing apparatus

The RC' term is a time constant term which determines the speed at which pressure in the upper cylinder responds to an applied input $P_i(s)$. The value of the time constant is equal to the time taken to reach 63.2% of the final pressure in response to a input step

$$\tau_p = RC' \tag{4.5}$$

The individual flow resistance and capacitance terms given by are unfeasible to predict independently as the value of the terms have multifactorial dependencies. The time constant term is primarily driven by specimen stiffness (which can't be known accurately *a priori*).

4.3 Feedback Controller Design

This section presents a two-stage root-locus based design approach which was performed. Design of an appropriate analog controller for the system described in the preceding section is presented first. This is followed by a discrete mapping of the analog controller to the digital

domain, and a subsequent adjustment of the controller parameters to maintain prescribed control system performance criteria. The proceeding design was predictively based on the preceding dynamic vessel pressurisation transfer function model which was described.

4.3.1 Controller Selection

The primary requirement of the feedback control system was to produce a stable system pressure output signal at a constant specified pressurisation rate. Pressurisation rate is a difficult quantity to measure directly as there aren't any readily available solutions. Time-differentiation of a pressure transducer signal would exacerbate physical signal noise and would be cumbersome to implement. Pressurisation rate was therefore indirectly imposed by setting the control system's reference input as a linear pressure ramp signal with a specified rate.

The system was required to operate with reasonable steady-state error. Proportional-only feedback control of the first-order mechanical system given by (4.4) has no integrating poles (poles at $s = 0 + j0$) and would result in a diverging system output response for a ramped input. Addition of a single integrating pole into the control path increases the system type, thereby constraining the steady-state error to a constant value. A conventional proportional-integral (PI) controller was selected which is described by the transfer function

$$G(s) = K_p \frac{(s + \sigma_a)}{s} \tag{4.6}$$

where K_p and σ_a are both free parameters. The proportional gain K_p primarily influences the response rate of the control system dynamics. The location of the controller zero σ_a (on the negative real axis in the analog domain) primarily influences the transient characteristics of the control system response.

4.3.2 Design Methodology

The methodology presented in this section considers the design of the analog PI-control system in the complex s-domain. The feedback-control system loop that was considered is shown in Figure 4-4. The system was left as simple as possible due to novice design experience.

The pressurisation model for the lower cylinder given by (4.4) was considered as it was independent of the piston gain. The first-order process dynamics were governed by the time-constant parameter τ_p given by (4.5). The pressure regulator actuator was modelled as a unity gain[1] with a time delay of period T_d seconds[2]. The plant is thus described by the transfer function

$$P(s) = \frac{e^{-T_d s}}{\tau_p s + 1} \tag{4.7}$$

with τ_p as a free parameter since both the sample-material boundary and flow control valve setting were variable. The value of the time-constant was therefore unknown *a priori* but could be physically measured from a step-input response prior to a test for an arbitrary configuration.

The plant time-constant τ_p was subsequently treated as a known parameter that was parametrically varied across a nominally estimated plant response design range

$$0.2s \leq \tau_p \leq 1.2s \tag{4.8}$$

The sensor was nominally modelled as first order described by the transfer function

$$H(s) = \frac{1}{\tau_m s + 1} \tag{4.9}$$

where τ_m is the sensor's physical measurement time-constant parameter[3].

The system shown in Figure 4-4 is thus described by third order closed-loop transfer function

$$\frac{Y(s)}{U(s)} = \frac{G(s)P(s)}{1 + G(s)P(s)H(s)} \tag{4.10}$$

A root-locus based design and analysis approach was utilised as it was familiar method for closed-loop feedback control design that allowed for simple, graphical variation of free design

[1] Actuator resolution was not modelled. Consequences of this omission are discussed in (§6.3.3)

[2] T_d was measured and was conservatively estimated at approximately 100ms (refer to Appendix B)

[3] τ_m was measured and was estimated at approximately 20ms (refer to Appendix B). Sensor dynamics were not expected to significantly affect the design dynamics but were nominally considered

parameters. Root locus design methodology by pole-zero placement is discussed in Appendix B. The PI-controller design strategy that follows was adopted from Fadali *et. al.* [61].

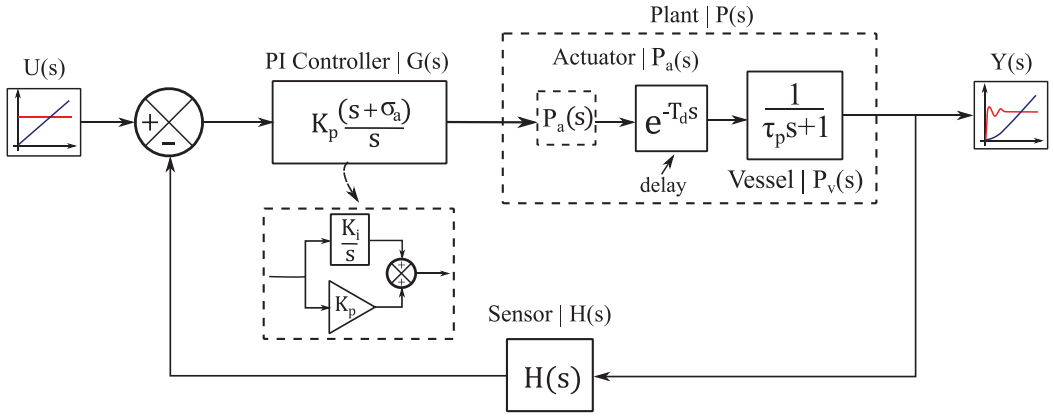

Figure 4-4: Analog proportional-integral control system feedback loop

A proportional controller $G(s) = K_p$ was first designed to achieve satisfactory transient performance for the system given by (4.10). In this case the only free parameter available was the proportional gain K_p. The dominant poles were thus identified from the root-locus plot for a particular time-constant to satisfy a nominally imposed damping ratio performance range

$$0.7 \leq \xi \leq 0.9 \tag{4.11}$$

Subsequent integral compensation by integrating pole-zero addition was included to improve the steady-state performance. The integrating-pole and zero for the PI-controller described by (4.6) were placed in close proximity to minimise their combined effect on the transient dynamics of the proportional design. Therefore, a small angle contribution of $\phi \approx 5°$ was added to the dominant poles from the proportional design by locating the controller zero at

$$\sigma_a = \frac{\hat{\omega}_n}{\hat{\xi} + \frac{\sqrt{1-\hat{\xi}^2}}{tan\,(\phi)}} \tag{4.12}$$

where $\hat{\omega}_n$ and $\hat{\xi}$ are the original natural frequency and damping ratio parameters which describe estimated second order dynamics of the closed-loop system.

The root-locus design procedure was repeated for the PI-compensated system(s) to compensate for changes in system dynamics from the original proportional design. Since the PI-controller zero was fixed, the system was compensated by adjusting the gain K_p in order to maintain the damping performance specification given by (4.11).

4.3.3 Continuous System Design Results

The root-locus design methodology described in (§4.3.2) was repeated for plant time-constant increments in the design range given by (4.8). A requirement of the root-locus method is that the loop gain term $L(s) = G(s)P(s)H(s)$ in (4.10) must be rational. The irrational plant delay term in $P(s)$ in (4.7) was substituted by a second-order Padé approximant [62], which is a rational Taylor series approximation

$$e^{-T_d s} \approx \frac{12 - 6T_d s + (T_d s)^2}{12 + 6T_d s + (T_d s)^2} \tag{4.13}$$

PI-compensated root-locus plots are shown in Figure 4-5 for a sample of the systems. The shape of the plots was face-value estimates due to the rationalisation of the plant-delay term, and uncertainties in the model and model parameters. The close proximity of the PI-compensated pole-zero pairs is evident. To complete the design, the dominant closed-loop poles for were graphically identified by manually locating the intersection of the root-locus plots with the constant damping ratio loci specified at the limtis of (4.11) which lay nearest to the $j\omega$ axis using Scilab *evans* root locus function.

Bode magnitude-frequency responses are shown in Figure 4-6 for the respective sample set of PI-control systems with varying plant time-constants. Nearly cancelling pole-zero contributions and negligible sensor dynamics produced an approximate 20dB/decade drop-off rate. The third-order closed-loop system given by (4.10) could therefore be approximated as first-order.

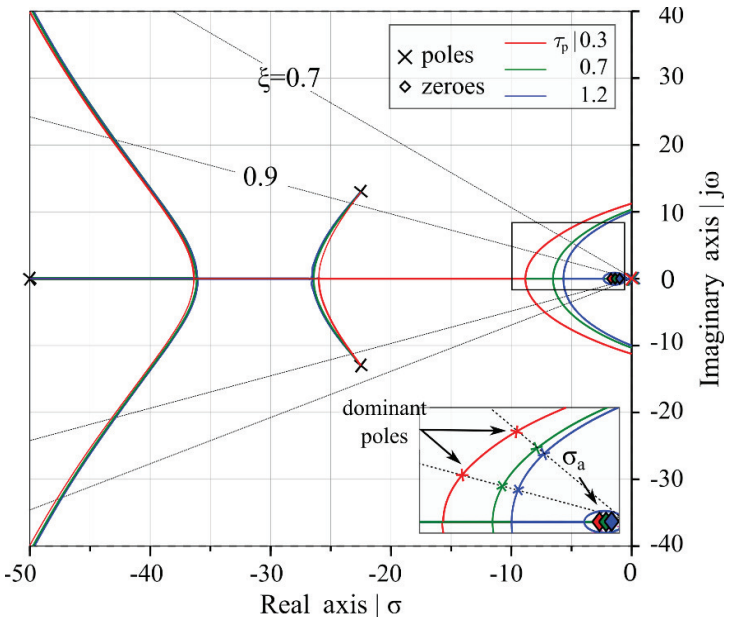

Figure 4-5: Root locus plots of the continuous PI-compensated system(s) with various plant time-constants

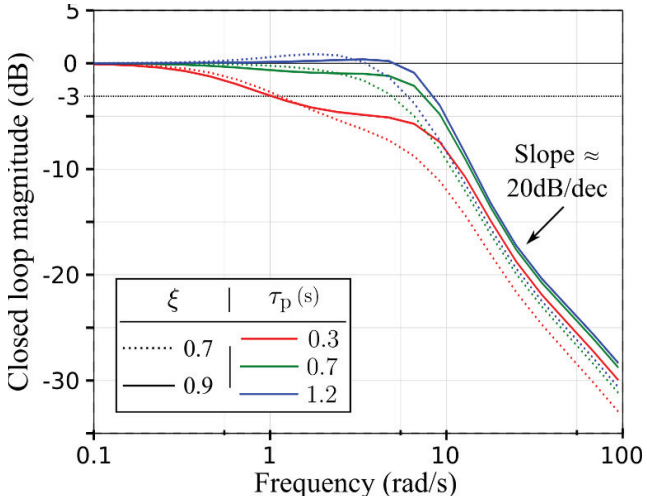

Figure 4-6: Continuous PI-control system closed-loop frequency response

4.3.4 Discrete System Design

The performance of the analog PI-control system design described in the preceding section was satisfactory for the varying plant dynamics in the design range specified by (4.8). The PI-compensated control system design was thereafter completed in the discrete domain in order to make the design digitally implementable.

4.3.4.1 Sampling Rate Selection

The Nyquist sampling theorem states that to recover the maximum frequency ω_{max} present in an arbitrary analog signal without introducing aliasing effects [63], sampling frequency must be at least

$$\omega_s \geq 2\omega_{max} \tag{4.14}$$

The maximum frequency that would be present in the physical system was unknown *a priori*. Frequency characteristics of the discrete system were estimated by the continuous PI-control system design as shown in Figure 4-7. Natural frequency was evaluated as the magnitude of the dominant closed-loop poles. The system bandwidth was estimated at the -3dB frequency ω_{bw} (see Figure 4-6) and indicates that a significant attenuation of signals at low relative frequencies occurs for the systems designed with faster plant response dynamics.

Maximum frequency was estimated to be **10x** the closed-loop system bandwidth

$$\omega_{max} \approx 10\omega_{bw} \tag{4.15}$$

where the maximum system bandwidth in Figure 4-7 was observed to be $\omega_{bw} \approx 8\,rad/s$, which implies a maximum predicted frequency of $\omega_{max} \approx 80\,rad/s$. Substituting this into (4.15) gives the nominal minimum sampling rate required to cover the design range

$$\omega_s \geq 160\,rad/s \tag{4.16}$$

or alternatively,

$$f_s \geq 26\,Hz$$

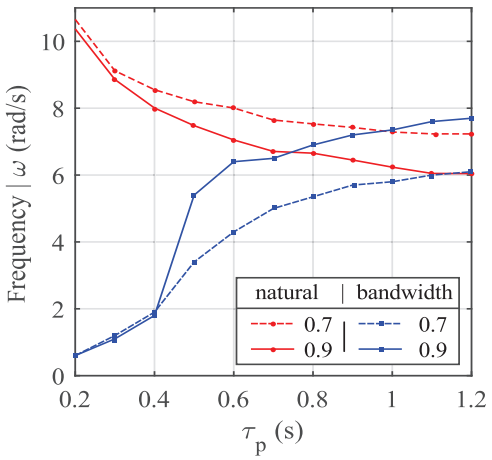

Figure 4-7: Frequency characteristics of the continuous PI-control systems

4.3.4.2 Discrete Control Loop

The analog PI-control loop which was previously illustrated in Figure 4-4 was transferred to the discrete domain as is illustrated in Figure 4-8. Sampling of the analog system output was conventionally modelled with an analog to digital converter (ADC). Physical conversion of the discrete control output signal was modelled using a conventional digital to analog converter (DAC). The combined z-transform of the DAC, the analog plant given by (4.7), and the ADC is given by the zero-order held and sampled transfer function (refer to Appendix B for the worked solution)

$$G_{zas}(z) = \frac{1 - e^{-T/\tau_p}}{z - e^{-T/\tau_p}} \tag{4.17}$$

where T is the sampling period of the ADC[4]

$$T = 2\pi/\omega_s \tag{4.18}$$

Plant delay was treated separately to the plant transfer function. The delay period T_d was assumed an integer multiple of T so that period was given by k_d samples

$$delay(z) = z^{-k_d} = z^{-\lceil T_d/T \rceil} \tag{4.19}$$

Applying the bilinear transform (2.15) to the analog PI-controller transfer function (described by (4.6)) gives the mapped transfer function which describes the response of the PI-controller in the discrete sampled domain

$$G(z) = \left(K_p \frac{\sigma_a + c}{c}\right) \frac{\left(z + \frac{\sigma_a - c}{\sigma_a + c}\right)}{(z - 1)} \quad \Big| \quad c = 2/T \tag{4.20}$$

[4] Hardware limitations prescribed a (conservative) sampling rate of f_s= 60Hz ($\omega_s \approx$ 380 rad /s)

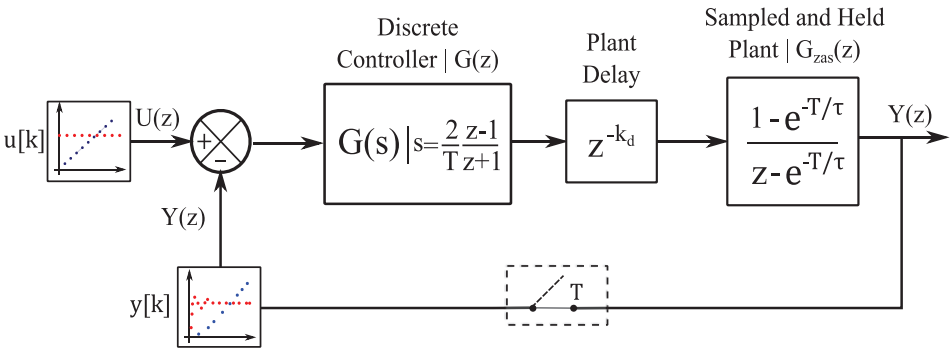

Figure 4-8: Discrete equivalent of the analog PI control system feedback loop

4.3.4.3 Discrete Controller Design Results

The preceding discrete PI-control system that was described in the preceding section is given by the discrete closed-loop transfer function

$$\frac{Y(z)}{U(z)} = \frac{z^{-k_d}\, G(z) G_{zas}(z)}{1 + z^{-k_d}\, G(z) G_{zas}(z)} \tag{4.21}$$

Discrete root locus analysis and design was perfomed for the discrete PI-compensated system described by (4.21) to compensate for deterioration in dynamic performance in the shift from analog to discrete domain. The PI-compensated root-locus plots for the discrete system are shown in Figure 4-5 for various plant time-constant values. The value of σ_a in the discrete controller transfer function given by (4.19) was preserved from the analog PI-controller design. Proportional gain K_p was readjusted to maintain the damping performance specification given by (4.11). The respective critical proportional gains K_p^{crit} were evaluated at the intersecting poles of the root locus plots with the stability boundary (unit-circle $|z|=1$ in the z-plane) to determine the gain margin characteristic for the system.

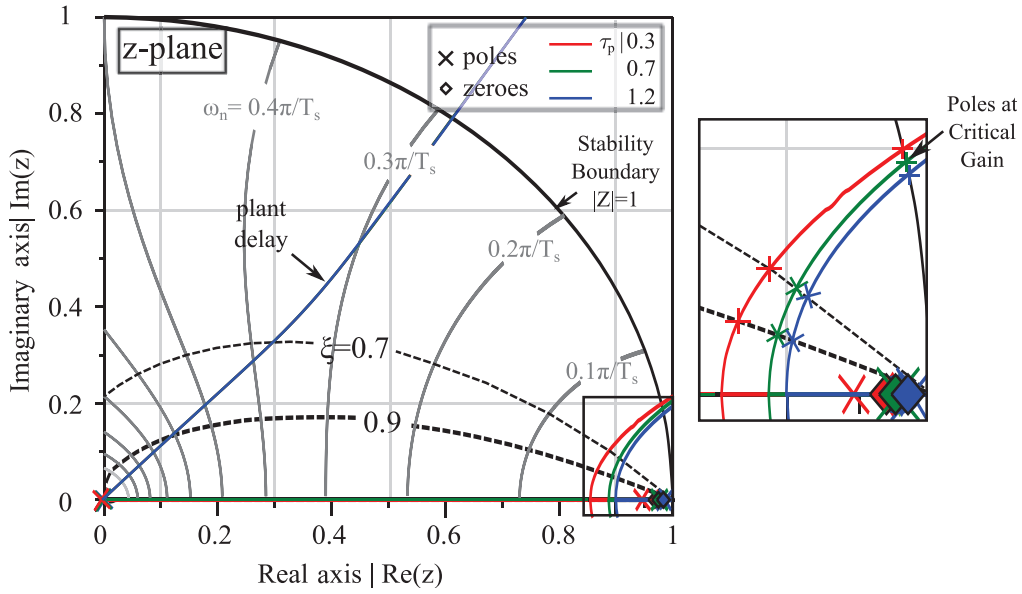

Figure 4-9: Discrete root locus plots of the PI control system for various time-constants

Step and ramp input responses for the discrete control system design are shown in Figure 4-9. The results indicate zero steady-state error for a step input and constant steady-state error for a ramp input as expected. The step and ramp responses results indicate that systems with a smaller time-constant will take longer to reach steady-state than systems with a larger time constant. This was attributed to slower reacting systems permitting the use of more aggressive controller (gain) parameters compared to the faster reacting systems.

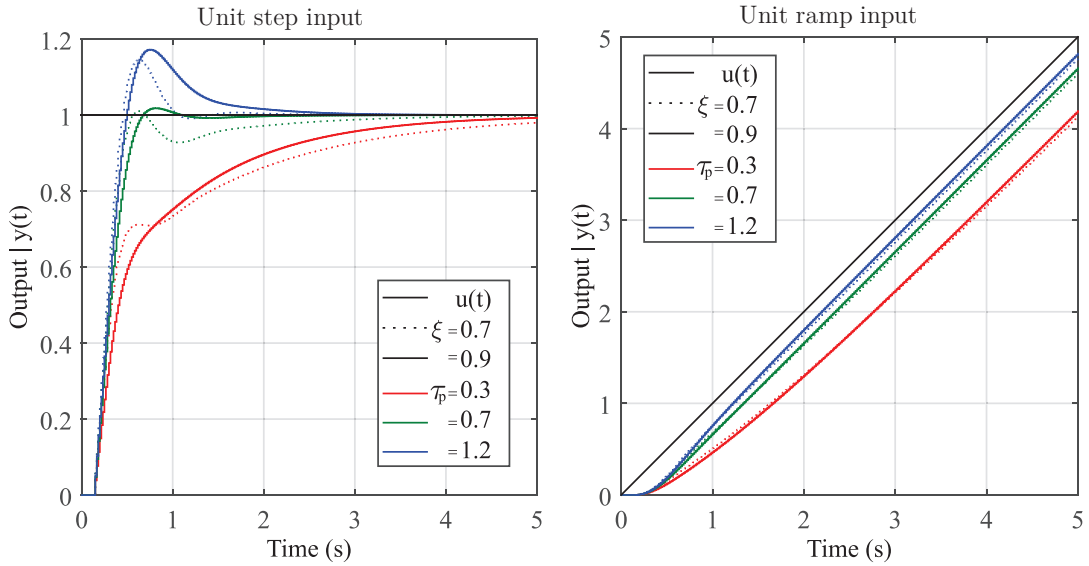

Figure 4-10: Input test responses for the discrete PI-control system(s)

The PI-controller parameters for the transfer function described by (4.20) are shown for the concluded discrete controller design in Figure 4-13. The results are shown for the nominal plant time-constant design range that was considered. Proportional gain is given for the results of the final discrete root locus analysis. Analog zero locus is given by the magnitude of the zero-locus placement on the negative real axis in the s-plane from the preceding analog PI-controller design.

Steady-state error for the discrete system with sampled ramped input is given by

$$e_{ss} = \frac{T}{(z-1)L(z)\,|_{z=1}} \qquad [61] \qquad (4.22)$$

(which ∴ simplifies to) $$= 1/(K_p \sigma_a)$$

where $L(z)$ is the loop gain given for the modelled system by $L(z) = z^{-k_d} G(z) G_{zas}(z)$. The steady-state error given by (4.22) is shown for the concluded discrete control system design in Figure 4-11 as a percentage of the reference signal pressurisation rate.

The provisional gain margin characteristic for the discrete control system is shown in Figure 4-12. Gain margin was evaluated from the gain at the location of the critical poles

$$Gain\ margin_{dB} = 20 \log_{10}\left(\frac{K_p^{crit}}{K_p}\right) \qquad (4.23)$$

The design gain margin was conservative (due to the restrictive damping criteria). This was preferred as there were discrete actuator resolution effects which were as yet not considered.

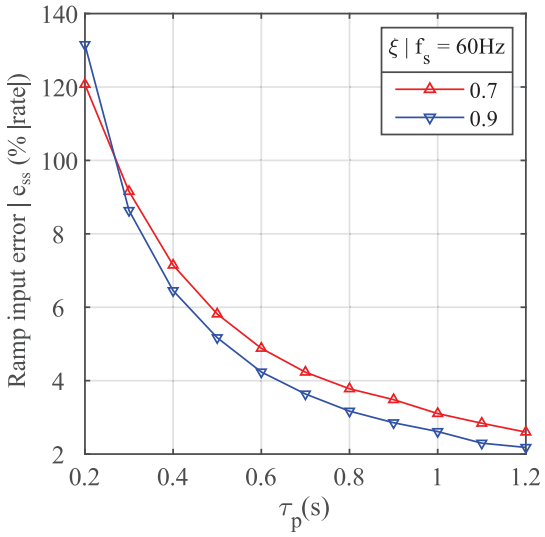

Figure 4-11: Steady-state error design characteristic for a ramp input

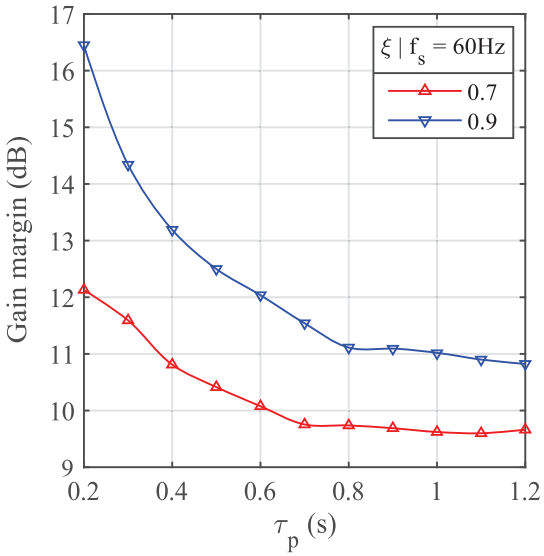

Figure 4-12: Gain margin design characteristic

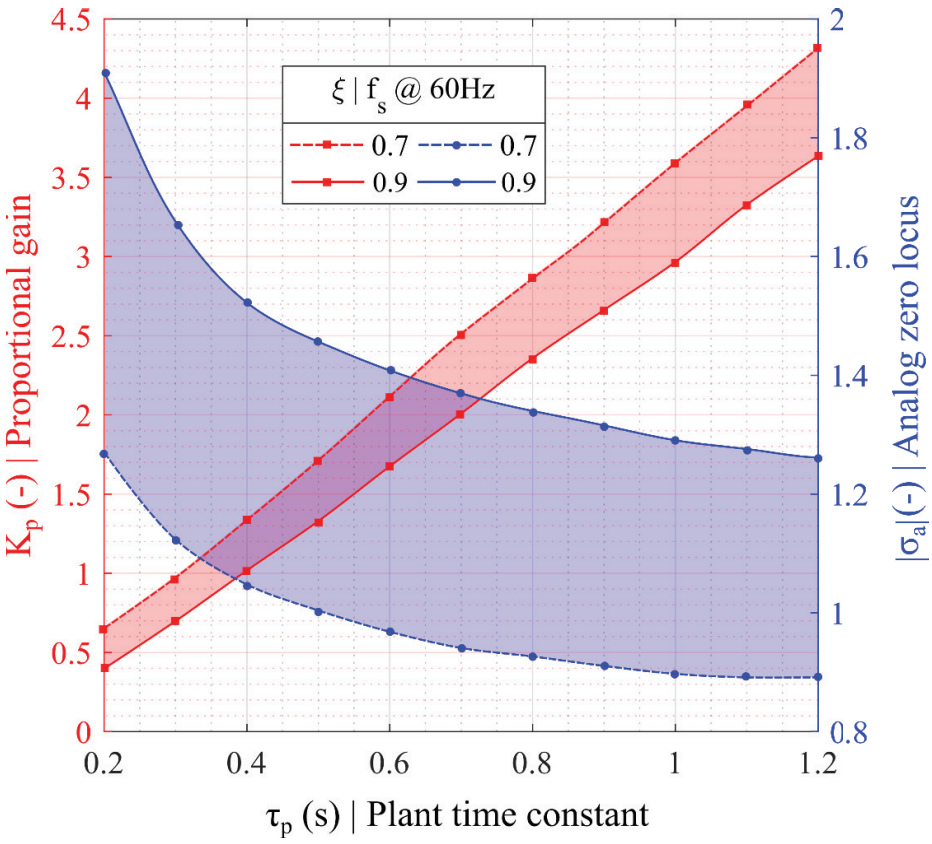

Figure 4-13: Discrete PI-controller design parameter specifications

4.4 Controller Difference Function

In order to practically implement the discrete controller within a software control system, a difference function describing the controller's sampled output state at an arbitrary sample n in the sampled n-domain was required. The control action for the controller with discrete control transfer function $G(z)$ defined by (4.20) is illustrated in Figure 4-14. The controller transfer function can then be given as

$$G(z) = \frac{A(z)}{E(z)} = K_c \frac{z + z_a}{z - 1} \tag{4.24}$$

where $K_c = K_p \frac{\sigma_a + c}{c}$ and $z_a = \frac{\sigma_a - c}{\sigma_a + c}$ are the controller proportional gain and zero respectively.

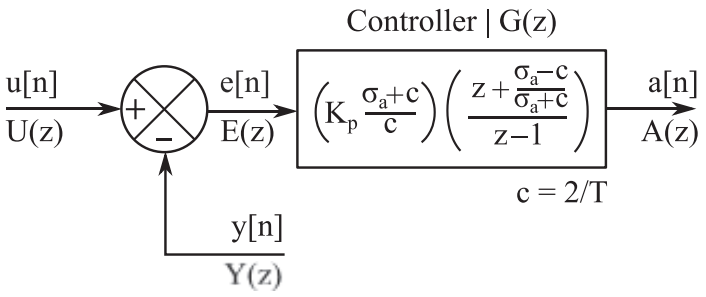

Figure 4-14: Discrete controller transfer function action in sampled n-domain

Multiplying (4.24) by $(z^{-1}/\, z^{-1})$ and rearranging gives the controller output/actuator input $A(z)$ in the z-domain as follows

$$A(z) = \left(K_c \frac{1 + z_a z^{-1}}{1 - z^{-1}}\right) E(z) \tag{4.25}$$

For an arbitrary discrete time signal $x(nT) = x[n]$ the inverse z-transform identity $\mathcal{Z}^{-1}\{x[n-k]\} = (z^{-1})^k\, X(z)$ applies. Rearranging (4.25) into terms containing $(z^{-1})^k$ gives

$$A(z) - z^{-1}A(z) = [K_c\, E(z) + z_a z^{-1} E(z)] \tag{4.26}$$

Taking the inverse z-transform of the individual terms in (4.26) describes the computable difference function for the controller output at an arbitrary sample $\{n \mid n \in \mathbb{Z}, 0 < n < \infty\}$

$$a[n] = K_c\left(e[n] + z_a[n-1]\right) + a[n-1]$$
$$= \left(K_p\frac{\sigma_a + c}{c}\right)\left(e[n] + \left(\frac{\sigma_a - c}{\sigma_a + c}\right)e[n-1]\right) + a[n-1] \tag{4.27}$$

4.5 Summary

The design of the feedback control system that was presented in this chapter is concluded by the expression given for $a[n]$ at an arbitrary sample n given in (4.27). The difference function provides a sampled, computable function for the PI feedback controller output which was easy to implement within the software control system. This would provide a convenient mechanism for on-the-fly custom specification of the controller gain and zero locus parameters to suit a control system design according to the response speed of the plant which is unknown *a priori*.

Chapter 5

Instrumentation and Controls

This chapter describes the architecture, design and development of the electronic hardware and software control systems that were created and integrated with the bulge testing platform. The fully integrated platform illustrated in the schematic in Figure 5-1 is an integrated hardware and software system comprising of three primary subsystems, namely:

a) The mechanical pneumatic piston-cylinder hardware (described in Chapter 3)
b) The electronic hardware circuitry used for sensor integration, signal conditioning, data acquisition, and actuation control
c) The embedded software control system used for test data acquisition (DAQ) management and processing, task automation, implementation of feedback control (described in 0), and user interfacing

The latter two subsystems are presented in detail in this chapter. This aims to provide a functional description for the individual systems to provide full context for the testing platform. Electronic controls and implementation are described first. The selection and implementation of electro-mechanical instrumentation and associated electronic hardware circuitry that was designed for the components are described. The software control system that was designed to interface with the physical bulge testing apparatus is subsequently described. A high-level functional outline of the software architecture and operation is presented.

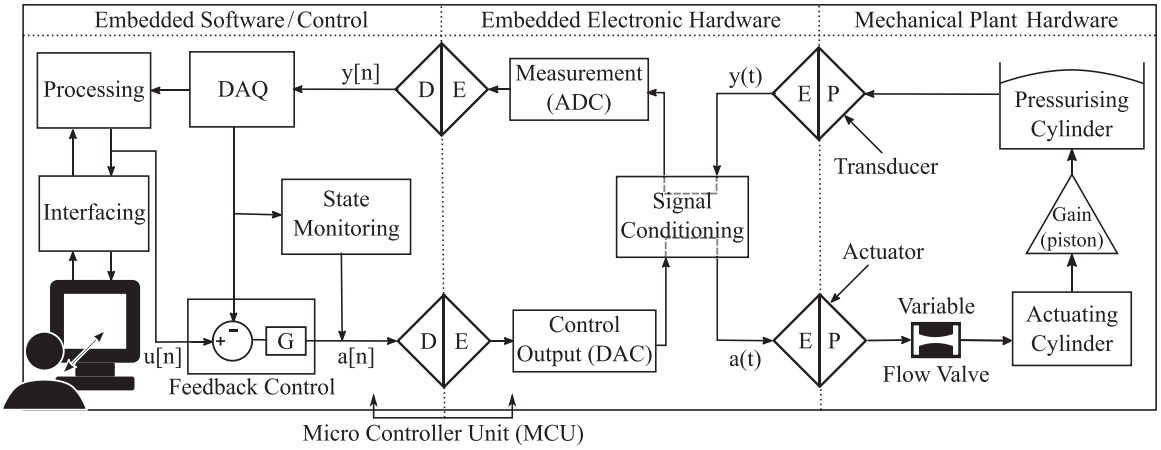

Figure 5-1: Block diagram schematic of the integrated system bulge testing platform

5.1 Electronic Hardware

A high-level block diagram of the embedded electronic hardware control system is shown in Figure 5-2. Two key functions of the electronics system which are prominently detailed in this chapter were to measure and sample the pressure sensor output, and to provide physical actuation control for the piston-cylinder apparatus using an electronic pressure regulator.

The embedded software control interface was developed on an STMicroelectronics STM32F4-Discovery platform evaluation board. The board houses a 32-bit STM32F407VG Micro Controller Unit (MCU) as well as other useful prototyping peripheral hardware. The evaluation board was chosen for its superior speed and memory performance (32-bit at 168MHz; 1024kB ROM and 192kB RAM [64]), compared to other common rapid prototyping MCU solution such as the Arduino Uno (8-bit at 16MHz; 32kB ROM and 2kB RAM [65]) or Arduino Mega 2560 (8-bit at 16MHz; 256kB ROM and 8kB RAM [65]). This provisioned facility for the handling of all control and automation tasks onboard a single MCU.

A dedicated host PC was interfaced with the MCU. The host was responsible for configuring, receiving, decoding, storing, and displaying all test data from the MCU. Serial communications with the MCU were handled using the UART (Universal Asynchronous Receiver Transmitter) protocol. A Prolific PL2303TA USB to UART converter [66] was used to interface the USB-capable host with the UART-capable MCU.

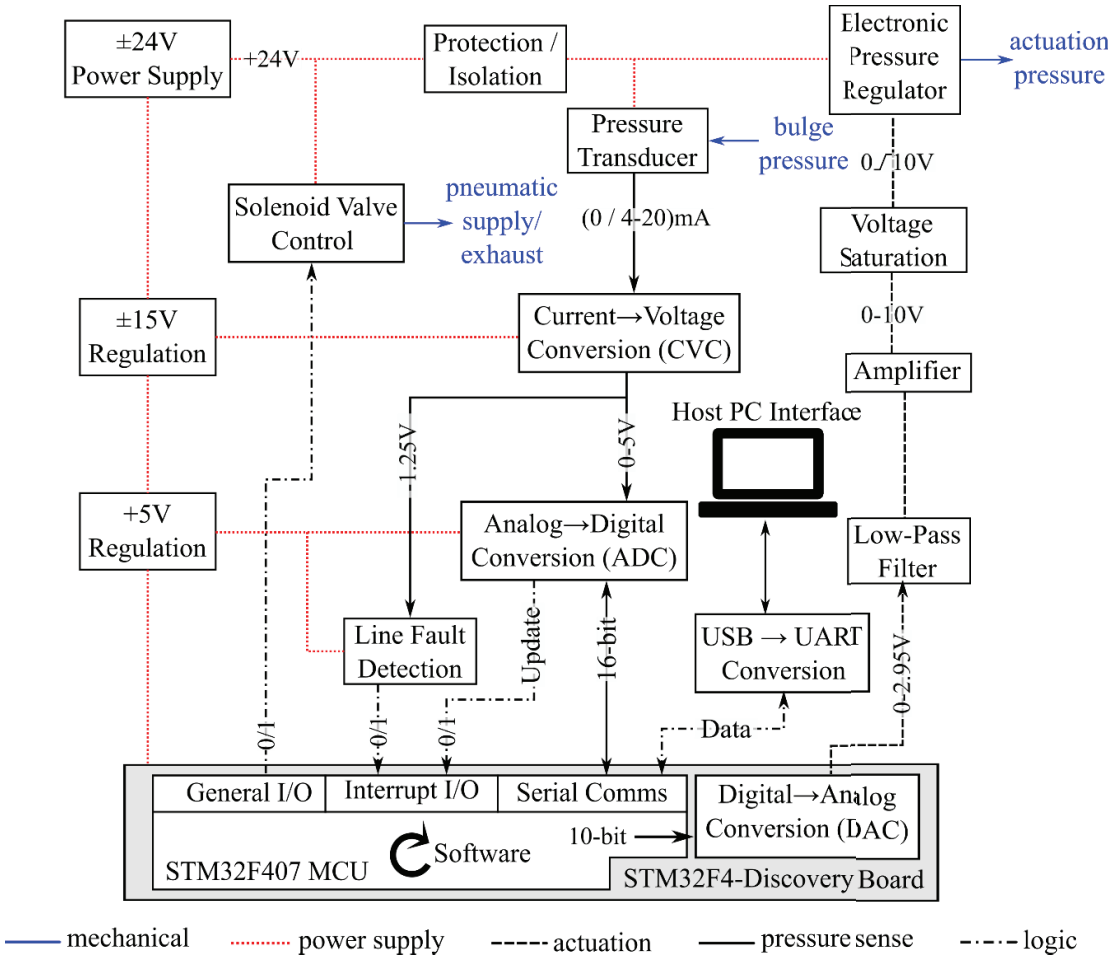

Figure 5-2: Block diagram schematic of the integrated electronic hardware system

5.1.1 Pressure Sensor

Accurate pressure measurement was paramount for recording the bulge pressure and effectively controlling its rate. Accuracy of the measurements is affected by the quality and full-scale capacity of the particular pressure transducer sensor used. As part of the overall platform development, a generic solution was designed for hassle-free interchangability of the transducer between tests to best suit the maximum predicted pressure load. Care was also taken to design robust electronic circuitry which could safeguard the (high cost) devices from user error. A detailed block diagram schematic of the electronic circuitry that was designed to measure pressure level using a 4 - 20mA ouput type transducer is shown in Figure 5-3. Current output transducer sensors were chosen over voltage sensors as the same interface

circuit could easily be used to accomodate any 4 – 20 mA sensor, and allowed for automatable diagnosis of line fault detection (as a 0 mA output would indicate an open circuit fault).

A Texas Instruments RCV420 current loop receiver Integrated Circuit (IC) chip was used to convert the non-sensible 4-20mA sensor output was converted to a sensible 0-5V output which is input to an ADC for sampling. The IC contains a 75Ω precision resistor and additional circuitry to produce a -1.25V output in open circuit. A 0/5V logic switch was placed on the output and connected to general I/O pin on the MCU in order to monitor the vitality of the signal. Description of the voltage supply requirements, load resistor value selection R_L, and other protective supporting electronics for the pressure sensor are presented in Appendix C.

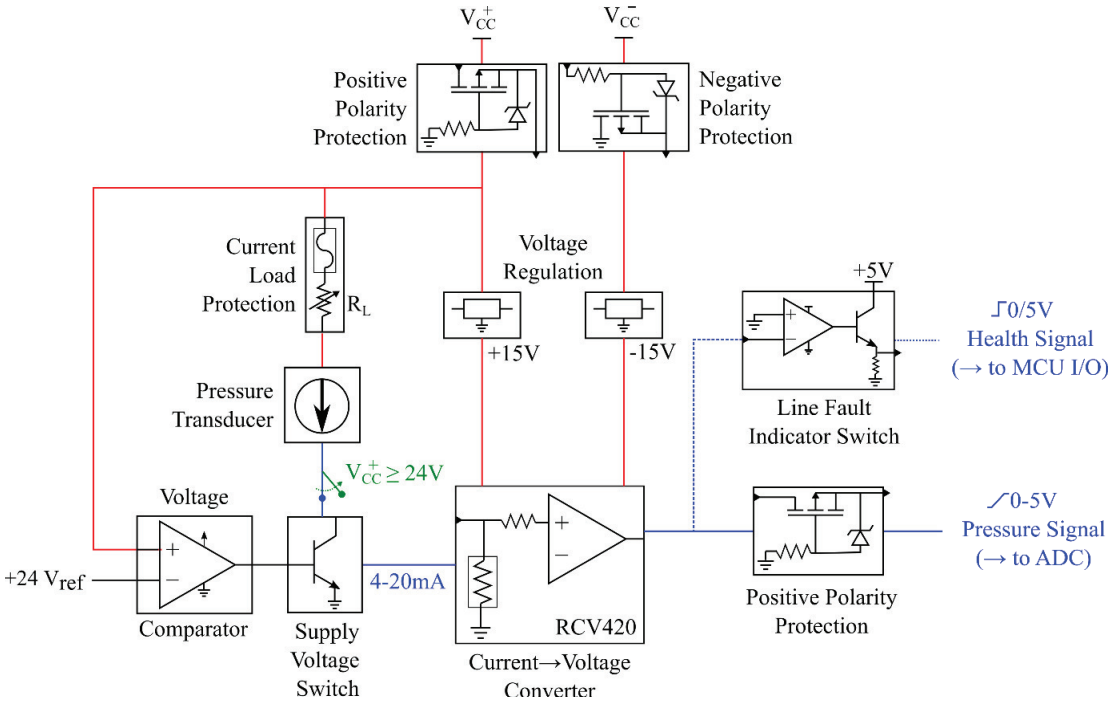

Figure 5-3: Block diagram schematic of the electronic hardware circuitry designed for a generic 4-20mA pressure transducer

5.1.1.1 Transducer Selection

Strict specifications weren't made for the pressure transducer that was used for prototyping in this project as the intention of the platform design was to permit freedom of transducer choice. A Gems Sensors and Controls 31IS series pressure transducer [67] was obtained for this project. The device is rated for a 0 – 10 bar pneumatic or hydraulic pressure input, with

a corresponding 4 - 20mA current output. Relevant information about the device specifications, calibrations, and current state is provided in Appendix C. The transducer's 10bar full-scale range was larger than necessary as the full-scale output of the apparatus in the pressure reducing configuration was 3.9 bar. At full scale the circuit could only produce a 1.95V output out of a possible 5V output, which was suboptimal.

5.1.2 Measurement of Analog Pressure Signal

A 16bit Analog Devices AD7706 Analog to Digital Converter (ADC) [68] was used to measure and convert the ideal 0 – 5V measured output signal to a readable digital value between 0 – 65535 that could be handled by the software control system. This provisioned an acceptable sensible 15Pa pressure resolution for the 10bar pressure sensor that was available for this project.

The AD7706 module was purchased as an Integrated Circuit (IC) chip which required supporting electronic circuitry and software configuration. A printed circuit board (PCB) was adapted from an evaluation board design provided by the manufacturer [69] and fabricated for the project. The electronic circuitry for the PCB is presented in Appendix C.

5.1.3 Electronic Proportional Pressure Regulator Actuator

A solenoid-piloted EPR was used in a closed-loop feedback configuration to automatically regulate the bulge pressure and pressurisation rate for actuation of the piston inside the cylinder. A Camozzi Series MX-PRO EPR [56] was obtained for the project, which is modular combination of a Camozzi Series MX2 pressure regulator which is piloted by a Camozzi Series K8P solenoid -EPR. Relevant information regarding the device's operation, specifications, and calibrations are presented in Appendix C.

The EPR converts a 0 - 10V analog command input voltage signal V_{CMD} to a corresponding 0 – 10bar output pressure signal. The device operates with a stated 5kPa output resolution and 0.5bar minimum realisable output. A maximum of 190 discrete pressurisation steps was therefore practically attainable across the 0.5 - 10bar output pressure range. The device's linear performance was good overall but did exhibit some sporadic failed conversions.

A block diagram schematic for the electronic circuitry that was designed to supply and control the EPR is shown in Figure 5-4. The device was expensive and required input supply polarity and overvoltage protection. Analog voltage output from the DAC was shifted from 0 – 2.95V to 0 – 10V using a non-inverting op amp configuration with an amplification factor of 3.4. A low pass filter was added on the command signal to reject non-DC signals past 50Hz. Further description of the voltage supply requirements, op-amp gain amplification and other electrical protective measurements are also presented in Appendix C.

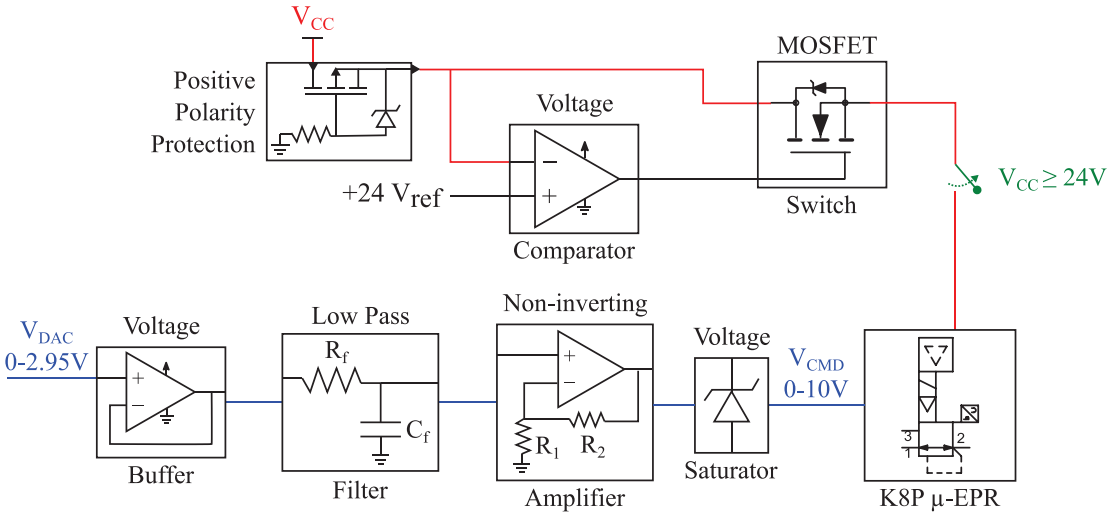

Figure 5-4: Block diagram schematic of the electronic hardware circuitry designed for the Camozzi MX-PRO EP regulator

5.2 Software Control System

The integrated embedded and interfacial software that was created and developed to operate the bulge testing device is presented at a high level in this section.

The embedded software's primary application was to automate the bulge testing procedure with minimal user intervention. The embedded software control system was written in the *C* programming language and developed using the *CooCox CoIDE* development environment which was specialised for ARM-based microcontrollers (*CoIDE* has since been discontinued).

The interfacial software's primary application was to mediate between the user and embedded system. A straight-forward Graphical User Interface (GUI) was developed to

provide a springboard application for operating the bulge testing apparatus. The interfacial software was written and developed in *MATLAB.*

5.2.1 Software Architecture

The high-level software architecture is shown in Figure 5-5. The *hardware layer* contains components that interact with the physical apparatus and environment. The *peripherals layer* is also physical but contains elements which translate the signals from the hardware layer to digital signals which may be used by the MCU. The *abstraction layer* contains MCU device firmware functions that interact with, and interpret, the peripheral signals. The *middleware layer* contains user-defined software functions which facilitate the main functionality of the software applications.

The *application layer* contains the user-defined functions which are used to carry out the primary software application functions. The application functions are those which directly produce an intended executable from the software. For the bulge testing device, these primarily include:

- Analog data measurement and monitoring
- handling serial communication instructions
- executing feedback control calculations and output
- generating and transmitting readable test output data

The *interface layer* is handled on a separate PC-based software platform. This layer provides a backend environment for test data management, as well as frontend environment for user interaction during a test. The graphical user interface (GUI) that was designed for intuitive interaction with the testing apparatus is presented in Appendix D.

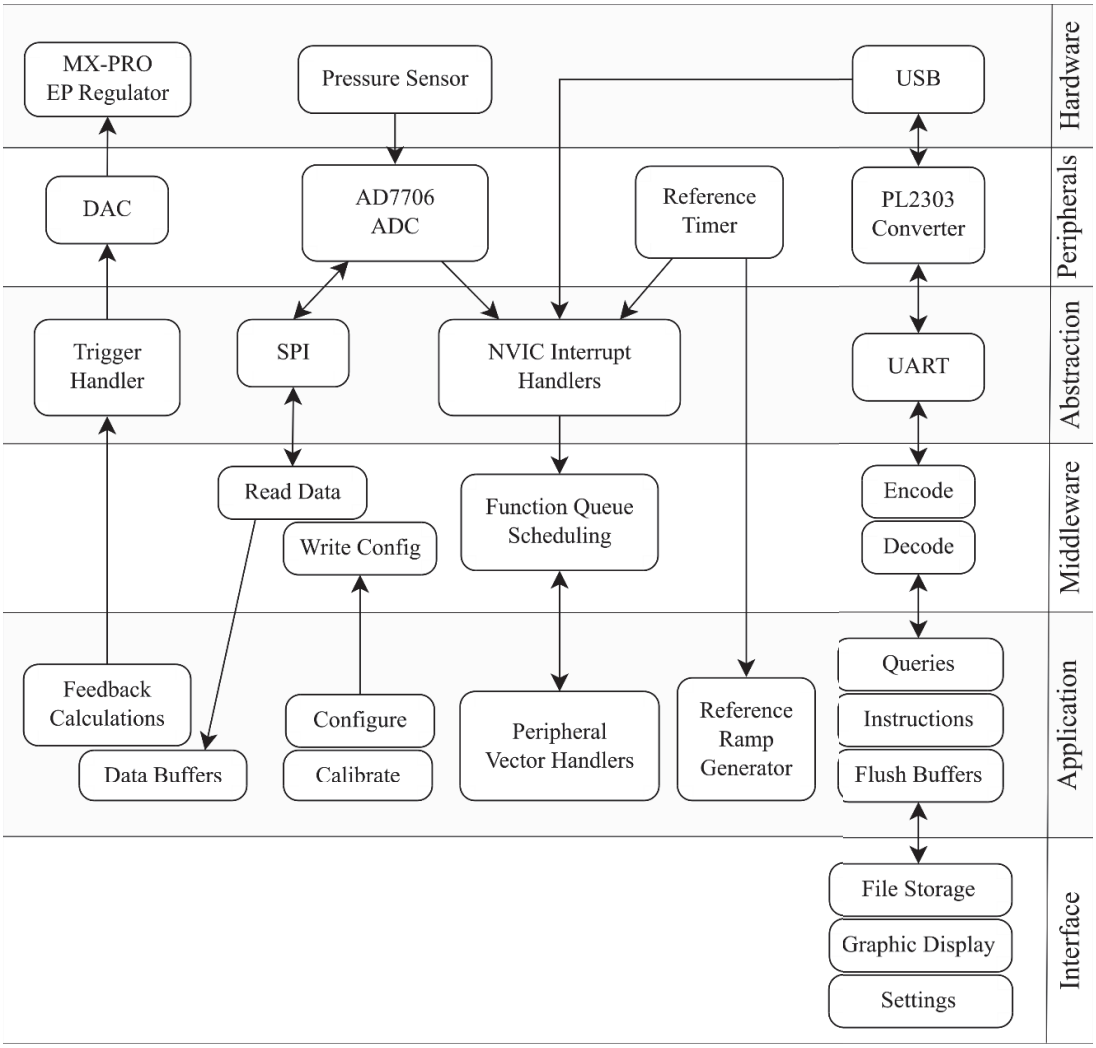

Figure 5-5: Software architecture diagram

5.2.2 Function Queue Scheduling

The embedded software architecture that was illustrated in Figure 5-5 indicates a substantial number of different application and peripheral functions and interactions to be handled. Each peripheral interaction required computational time resources, some requiring immediate action, and others which could be handled in due course. An appropriate task scheduling architecture was thus required to handle these processed expeditiously.

A straight-forward linear round-robin[5] (or round-robin with interrupts) based task scheduling approach was likely to overwhelm the software or cause it to hang, potentially

[5] In round-robin scheduling tasks are handled sequentially in a main loop without interactions [77]

resulting in a failure to perform some (or all) tasks. Therefore, a function queue scheduling approach was employed to manage task handling. Function call tasks are added to a queue and processed sequentially via a centralised handler, as and when resources are available. Critical tasks are handled immediately as they are encountered.

For example, consider the serial communications chain on the far right in Figure 5-5. A single character sent to the microcontroller via USB and interpreted by its UART driver requires immediate attention as soon as the interrupt-driven serial transmit/receive protocol initiates. Characters are read in by the UART Interrupt Service Routine (ISR) as a new character is received at the microcontroller's serial input.

During ISR handling the main loop will be paused so the routine must process rapidly to allow normal operations to resume. Once a fully received instruction is identified, it is added to a local instruction queue (it is possible that a new instruction is received before the previous instruction was processed). A call to process an instruction is added to the function callback[6] queue before exiting the ISR. Previously added queue callbacks are then handled sequentially during normal loop operation before reaching the considered instruction handling callback. Once the instruction handling callback is reach, the oldest instruction in the local instruction queue will then be processed.

5.2.2.1 Implementation

Using the method described in the preceding section, non-critical tasks could be reliably executed without sacrificing resources needed for critical functions. Non-critical tasks include (but are not limited to): data buffering, data string encoding and transmission, handling of PC-interface related queries and instructions, pressure level monitoring etc. Critical tasks include (but are not limited to): ADC data acquisition, evaluating and setting the feedback controller output, receiving serial instructions etc.

For implementation of function queue scheduling within the embedded software, the concept of peripheral vectors was employed. The term 'vector' in this context refers to a dedicated

[6] 'callback' refers to a unique user-defined function that is linked to the specific function queue insertion

function callback queue address which is assigned to each peripheral. The term 'peripheral' in this context is not only related to the hardware peripherals, but also to processes which directly interact with the interface. The peripherals that were considered during implementation were:

- ADC handles the storage and state monitoring of analog input data (see §5.2.3)
- SERIAL which handles instruction and queries from the PC interface
- REF_TIMER which handles computation of the reference ramp input signal
- BUFFER_PRT which handles encoding and transmission of test data buffers

Vector Injection

Peripheral vector injection is illustrated in the flow diagram shown in Figure 5-6. A call to add a new peripheral handling request to the function queue is called a peripheral request. When a peripheral request is called from within the code, the peripheral's vector is injected into the First-In-First-Out (FIFO) peripheral vector queue. How the peripheral request is handled once the vector is reached in that queue is governed by the callback assigned to it. Each peripheral vector is assigned a FIFO callback function queue which locates the callback function assigned to the corresponding peripheral request. In doing so, peripheral requests could be handled polymorphically which made them particularly versatile.

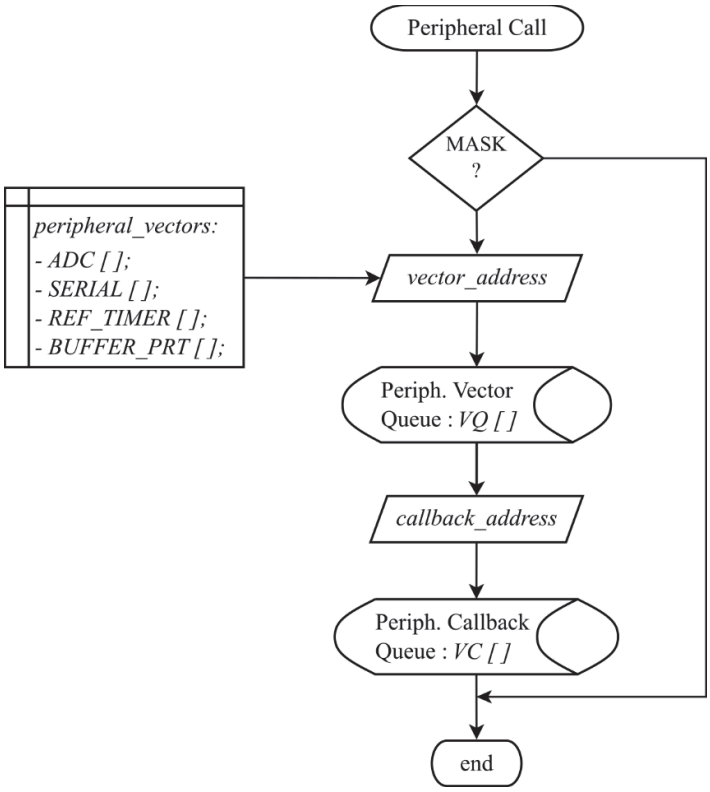

Figure 5-6: Flow of a peripheral request function queue insertion

5.2.3 Analog/Digital Data Handling

Arguably, the most critical function of the software control system was to ensure efficient and effective handling of the analog pressure input data. This affected collection of bulge test pressure data, feedback controller efficacy, rupture detection, and threshold pressure detection.

The ADC data handling implementation is illustrated by the flow diagram shown in Figure 5-7. When the ADC has new data available a notification pin is driven low which triggers the ADC ISR. An ADC peripheral request is added to the peripheral vector queue which is mapped to the ADC callback function. The new ADC data is read into temporary storage and the notification pin is thereby reset, ensuring that the most recent ADC measurement data is always available.

Once the ADC vector is reached in the vector queue, the ADC callback is launched. The newest data in the temporary storage is then written to multiple ADC data buffers. A flag is

set notify that new analog system output data is available for feedback controller output computation. A new ADC peripheral request is made during the current vector callback which is mapped to an ADC monitoring callback.

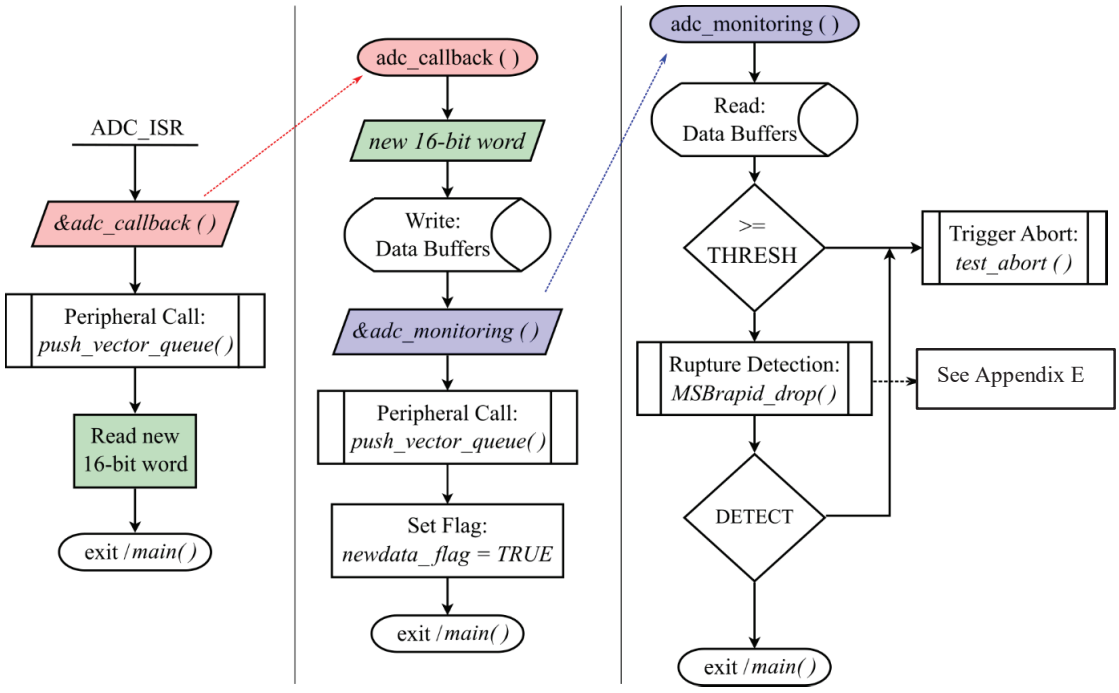

Figure 5-7: Flow diagram of ADC data handling implementation

5.2.3.1 Threshold Monitoring

The ADC monitoring callback is launched upon reaching the subsequent ADC vector. Data from the ADC buffers are operated on to monitor threshold criteria. If the callback routine identifies that the termination pressure has been exceeded, or that a rupture has been detected[7], termination proceedings are immediately initiated. This exhausts all pressure, flushes all buffers to the PC-interface one last time, shuts down peripherals, and then notifies the PC of termination so that it may initiate its own termination and clean-up operations.

[7] Rupture is identified when a sustained reduction in the Most Significant Byte (MSB) from the historical maximum is reached

5.2.4 Practical Task Scheduling with Feedback Control

Peripheral vector handling is shown in the context of the main bulge testing operating platform's software application in Figure 5-8. The loop diagram illustrates the main software loop during an active ramp test, subsequent to any system initialisations, calibrations, and configurations which take place initially.

The feedback control is tasked in sequence with peripheral vector queue handling in a round-robin configuration. Feedback control is therefore given high prioritisation; for every vector that is handled, the feedback control routine is polled and run if new data is ready. The feedback controller output is then computed as per the feedback controller difference function that was described in (§4.4) note: K_p and K_e are proportional constants that are evaluated from the custom user GUI controller specification). The control output is then converted to a 10-bit DAC analog output signal which controls the EPR pressure regulation.

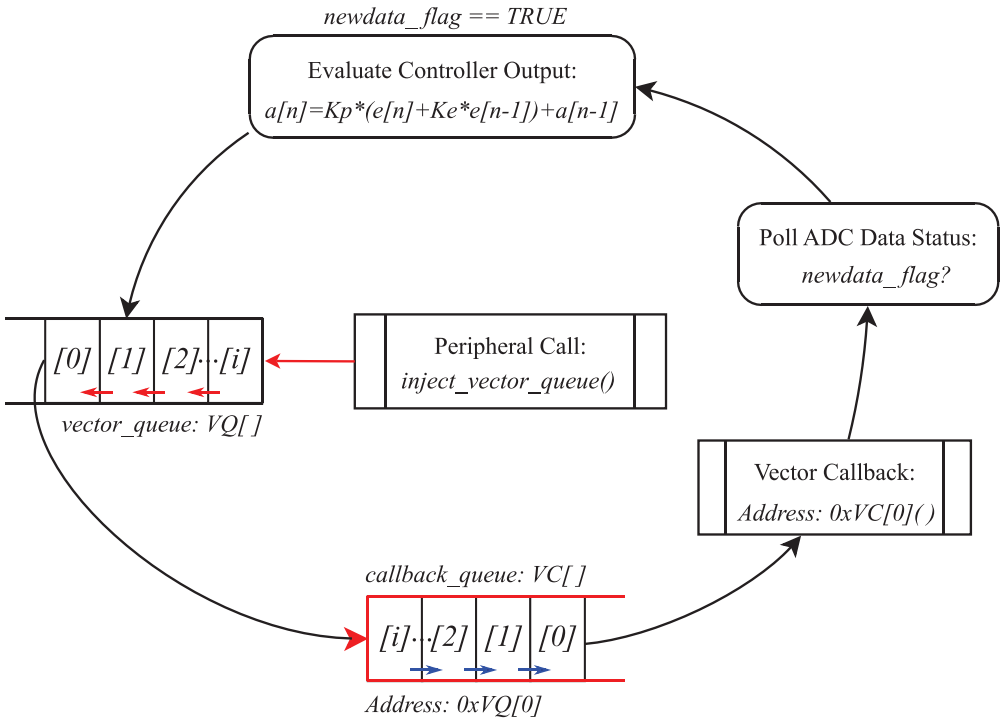

Figure 5-8: Active testing control loop with function queue scheduling

5.2.5 Serial Interfacing

Serial communication between the PC and microcontroller was handled via Universal Asynchronous Receiver/Transmitter (UART; see Figure 5-5). All serial communication events between the PC and controller and vice versa required a returned acknowledgement of the received data from the receiver to the transmitter. Instead of an acknowledgement, the receiver could also request retransmission of the last packet if there was an issue in decoding the data received. The measured latency of the maximum transmittable data packet size that could be received / transmitted by the microcontroller was used to calibrate a timer on both devices that would retransmit unacknowledged data packets up to three times.

Experimental data that was transmitted from the microcontroller to the PC was sent in data packets containing about 200ms worth of measurement data (10 – 15 samples) which were sent as hexadecimal values. These data packets had reserved overhead that stated the source of the data, a start and end time stamp, and the number of data points that should be expected for the transmission. The PC received these packets, decoded the data points, and compared this to the number of expected data points that were specified in the overhead. If the number of data points match the PC requested a retransmission of the data. A serial printing queue was implemented in the microcontroller software to accommodate overlapping retransmissions of failed data packets and new data packets.

5.3 Summary

The selection of the control and measurement instrumentation that was used in the bulge testing platform, and the design of the related electronic and software interfaces were discussed in detail. Output from an interchangeable 4 – 20 mA pressure transducer was converted to a sensible 0 – 5V signal using a current to voltage converter circuit. Practical measurement of the 0 – 5V pressure signal was performed using a 16-bit ADC which was used to perform PI controller calculations and transmit pressure-time data to a host PC filing system for display and storage. Continuous pressure monitoring was implemented to detect over-pressure and rapid pressure drop caused by specimen rupture and automatically purge pressure and terminate the test. A 10-bit DAC and basic voltage amplifier circuit were used to convert a

computed PI controller output to a $0 - 10$V control signal that was used to automatically set the EPR actuator's pressure level in the feedback control circuit.

The majority of the automated control tasks were performed on a single 168MHz, 32bit STM32F4 microcontroller. The software architecture was centred around task queuing which was designed and implemented in the embedded software to serially manage the many (often overlapping) software operations which needed to be carried out on the controller.

Chapter 6

Platform Commissioning Testing

This chapter presents the methodology, results, and critical discussion for practical tests which were performed to assess and characterise the performance of the fully realised bulge testing platform. Pressurisation rate control tests were performed on silicone rubber sheet specimes to examine the efficacy of the customisable feedback control system which was designed and implemented. Rate tracking compliance is compared and analysed for a range of pressurisation rates between 2kPa/s and 20kPa/s. Feedback control system performance is concurrently compared and analysed for various open-loop plant response speed design conditions.

Further tests were performed to rupture on neoprene rubber sheet specimens to measure as a precursor to eventual intended skin tissue testing, using the described platform to collect mechanical stress-strain data. Results which were collected using the unestablished bulge testing platform and with the established uniaxial tensile tests are presented and compared. The performance of the considered bulge testing platform is evaluated as a reasonable mechanical material testing platform.

6.1 Platform Overview

The flow chart presented in Figure 6-1 provides a high-level representation of the flow of activities for the bulge testing platform that has thus far been developed and described. The practical tests that are presented in this chapter were performed to ensure adequate and repeatable operability and performance of the platform.

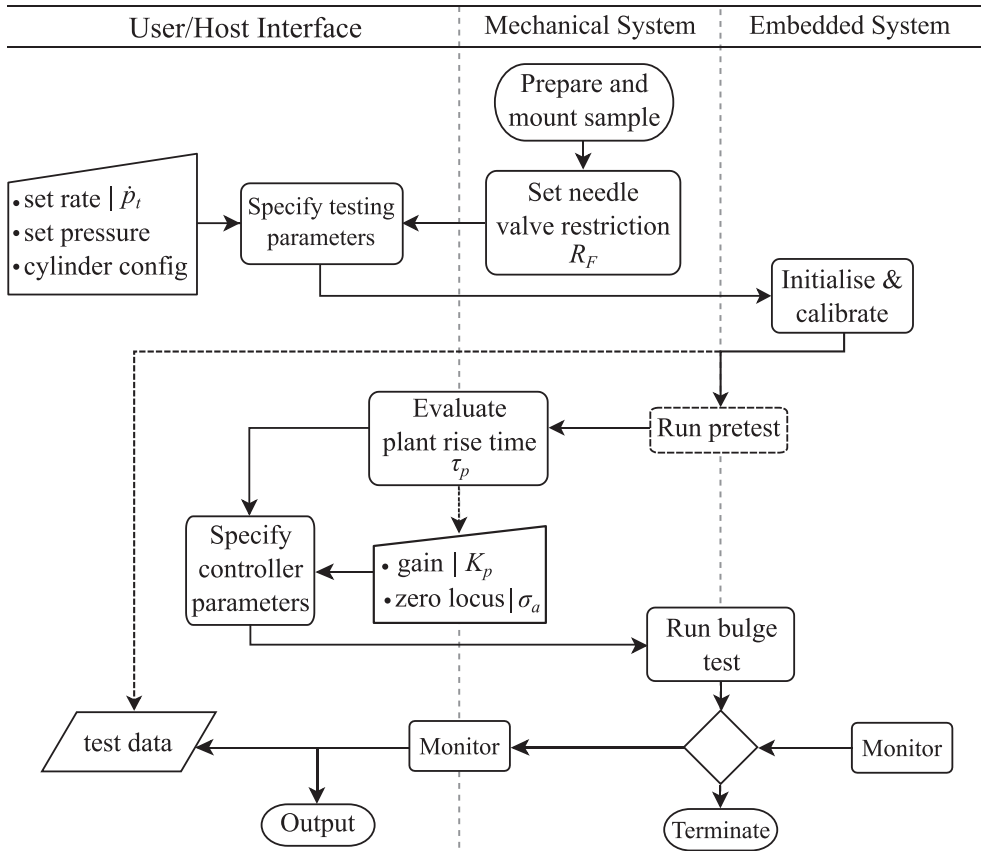

Figure 6-1: Platform evaluation testing flow chart

6.1.1 Operating Methodology

Comprehensive operating instructions are provided for the bulge testing device in Appendix D. The reference pressurisation rate $\dot{p}_t$, and termination pressure were manually specified at the user interface for each test. Thereafter the plant response speed design point was manually adjusted by varying the inlet flow restriction of the needle valve R_F, where

$$0 \leq R_F \leq 1 \quad \begin{array}{l} 0 = \text{Fully Open} \\ 1 = \text{Fully Closed} \end{array} \tag{6.1}$$

An optional integrated pretest routine was then run if the initial plant response time was unknown, where a small pressure step input was applied and held for five seconds, then released. The corresponding step response was treated as first-order with response given by

$$p(t) = p_{final} + \left(p_{inital} - p_{final}\right) e^{-t/\tau_p} \tag{6.2}$$

where τ_p is the unknown plant response time. An automated routine (described in Appendix E) was then fitted to the raw pretest data in order to determine the plant response time.

Appropriate controller gain and zero locus parameters (K_p and σ_a respectively) were programmatically identified by the PC interface software using the controller design chart produced in (§4.3.4). Parameters were identified for the fitted τ_p estimate within the prescribed $0.7 \leq \xi \leq 0.9$ damping ratio range and manually specified at the user interface. The embedded feedback controller difference function was automatically customised, and test configuration data (variable ID's, calibration offsets etc.) were relayed back to the PC interface.

The minimum realisable EPR output was set and held until the signal settles. Thereafter contiguous closed-loop feedback control is initiated for the specified pressurisation rate. Control system output data was routinely sent from the MCU to the PC interface where it was decoded, identified, stored, and displayed.

Automatic termination was initiated by the embedded software control system when either prescribed termination pressure was detected or when a rapid pressure drop was detected by the rupture detection monitoring routine (described in Appendix E). Notification of termination was relayed to the PC interface whereupon test data was collated and stored in the PC's filing system into a single .txt file.

6.2 Pressurisation Platform Repeatability

Initial pressurisation tests were performed to ensure repeatable operation of the platform as it was described in the preceding section, and to identify any potential issues prior to formal testing. The tests were performed on 2.25mm thick, ∅50mm circular silicone rubber sheet samples at pressurisation rates 2, 5, 10, 20 kPa/s at flow restrictions 0, ¼, ½, ¾ respectively. Supplementary repeatability tests are also provided in Appendix F for substantiation purposes.

6.2.1 Mechanical System

A typical bulge test is shown *in situ* at various stages in Figure 6-2. Volumetric capacity supply issues were identified when air was used as the pressurised medium in the upper cylinder. The piston reached the end of its stroke before reaching the full pressure output potential of the device. Some gas leakage was identified between the sample and clamping ring. Gas leakage was reduced using *ad hoc* gaskets but did not completely resolve the issue.

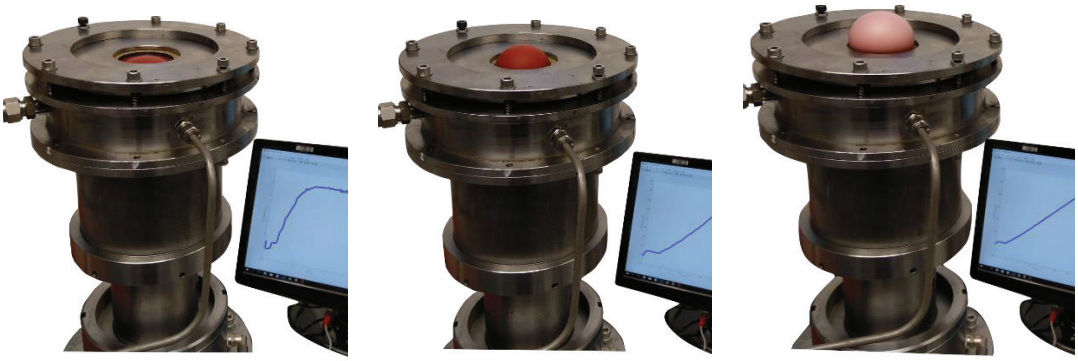

(c) (b) (c)

Figure 6-2: In situ pressurisation rate control test for an arbitrary silicone sample
(a) uncontrolled step-in phase (b) feedback-controlled phase (c) end of piston stroke

6.2.2 First-Order System Parameter Identification

The pretest step response output and fitted first-order response results are shown for the repeatability tests in Figure 6-3 . The fitted data indicated satisfactory visual agreement with the pretest data. Plant response time increased with increasing flow restriction as intended. The maximum output pressure decreased with increasing flow restriction, and a short period of inactivity was observed between the supply opening and initiation of the response. It was presumed that friction between the piston seals and cylinder was more difficult to overcome with reduced inlet flow, resulting in these observations.

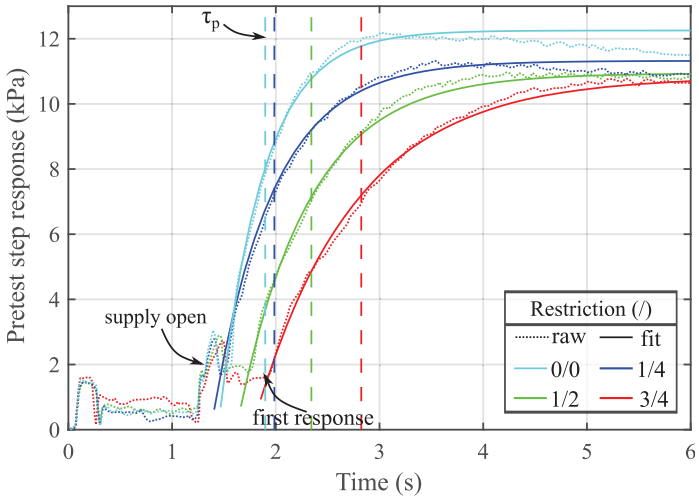

Figure 6-3: Pretest step responses and fitted responses for various flow restrictions

6.2.3 Controlled Pressurisation

Appropriate feedback controller parameters were selected and specified for the respective plant response times indicated in Figure 6-3. The pressure output results and corresponding feedback controller output signals are shown in Figure 6-4. Repeatable contiguous transitions from initial open-loop control to closed-loop feedback control was observed. Adequate rate tracking was observed thereafter in all cases. All tests terminated automatically upon reaching termination pressure as intended. Rupture identification tests are presented in Appendix F for substantiation purposes.

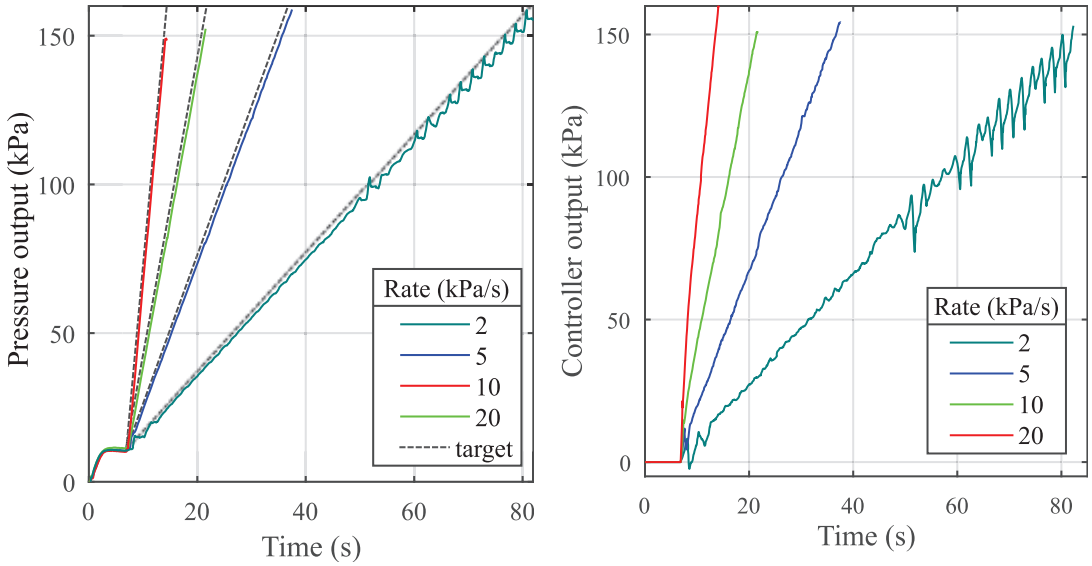

Figure 6-4: Controlled pressurisation repeatability test results

6.3 Pressurisation Rate Control Tests

The closed-loop feedback PI controller which is described in 0 was designed to track a user-specified bulge pressurisation rate. Pressurisation rate control tests were performed to evaluate the compliance of the digital control system to track a range of constant pressurisation rates. The efficacy of the customisability of the feedback controller design strategy was concurrently assessed in a controlled manner by modifying the plant response speed using the installed needle valve to retard flow.

6.3.1 Methodology

Tests were performed on arbitrary 2.25mm thick ∅50mm silicone rubber sheet samples. The initial sealed cylinder air volume was used as the loading medium to expediate testing and also guard unprotected electronics from potential water damage in case of specimen rupture.

Four series of rate control tests were performed at increasing targeted pressurisation rates

$$\dot{p}_t = \{2, 5, 10, 20\} \text{ kPa/s} \tag{6.1}$$

The plant response speed was incrementally reduced by manually increasing the restriction of the needle valve on the pneumatic inlet in four equal increments per rate series,

$$R_F = \{0, ¼, ½, ¾\} \tag{6.2}$$

The first order plant response time was identified for each rate and flow restriction configuration during respective pretest routines. Appropriate feedback controller parameters were identified and specified at a damping ratio of $\xi = 0.9$ for each fitted plant response time. The tests were automatically terminated at a pressure of 200kPa to ensure the tests would terminate automatically before running out of volumetric supply capacity.

6.3.2 Results

The plant response time estimates that were identified for each testing configuration in Table 6-1. The corresponding feedback controller parameters which were selected for the respective pressurisation test are provided in Appendix F**Error! Reference source not found.**.

Table 6-1: Summary of the fitted first order plant response time estimates from pretests

R_F	$\dot{p}_t$ (kPa/s)	Plant Response Time | τ_p (s)			
		2	5	10	20
0		0.43	0.44	0.42	0.43
¼		0.55	0.58	0.58	0.58
½		0.68	0.68	0.67	0.66
¾		0.97	0.98	0.95	1.00

The pressure output signals for the rate control tests from 2kPa/s to 20kPa/s are presented in Figure 6-5 to Figure 6-8 respectively. The first and last five seconds are magnified to show the initial transient behaviour and steady-state behaviour respectively. A best fit straight line was fitted to the final 25% of tests data which was assumed to be in steady state. The results are shown only for the feedback-controlled phase (after initial settling of the minimum regulator output was detected).

Results for the 2kPa/s and 5kPa/s test series are shown in Figure 6-5 and Figure 6-6 respectively. The 2kPa/s rate produced sawtooth shaped pressure signals which became more significant at more advanced stages of the tests. Physically this manifested repeatedly as a rise in pressure followed by a quick release of pressure. The 5kPa/s rate produced noticeably smoother pressure signals compared to the slower rate tests, however distinct discrete steps were still recognisable. The pressure output and reference input signals can be seen to diverge from one another as the tests progress.

Results for the 10kPa/s and 20kPa/s test series are shown in Figure 6-7 and Figure 6-8 respectively. Smoother pressure signals were produced at these rates. Degradation of signal quality or divergence of the output signal from the reference signal at advanced stages of a test were not prominent. The 20kPa/s results indicate a clear improvement in steady-state refence signal error with increasing flow restriction.

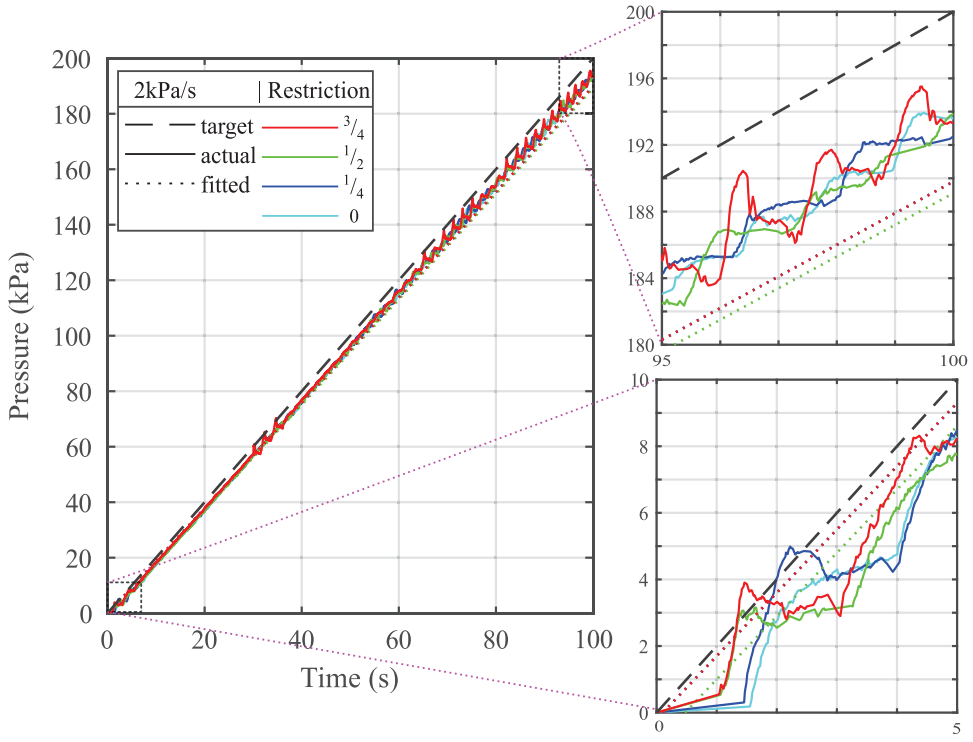

Figure 6-5: System output pressure history - 2kPa/s

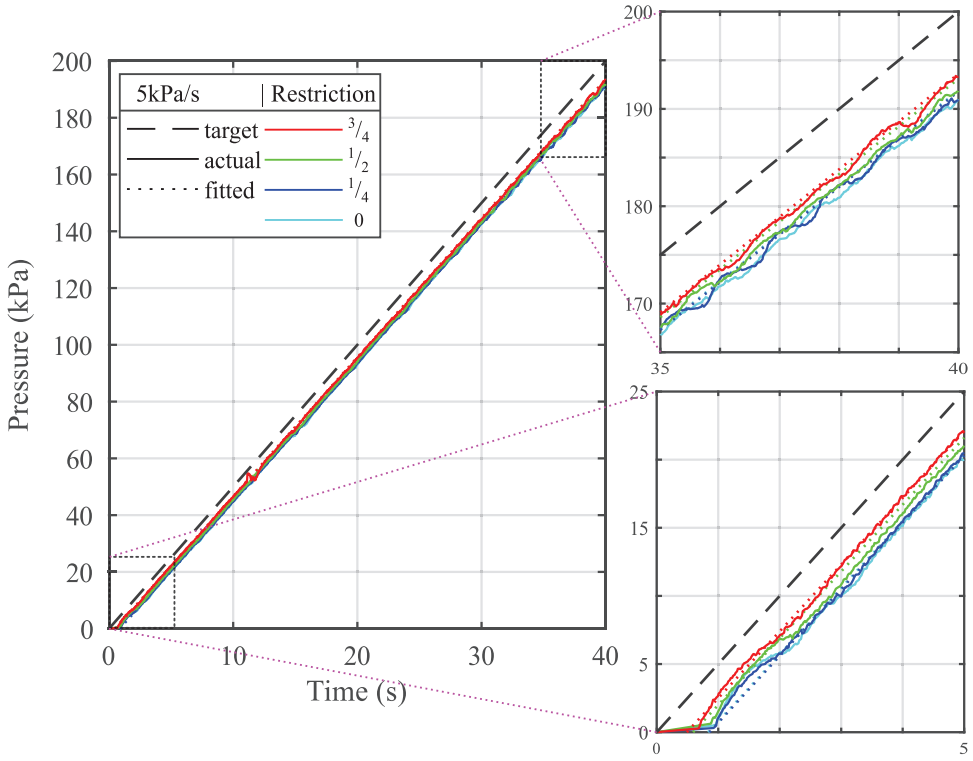

Figure 6-6: System output pressure history - 5kPa/s

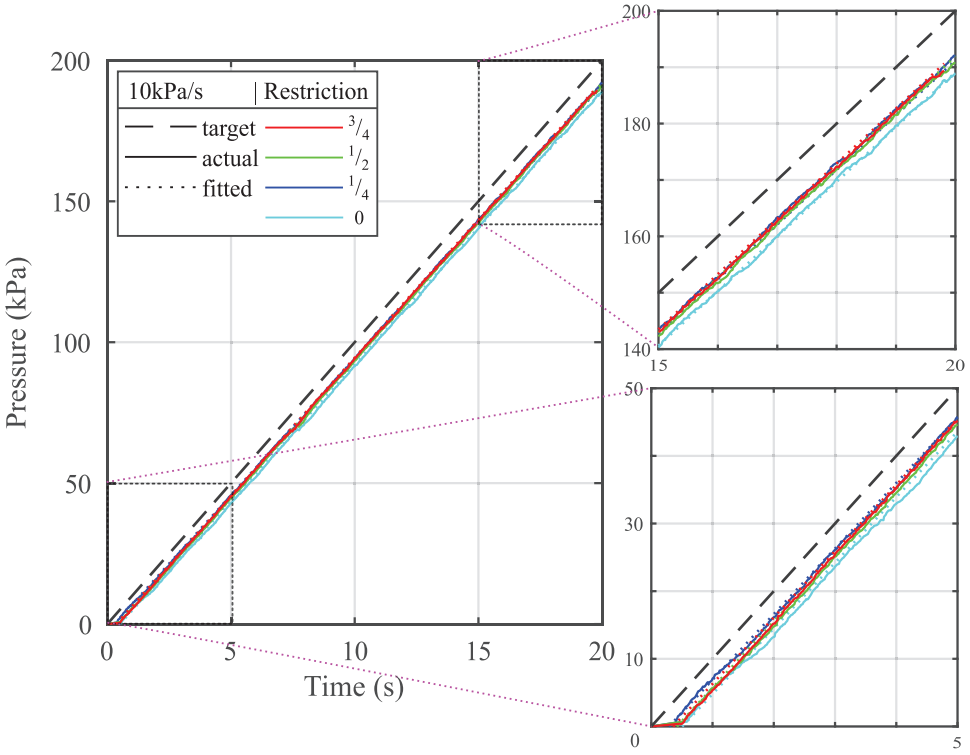

Figure 6-7: System output pressure history - 10kPa/s

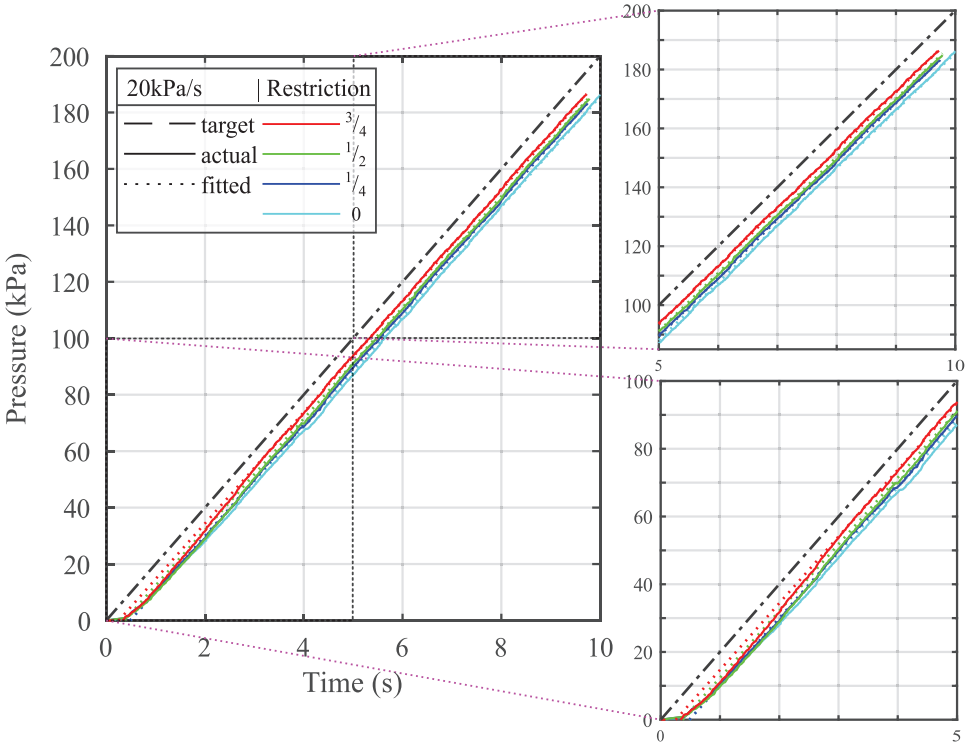

Figure 6-8: System output pressure history - 20kPa/s

The steady-state rates that were achieved are summarised in Table 6-2. The rates were measured from the gradient of the fitted linear data for each test. The results indicate highly satisfactory pressure rate tracking with no more than a 5% deviation from the expected rates, all slightly underperforming relative to the specified rates.

Table 6-2: Summary of measured steady-state pressurisation rates

$\dot{p}_t$ (kPa/s)	R_F	Measured Rate [a] | $\dot{p}_t$ (kPa/s)				% Error (approx.)			
		0	¼	½	¾	0	¼	½	¾
2		1.9	1.9	1.9	1.9	-5	-5	-5	-5
5		4.8	4.8	4.9	4.9	-4	-4	-2	-2
10		9.7	9.7	9.8	9.8	-3	-3	-2	-2
20		19.7	19.7	19.8	19.5	-1.5	-1.5	-1	-2.5

[a] measured from linear best fit gradient ($R^2 > 0.98$; except for 2kPa/s at $R^2 \approx 0.93$)

A typical second order system ramp response is illustrated in Figure 6-9. Output lag τ_{ss} is the time-axis offset between the constant-rate steady-state system output and reference input. The unit ramp error $\hat{e}_{ss}$ is an equivalent steady-state error for a unit ramp input. These are given respectively by the following expressions

$$\tau_{ss} = \frac{e_{ss}}{\dot{p}_t} \tag{6.3}$$

$$|\hat{e}_{ss}| = |\tau_{ss}| \tag{6.4}$$

The lag can provide an estimate of the time taken for the signal to reach steady, where

$$t_{ss} \approx 4\tau_{ss} \tag{6.5}$$

is the estimated time to steady state for a second order control system.

Table 6-3 shows the predicted unit ramp error for the different control systems, customised according to the different plant response times shown in Table 6-1. Recall from 0 that the predicted steady-state error $e_{ss} = \frac{1}{K_p \sigma_a}$ was only related to the controller parameters that were chosen. Theoretically, the lag and unit ramp error magnitudes should be equivalent. The predicted steady-state performance results indicate an improvement in both error and lag performance are expected with increased plant response time.

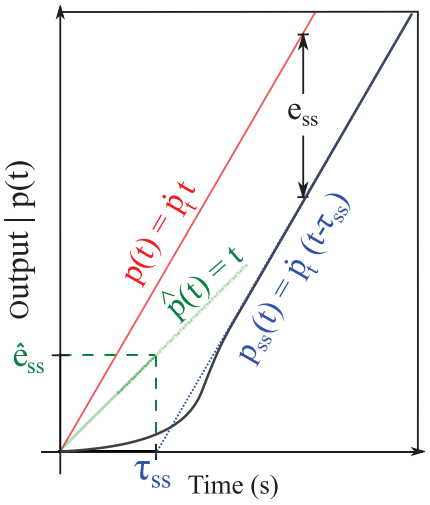

Figure 6-9: Typical closed-loop feedback control system ramp response

Table 6-3: Predicted steady-state performance results

$\dot{p}_t$ (kPa/s)	Unit Ramp Error *or* Lag | $\hat{e}_{ss}$ (Pa) *or* τ_{ss} (s)				
	R_F	0	¼	½	¾
2		0.60	0.45	0.40	0.25
5		0.60	0.44	0.38	0.26
10		0.57	0.44	0.37	0.26
20		0.60	0.46	0.37	0.27

The measured steady-state results are summarised in Table 6-4. The measured and unit ramp error and lag were significantly different for slower rates, showing some improvement in comparability towards higher rates. The measured mean unit error measurements were ostensibly higher than predicted, but did present the anticipated improvement with increasing flow restriction. The results also indicated a significant improvement in steady-state error with increasing rates. The measured lag results did not correlate and did produce any immediately useful information.

Table 6-4: Measured steady-state performance results

$\dot{p}_t$ (kPa/s)	Mean Unit Ramp Error [a] | $\overline{\hat{e}_{ss}}$ (Pa)					Lag [b] | τ_{ss} (s)			
	R_F	0	¼	½	¾	0	¼	½	¾
2		3.15	3.09	3.26	2.96	0.10	0.10	0.45	0.10
5		1.80	1.76	1.60	1.38	0.82	0.84	0.58	0.48
10		1.11	0.81	0.91	0.81	0.49	0.28	0.41	0.35
20		0.72	0.58	0.53	0.39	0.25	0.37	0.48	0.47

[a] error measured between predicted response and corresponding physical output signal

[b] measured from linear best fit x-axis intersection ($R^2 > 0.98$; except for 2kPa/s at $R^2 \approx 0.93$)

6.3.3 Analysis and Discussion

Comparison of the pressure signal results presented in Figure 6-5 to Figure 6-8 indicated improvement in the signal quality with increasing rate. This was presumed to be caused by the output resolution of the EPR actuator which was originally treated as an ideal linear component for control system modelling simplification. Diagnostic simulations were subsequently run on the original control loop in Simulink, but with a 5kPa resolution actuator (as per device specification). Comparison of the simulated and real outputs shown in Figure 6-10 indicate comparable behaviour for each rate.

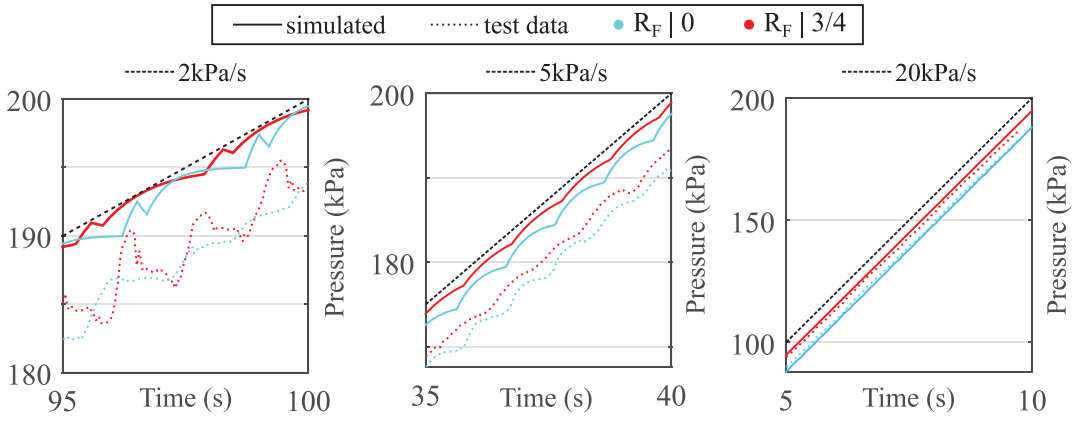

Figure 6-10: Comparison of simulated and physical response with a 5kPa actuator resolution

The results shown in Figure 6-10 substantiate the presumption that the varying quality of the pressure signal was primarily linked to the actuator resolution. The error term rises and accumulates in the integrator; the actuator output remains unchanged until the next

resolution step. When the next resolution step is reached the output component in the error signal drops rapidly as the reference signal component rises.

At the slowest rate (2kPa/s) the accumulated error between resolution steps is not sufficient to compensate for the drop in error after a step. The controller signal drops below the current sensible actuator input level before rising sufficiently to reach the next sensible step. At the intermediate rate (5kPa/s) the controller signal does not drop below the sensible actuator input as the refence signal is just fast enough to compensate for the error signal swing. At the highest rate (20kPa/s) the reference signal rises fast enough to compensate for the swing in error caused by the discrete step without producing any noticeable resolution effects.

In Figure 6-10 it is noticeable that reducing the response speed of the plant improves the signal quality. In this case the drop in error signal is less dramatic when a new resolution step is reached, thereby giving the controller time to respond to the swing in the error signal. While performance at low rates showed deterioration, time constraints limited detailed investigation of this phenomena.

The initial controller design was based on the system performing within a prescribed damping ratio band. System damping is a difficult quantity to practically evaluate from a ramp response. Instead, the Integral of the Absolute unit ramp Error signal (IAE) was used as a comparative performance indicator for the control system, where

$$\mathrm{IAE} = \int_0^{t_{end}} |\hat{e}(\tau)| \mathrm{d}\tau \tag{6.6}$$

The absolute unit ramp error signal was reconstructed as is illustrated in Figure 6-11 (for a full set of resultant signals refer to Appendix F). The IAE results are shown in Figure 6-12 for the modelled control system and for the practical results. Results are shown for the minimum and maximum rates and respective minimum and maximum flow restrictions.

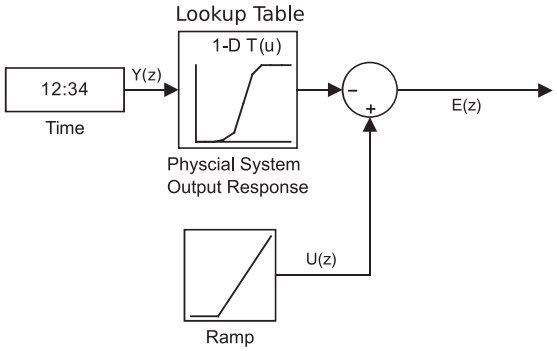

Figure 6-11: Reconstruction of error signal from the physical system output results

The IAE results were expected to be linear with time during steady-state since steady-state error for a *type 1* control system with a ramped input is constant. However, a nonlinear rise in the IAE was observed which indicated a divergence of the output and reference signals (refer to Figure 6-5 and Figure 6-6 respectively).

The deviation in reference ramp input tracking was found to be caused by a small proportional calibration error for an embedded software timer which was used to perform reference ramp input signal calculations. The generated reference signal was therefore at a slightly lower rate than specified. The apparent deterioration in IAE performance that was observed with decreasing rate was thus exacerbated by the increased test duration.

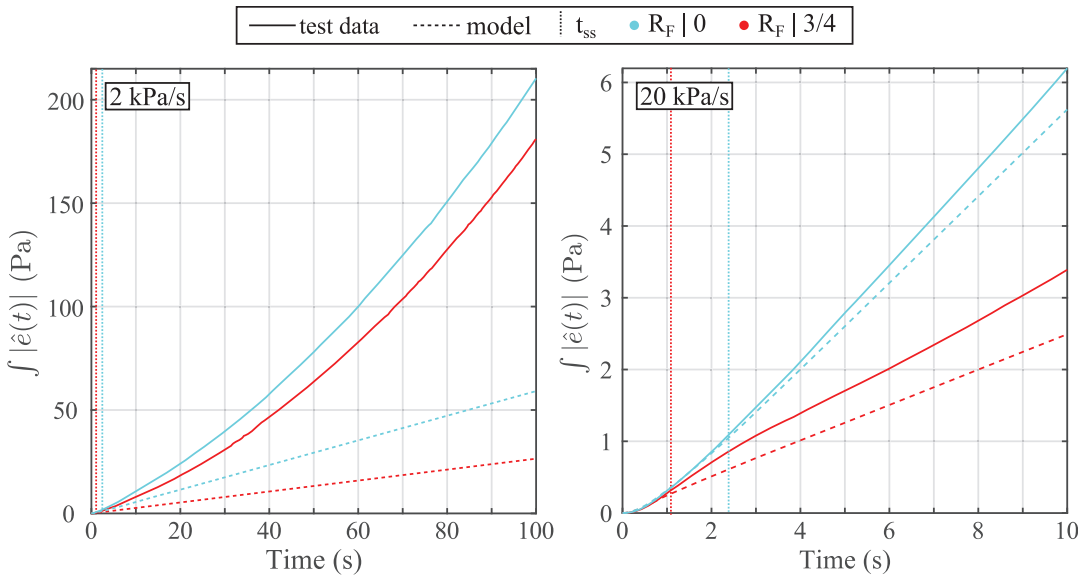

Figure 6-12: Integral absolute error for rate control tests showing divergence from control system model performance

6.4 Mechanical Material Tests

Mechanical material tests were performed to assess the functionality of the device as a mechanical experimentation platform. The objective of the tests was to collect and compare biaxial tensile mechanical data obtained using the implemented bulge testing device with data collected using ASTM D412-16 [70], for tensile testing of vulcanised rubber and elastomers, as the relevant test method. Large variances in mechanical response and properties which have been observed for skin tissue in the literature meant it was not feasible to perform tests on skin or skin synthetics without first assessing the platform under more predictable conditions. All tests were performed on commercially sourced generic neoprene rubber sheet which behaves as an isotropic hyperelastic material.

6.4.1 Mechanical Testing Methodology

Tests were performed using neoprene rubber sheet specimens cut from a single 1.75mm thick sheet. This material configuration was chosen as it could be successfully taken to rupture before running out of compressed gas capacity in the upper cylinder. Specimen geometries for the testing configurations described subsequently are presented in Appendix G.

Uniaxial tensile tests were performed according to the standard procedure prescribed in the discussed ASTM standard. Tests were performed on an Instron tensile testing machine at an extension rate of 50mm/min. Axial extension was measured using a clip-on extensometer.

Equibiaxial tensile tests were performed on the bulge testing device platform. Tests were performed on circular ∅50mm specimens at various pressurisation rates (2, 10, 20 kPa/s). Vertical deformation was measured at the bulge apex using a 1D laser range measuring device, as described in the proceeding subsection.

6.4.1.1 Biaxial Deformation Measurement

The out of plane of biaxial deformation measurements for bulge tests should be measured using 3D DIC methods for the best results. This method can provide detailed planar deformation measurements that may be used to extrapolate stress and strain fields across the

entire specimen, as well as identify curvatures that can identify the collagen fibre orientations. At the time of commissioning testing 3D DIC cameras were not available for testing purposes. A compromise was made to use a simple laser displacement sensor to collect apex deflection data for isotropic materials to use as basic validation of the performability of the bulge testing platform.

As only isotropic material samples were considered, stress could be evaluated from vertical bulge displacement deformation data. Apex displacement was measured with an ST Electronics VL53L0x infrared laser time-of-flight range sensor evaluation module as illustrated in Figure 6-13 (description of the device's operation is presented in Appendix G). A white target disc was glued to a 3D printed concentric concave platform to provide a planar target covering the sensor's 25° field of view. The target platform was affixed to the specimen with a wet glue in an aim to provide stability to the target. This method was *ad hoc* due to time constraints but was adequate when applied carefully. Apex deflection δ was measured relative to the full-scale measurable range h.

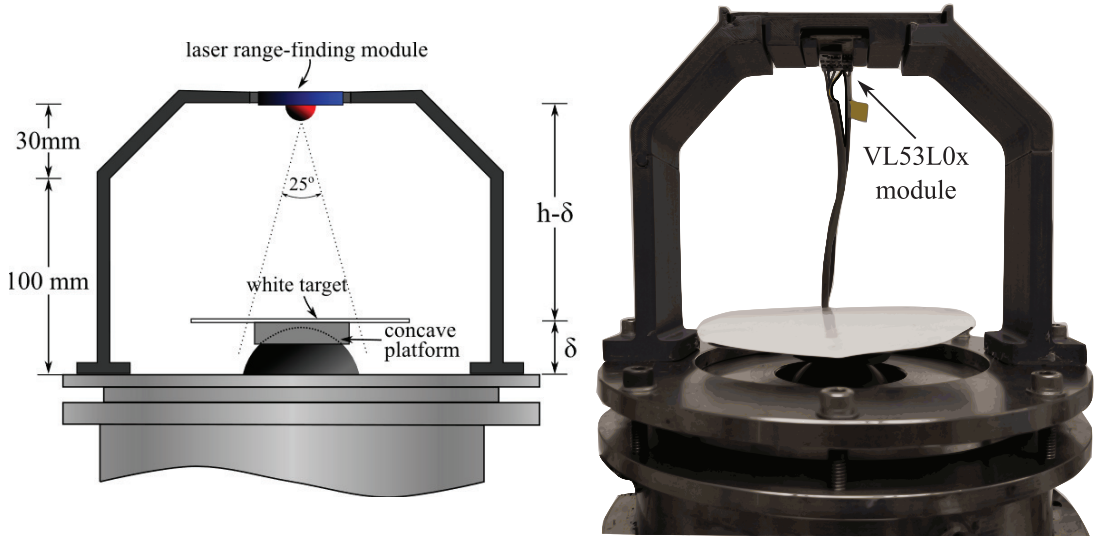

Figure 6-13: Bulge apex displacement measurement setup

(left) schematic of the configuration (right) photo *in situ*

6.4.2 Basic Model Parameter Identification Methodology

To compare the quality of the uniaxial and biaxial tensile test data, basic Mooney-Rivlin hyperelastic model fitting was performed on the test data. The Mooney-Rivlin strain energy density function can be written in terms of principal stretches

$$W_{mr}(\lambda_{1,2,3}) = C_1\left(\sum_{i=1}^{3}\lambda_i^2 - 3\right) + C_2\left(\sum_{i=1}^{3}\lambda_i^{-2} - 3\right) \tag{6.7}$$

which is equivalent to a two term Ogden hyperelastic material. The first term in (6.7) describes the small-strain response of the material, and the second term describes strain hardening.

Cauchy stress for a Mooney-Rivlin hyperelastic material in uniaxial tension can be shown to be given in terms of the principal stretch in the loaded direction, as follows

$$\sigma_1^{mr} = 2C_1(\lambda_1^2 - \lambda_1^{-1}) - 2C_2(\lambda_1^{-2} - \lambda_1) \tag{6.8}$$

Cauchy stress for a Mooney-Rivlin hyperelastic material stress for a spherically deformed specimen in equibiaxial tension can be shown to be given in terms of the stretch in either of the principal circumferential directions ϕ, θ

$$\sigma_{\phi,\theta}^{mr} = 2C_1\left(\lambda_{\phi,\theta}^2 - \lambda_{\phi,\theta}^{-4}\right) - 2C_2\left(\lambda_{\phi,\theta}^{-2} - \lambda_{\phi,\theta}^4\right) \tag{6.9}$$

The unknown coefficients were identified by applying non-linear least squares to the experimental data in order to solve for the minimisation function

$$Q = \sum_{i=1}^{n}[\hat{\sigma}(\boldsymbol{c}, p_i) - \sigma_i]^2 \tag{6.10}$$

For which the unknown search parameter vector $\boldsymbol{c}$ is sought for the analytical stress vector $\hat{\sigma}(\mathbf{c},\mathbf{p})$ with independent variable vector $\boldsymbol{p}$ to match the experimental stress vector $\boldsymbol{\sigma}$ results as closely as possible. This was performed using MATLAB's *lsqnonlin* nonlinear least squares regression solver function.

6.4.3 Results

Results collected from uniaxial testing are presented first, followed by biaxial testing results collected using the proffered bulge testing device. The complete set of the fitted data and results for the tests are provided in Appendix G.

6.4.3.1 Uniaxial Tensile Tests

True stress for the uniaxial tensile tests was evaluated by the following for applied load F

$$\sigma_1^{exp} = \frac{F}{A_0}\lambda_1 \tag{6.11}$$

where A_0/λ_1 is the instantaneous cross-sectional area for an incompressible isotropic extension. The stress-stretch response results for the uniaxial tensile tests are shown in Figure 6-14. Visually the results were grouped well together, especially at lower strains. The shape of the responses were repeatable, but the points at which failure occurred varied appreciably. The failure stresses and strains fell within a 4.9 - 6.6 MPa and 170 - 220% range respectively. The fitted average-parameter model fit is also shown in Figure 6-14. Mooney-Rivlin model parameters were evaluated for each test and averaged overall (see Appendix G)

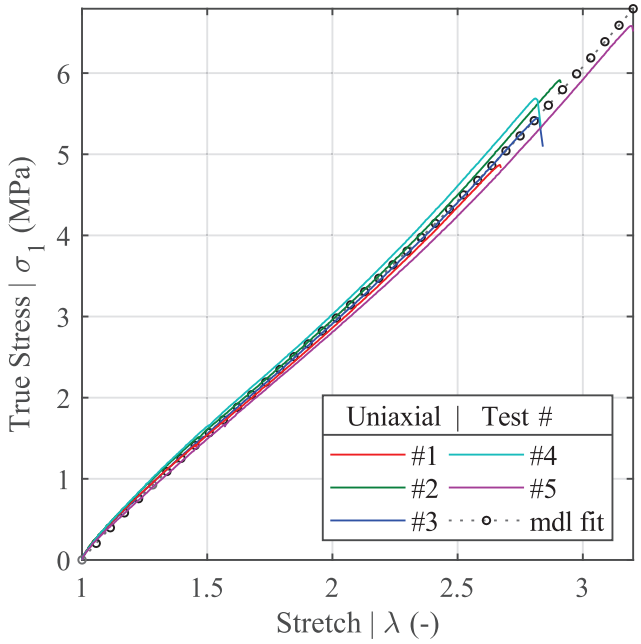

Figure 6-14: Uniaxial tensile test stress-stretch results

showing the data spread bounds and average Mooney-Rivlin model fit

6.4.3.2 Equibiaxial Bulge Tests

Raw pressure transducer and laser displacement sensor signals for the bulge tests are shown in Figure 6-15. The signals are shown normalised with respect to the maximum time and data components of each signal in order to compare the quality of the signals on a comparable scale. The pressure sensor produced clean signals that presented little appreciable noise. At the lowest rate the smoothness of the signals was disrupted due to the actuator resolution effects which have been discussed. The laser displacement sensor produced signals that presented substantial signal noise due to poor resolution characteristics of the sensor.

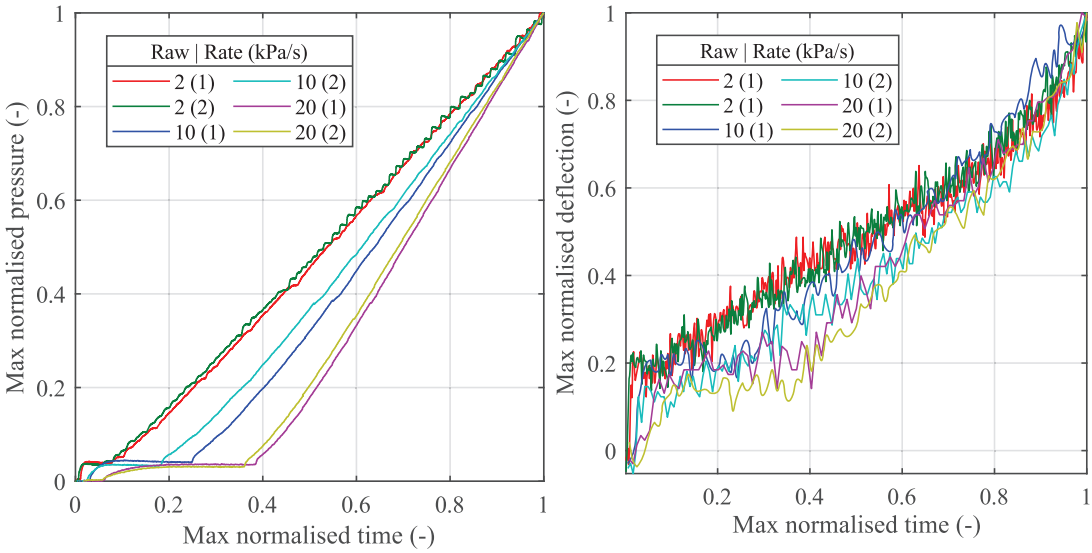

Figure 6-15: Raw pressure and apex deflection signals (max normalised on both axes)

The displacement data was smoothed using a moving average filter (refer to Appendix G). An average sample window size equivalent to 5% of the total sampled data length was applied. The first 10% of the data was smoothed less aggressively to reduce the impact of intrinsic historical filter errors. The filtered deflection-pressure response results are shown in Figure 6-16. The samples ruptured consistently at bulge pressures around 200kPa. The ostensible final deflections were inconsistent, scattered in the range between 20-25mm.

True equibiaxial tensile stress for the bulge tests was evaluated for a spherical membrane inflation in terms of the applied load pressure p

$$\sigma_{\theta,\phi}^{exp} = \frac{p\rho}{2t_0\lambda_{\theta,\phi}^2} \tag{6.12}$$

where $t_0\lambda_{\theta,\phi}^2$ is the reduced instantaneous membrane thickness for an incompressible isotropic material. Bulge curvature ρ and circumferential stretch $\lambda_{\theta,\phi}$ are geometric terms that were evaluated with respect to the apex deflection.

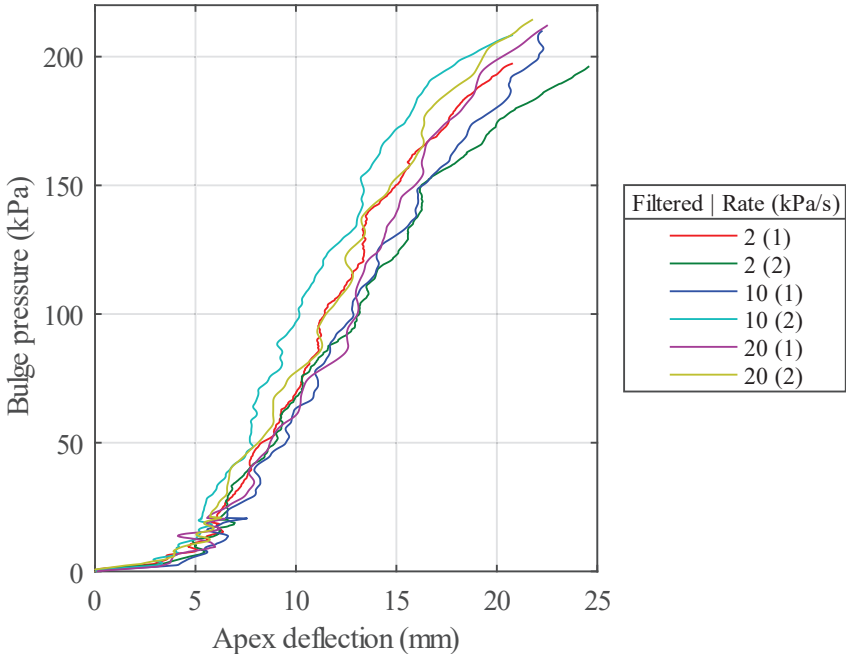

Figure 6-16: Pressure-deflection response for the neoprene bulge tests (deflection filtered)

The stress-stretch response results for the biaxial bulge tests are shown in Figure 6-17. The failure stresses and strains fell within a 2.8 – 3.4 MPa and 40 - 55% range respectively. Visually the results did not group well together at low or high strains. The overall quality and smoothness of the biaxial mechanical response results was poor as a result of the noisy deflection data. Mooney-Rivlin coefficients were fitted for each to test response and are presented in Appendix G.

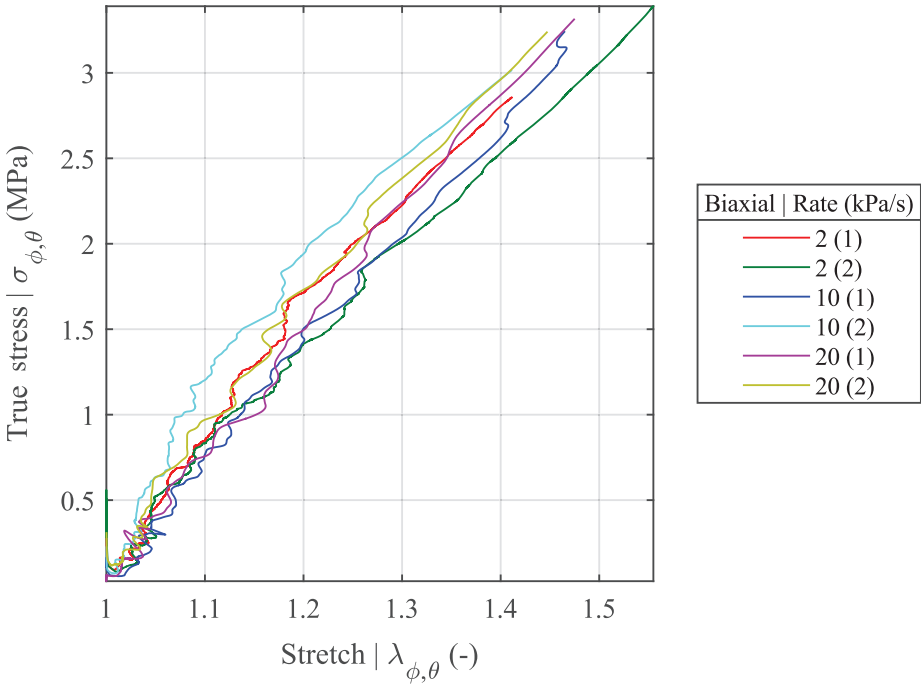

Figure 6-17: Experimental stress-stretch response for mechanical bulge tests

6.4.3.3 Discussion

Comparison of the uniaxial and equibiaxial mechanical responses presented in Figure 6-14 and Figure 6-17 respectively indicates a clear increase in the response stiffness, and a reduction in maximum stress in biaxial loading. This was anticipated from the literature and indicated adequacy of the bulge testing platform's potential for biaxial mechanical testing as a necessary addition to uniaxial tensile testing.

Table 6-5: Summary of the fitted Mooney-Rivlin model parameters for the mechanical tests

Test Type	**C_1 (kPa)**		**C_2 (kPa)**	
	avg ± std dev	⌈*range*⌉ ⌊*range*⌋	avg ± std dev	⌈*range*⌉ ⌊*range*⌋
Uniaxial	212.7 ± 7.78	219.3 200.2	413.7 ± 25.2	436.5 370.6
Biaxial	869.6 ± 290.2	1410.2 717.0	-22.7 ± 131.0	-281.3 109.1

Uniaxial and equibiaxial Mooney-Rivlin model coefficient parameters that are presented in Appendix G are summarised in Table 6-5. The small variability in the uniaxial data fits

indicated fair repeatability for the established uniaxial mechanical testing platform. The high variability in the biaxial results indicate that the significant presence of noise in the signals introduced by the laser displacement sensor ultimately produced results with insufficient accuracy.

6.5 Summary

The pressurisation rate compliance of the bulge testing apparatus' feedback control system was tested and identified between 2kPa/s and 20kPa/s. The initial open-loop plant response time was varied within the 0.2 – 1.2s design range. Optimal control system performance was achieved for a combination of high pressurisation rate and slow plant response speed.

Equibiaxial mechanical tensile material tests were performed with neoprene rubber sheet samples using the bulge testing platform. Vertical apex displacement for the bulge tests was measured using a 1D laser displacement sensor which produced noisy deformation signals. The biaxial mechanical response results were compared with results collected using standard uniaxial tensile testing procedures. The uniaxial tensile tests produced results with adequate repeatability. The bulge tests produced satisfactory pressure time histories but suffered poor accuracy and repeatability due to the use of a laser displacement sensor which was used in the absence of a more appropriate 3D DIC measurement system.

Chapter 7

Conclusion

A prototype bulge testing device and operating platform was designed, created, developed, and modified to provide a stable development platform for future intended skin tissue testing applications. In summary, the specifications for the device are presented in Table 7-1 for the given prototype configuration (outputs indicate

A mechanical, pneumatically driven, free dual-piston piston-cylinder apparatus was configured in a pressure reducing configuration to reduce present EPR actuator resolution effects which were present due to the use of a low cost discretely outputting instrument.

Constant bulge test pressurisation rate control was implemented using an embedded software based closed-loop digital PI controller. The design of the controller was based on a first order transfer function model of the pressure vessel system which required *a priori* knowledge of pneumatic resistance and capacitance parameters. It was not feasible to define these parameters for the given system, due to the variability in stiffness of the anticipated specimens. Custom feedback controller design was implemented in the embedded software controller. Manual specification of feedback controller gain and zero-locus design parameters were based on an initial first order response time measurement of the material sample before each test.

Table 7-1: Summary of resources and actions for physical platform components

Resource	**Description**	**Input**	**Output/Action**
Pneumatics:			
Supply:	Regulated	10 – 16bar	10bar
Vacuum:	Venturi	3bar	vacuum
Piston-cylinder:			
Lower cylinder:	∅ small (75mm)	0 – 10bar	piston
		vacuum	return piston
Upper cylinder:	∅ large (120mm)	piston	0 – 3.9bar
Actuation control:			
Feedback:	DAC	0 – 4095bit	0 – 2.95V
Control signal:	Level shift	0 – 2.95V	0 – 10V
Output signal:	EP regulator	$24v_s$	-
		0 – 10V	0.5 – 10bar
Pressure:			
Measurement:	Transducer	$\pm 24v_s$	-
		0 – 10bar	-
Sensing:	Conversion	4 – 20mA	0 – 5V [-1.25V]
Feedback input:	ADC	0 – 5V	0 – 65535bit
State monitoring:			
Threshold:	Software	pressure	abort if >⌈historical⌉?
Rupture:	Software	pressure	abort if <0.5*⌈historical⌉?
Data interfaces			
Computer:	User I/face	test data config	test data
Test Data:	Pressure history	pressure data output	filing system storage

The pressurisation rate control system was successfully tested to track rates between 2 – 20 kPa/s, to a maximum output pressure of about 200 kPa. On the lower scale of the tested rates the output pressure signal quality deteriorated due to effects from the EPR resolution. Controller performance was improved by manually adjusting a needle valve to slow gas flow into the apparatus.

In this report bulge apex deflection was measured with an *ad hoc* 1D laser displacement sensor which produced inferior mechanical response results from the collected bulge pressure-time output. Deformation measurement for the tested samples requires 3D DIC techniques (or similar) to accurately track deformation. Post sample rupture waterproofing protection of camera equipment which would be required if a hydraulic bulge fluid is used was not completed due to time constraints.

Numerous manual and automated safety features were implemented to provision predictable termination criteria and behaviours for the system. The implementation of an efficient rupture detection routine was highly successful in automatically arresting supply and exhausting pressurised components.

The platform that was developed in this report was successful in providing an appropriate infrastructure and framework for general bulge testing applications of elastomeric materials. The mechanical apparatus proved to be an effective pressurisation mechanism but requires some revision in a few key areas. The user interface, control system implementation and integration, data collection, and data storage mechanisms were highly effective and straightforward to use, making the backend of the platform largely reusable.

7.1 Recommendations

The design of the mechanical bulge testing apparatus can be improved in few key areas to improve its performability:

- The sample clamping mechanism should be redesigned to be more biomaterial friendly (omit the need for bonding of the sample to a rigid backing) and adopt a less elaborate sealing mechanism that doesn't cause precursory sample deformation.
- The revised clamping mechanism should be tested at higher pressures (>4bar) as it is most vulnerable to leaking here
- Containment of hydraulic bulge fluid (if used), post rupture, should be designed to localise fluid loss to protect the user and sensitive electronic components.
- If gas compression is preferred for bulge pressurisation, it is recommended that the volumetric capacity of the bulge fluid chamber is increased in some way
- Components which were manufactured from mild steel (such as cylinder tubes **and** adapters) should be replaced with non-corrodible equivalents if exposed to hydraulic media. Corrosion occurred in precision components when not strictly maintained.

The design of the rate control feedback system can be improved in few key areas to improve its efficacy:

- An alternative feedback control design strategy should be considered if possible as the current method of identifying system parameters from an initial state is laborious and the parameters do not appear to remain necessarily static
- The current strategy assumed that pressure would invariably rise with increasing strain; this is not always necessarily true for elastomers. Safeguarding should be implemented in the case that pressure drops (gradually) with strain.

Improvements can be made for the instrumentation and controls:

- If fine control of the pressurisation is required, a servo-piloted pressure regulator should be used instead of the solenoid-controlled EPR solution that was used
- Printed circuit boards (PCBs) should be fabricated for the electronic circuitry schematics which are presented in Appendix C.

The testing platform is highly effective in performing rate-controlled pressurisation tests. Improvements of the testing platform from a mechanical material testing aspect can be improved by implementing:

- Measurement of planar and out of plane sample deformation should be performed using 3D DIC and digital imaging techniques to obtain realistic deformation data to get representative stress and strain evaluations.

References

[1] G. W. Wood, M. B. Panzer, C. R. Bass, and B. S. Myers, "Viscoelastic Properties of Hybrid III Head Skin," *SAE Int. J. Mater. Manuf.*, vol. 3, pp. 186–193, 2010.

[2] ABAQUS, "Hyperelastic behavior of rubberlike materials." [Online]. Available: https://abaqus-docs.mit.edu/2017/English/SIMACAEMATRefMap/simamat-c-hyperelastic.htm. [Accessed: 25-Nov-2019].

[3] K. Langer, "On the anatomy and physiology of the skin: I. The cleavability of the cutis," *Br. J. Plast. Surg.*, vol. 31, no. 1, pp. 3–8, Jan. 1978.

[4] J. A. McGrath, R. A. J. Eady, and F. M. Pope, "Anatomy and Organization of Human Skin," in *Rook's Textbook of Dermatology*, John Wiley & Sons, Ltd, 2008, pp. 45–128.

[5] A. Laurent *et al.*, "Echographic measurement of skin thickness in adults by high frequency ultrasound to assess the appropriate microneedle length for intradermal delivery of vaccines," *Vaccine*, vol. 25, no. 34, pp. 6423–6430, 2007.

[6] H. Oxlund, J. Manschot, and A. Viidik, "The role of elastin in the mechanical properties of skin," *J. Biomech.*, vol. 21, no. 3, pp. 213–218, 1988.

[7] I. A. Brown, "Scanning electron microscopy of human dermal fibrous tissue.," *J. Anat.*, vol. 113, no. Pt 2, pp. 159–168, Nov. 1972.

[8] M. D. Ridge and V. Wright, "The directional effects of skin, a bio-engineering study of skin with particular reference to langer's lines," *J. Invest. Dermatol.*, vol. 46, no. 4, pp. 341–346, 1966.

[9] C. H. Daly, "Biomechanical properties of dermis," *J. Invest. Dermatol.*, vol. 79, no. Suppl. 1, pp. 17–20, 1982.

[10] M. Nordin and V. H. Frankel, *Basic Biomechanics of the Musculoskeletal System*. Philadelphia: Lippincott Williams & Wilkins, 2001.

[11] B. Zhou, F. Xu, C. Q. Chen, and T. J. Lu, "Strain rate sensitivity of skin tissue under thermomechanical loading," *Philos. Trans. R. Soc. A Math. Phys. Eng. Sci.*, vol. 368, no. 1912, pp. 679–690, 2010.

[12] Z. Liu and K. Yeung, "The Preconditioning and Stress Relaxation of Skin Tissue," *J. Biomed. Pharm. Eng.*, vol. 1, no. 1, pp. 22–28, 2008.

[13] F. H. Silver and J. Freeman, "Viscoelastic properties if human skin and processed dermis."

[14] C.-H. Lee, K. L. Billiar, W. Zhang, M. S. Sacks, and Y. Feng, "A Generalized Method for the Analysis of Planar Biaxial Mechanical Data Using Tethered Testing Configurations," *J. Biomech. Eng.*, vol. 137, no. 6, p. 064501, 2014.

[15] O. A. Shergold, N. A. Fleck, and D. Radford, "The uniaxial stress versus strain response of pig skin and silicone rubber at low and high strain rates," *Int. J. Impact Eng.*, vol. 32, no. 9, pp. 1384–1402, 2006.

[16] R. Reihsner, B. Balogh, and E. J. Menzel, "Two-dimensional elastic properties of human skin in terms of an incremental model at the in vivo configuration," *Med. Eng. Phys.*, vol. 17, no. 4, pp. 304–313, 1995.

[17] A. N. Annaidh, M. Ottenio, K. Bruyère, M. Destrade, and M. D. Gilchrist, "Mechanical properties of excised human skin," *IFMBE Proc.*, vol. 31 IFMBE, pp. 1000–1003, 2010.

[18] C. A. Edwards and R. Marks, "Evaluation of biomechanical properties of human skin.," *Clin. Dermatol.*, vol. 13 4, pp. 375–380, 1995.

[19] M. Ottenio, D. Tran, A. N. Annaidh, M. D. Gilchrist, and K. Bruyère, "Strain rate and anisotropy effects on the tensile failure characteristics of human skin," *J. Mech. Behav. Biomed. Mater.*, vol. 41, pp. 241–250, 2015.

[20] F. H. Silver, J. W. Freeman, and D. DeVore, "Viscoelastic properties of human skin and processed dermis," *Ski. Res. Technol.*, vol. 7, no. 1, pp. 18–23, 2001.

[21] J. Lim, J. Hong, W. W. Chen, and T. Weerasooriya, "Mechanical response of pig skin under dynamic tensile loading," *Int. J. Impact Eng.*, vol. 38, no. 2–3, pp. 130–135, 2011.

[22] R. J. Lapeer, P. D. Gasson, and V. Karri, "Simulating plastic surgery: From human skin tensile tests, through hyperelastic finite element models to real-time haptics," *Prog. Biophys. Mol. Biol.*, vol. 103, no. 2–3, pp. 208–216, 2010.

[23] A. Delalleau, G. Josse, J.-M. Lagarde, H. Zahouani, and J.-M. Bergheau, "A nonlinear elastic behavior to identify the mechanical parameters of human skin in vivo.," *Skin Res. Technol.*, vol. 14, no. 2, pp. 152–164, May 2008.

[24] M. S. Sacks, "Biaxial Mechanical Evaluation of Planar Biological Materials," *J. ofElasticity*, vol. 61, pp. 199–246, 2000.

[25] G. E. Leclerc, Q. Dermigny, M. Rachik, and M.-C. Ho Ba Tho, "Biaxial mechanical response of graft material derived from human skin," *Comput. Methods Biomech. Biomed. Engin.*, vol. 17, no. sup1, pp. 26–27, 2014.

[26] G. T. Mase and G. E. Mase, "Nonlinear Elasticity," in *Continuum Mechanics for Engineers*, 2nd ed., Boca Raton: CRC Press LLC, 1999, pp. 310–337.

[27] M. Mooney, "A Theory of Large Plasic Deformation," *J. Appl. Phys.*, vol. 11, pp. 582–592, 1940.

[28] R. S. Rivlin, "Large Elastic Deformations of Isotropic materials IV," no. October, 1948.

[29] R. W. Ogden and R. Hill, "Large deformation isotropic elasticity - on the correlation of theory and experiment for incompressible rubberlike solids," *Proc. R. Soc. London.*

A. Math. Phys. Sci., vol. 326, no. 1567, pp. 565–584, 1972.

[30] G. A. Holzapfel, T. C. Gasser, and R. W. Ogden, "A New Constitutive Framework for Arterial Wall Mechanics and a Comparative Study of Material Models," *J. Elast. Phys. Sci. solids*, vol. 61, no. 1, pp. 1–48, Jul. 2000.

[31] L. R. G. Treloar, "Stress-Strain Data for Vulcanised Rubber under Various Types of Deformation," *Trans. Faraday Soc.*, vol. 40, pp. 59–70, 1944.

[32] R. S. Rivlin, D. W. Saunders, and E. N. D. C. Andrade, "Large elastic deformations of isotropic materials VII. Experiments on the deformation of rubber," *Philos. Trans. R. Soc. London. Ser. A, Math. Phys. Sci.*, vol. 243, no. 865, pp. 251–288, 1951.

[33] R. W. Ogden, "Large Deformation Isotropic Elasticity—On the Correlation of Theory and Experiment for Incompressible Rubberlike Solids," *Rubber Chem. Technol.*, vol. 46, no. 2, pp. 398–416, 2011.

[34] E. M. Arruda and M. C. Boyce, "A three-dimensional constitutive model for the large stretch behavior of rubber elastic materials," *J. Mech. Phys. Solids*, vol. 41, no. 2, pp. 389–412, 1993.

[35] M. Johlitz and S. Diebels, "Characterisation of a polymer using biaxial tension tests. Part I: Hyperelasticity," *Arch. Appl. Mech.*, vol. 81, no. 10, pp. 1333–1349, 2011.

[36] H. Seibert, T. Scheffer, and S. Diebels, "Biaxial testing of elastomers - Experimental setup, measurement and experimental optimisation of specimen's shape," *Tech. Mech.*, vol. 34, no. 2, pp. 72–89, 2014.

[37] M. Sasso, G. Chiappini, M. Rossi, L. Cortese, and E. Mancini, "Visco-Hyper-Pseudo-Elastic Characterization of a Fluoro-Silicone Rubber," *Exp. Mech.*, vol. 54, no. 3, pp. 315–328, 2014.

[38] G. S. Kassab, S. Chambers, X. Zhao, Z. C. Berwick, J. F. Krieger, and H. Chen, "Novel Design of Cruciform Specimens for Planar Biaxial Testing of Soft Materials," *Exp. Mech.*, vol. 54, no. 3, pp. 343–356, 2013.

[39] J. McIntyre, T. Alsuth, Y. F. Zhou, M. Johnson, and S. Jerrams, "Realistic fatigue life prediction for magnetorehological elastomers," in *Constitutive Models for Rubber VIII*, London: Taylor & Francis Group, 2013, pp. 677–682.

[40] Z. Marciniak, J. Duncan, and S. Hu, *Mechanics of Sheet Metal Forming*. Oxford: Butterworth-Heinemann, 2002.

[41] C. T. Nguyen, T. Vu-Khanh, and J. Lara, "Puncture characterization of rubber membranes," *Theor. Appl. Fract. Mech.*, vol. 42, no. 1, pp. 25–33, 2004.

[42] M. Sasso, G. Palmieri, G. Chiappini, and D. Amodio, "Characterization of hyperelastic rubber-like materials by biaxial and uniaxial stretching tests based on optical methods," *Polym. Test.*, vol. 27, no. 8, pp. 995–1004, 2008.

[43] Y. Lanir and Y. C. Fung, "Two-dimensional mechanical properties of rabbit skin—II. Experimental results," *J. Biomech.*, vol. 7, no. 2, pp. 171–182, 1974.

[44] S. D. Waldman and J. Michael Lee, "Boundary conditions during biaxial testing of

planar connective tissues. Part 1: dynamic behavior.," *J. Mater. Sci. Mater. Med.*, vol. 13, no. 10, pp. 933–938, Oct. 2002.

[45] A. N. Annaidh *et al.*, *Automated estimation of collagen fibre dispersion in the dermis and its contribution to the anisotropic behaviour of skin*, vol. 40, no. 8. 2012.

[46] A. Karimi, S. M. Rahmati, and M. Navidbakhsh, "Mechanical characterization of the rat and mice skin tissues using histostructural and uniaxial data," *Bioengineered*, vol. 6, no. 3, pp. 153–160, 2015.

[47] P. Zioupos, J. C. Barbenel, and J. Fisher, "Mechanical and optical anisotropy of bovine pericardium," *Med. Biol. Eng. Comput.*, vol. 30, no. 1, pp. 76–82, 1992.

[48] T. K. Tonge, L. S. Atlan, L. M. Voo, and T. D. Nguyen, "Full-field bulge test for planar anisotropic tissues: Part I-Experimental methods applied to human skin tissue," *Acta Biomater.*, vol. 9, no. 4, pp. 5913–5925, 2013.

[49] W. Rothkopf, T. K. Tonge, S. Alexander, T. D. Nguyen, B. J. Murienne, and B. Coudrillier, "Minimal Preconditioning Effects Observed for Inflation Tests of Planar Tissues," *J. Biomech. Eng.*, vol. 135, no. 11, p. 114502, 2013.

[50] K. Ogata, *Modern Control Engineering*, Fifth. New Jersey: Prentice Hall, 2010.

[51] M. S. Fadali and A. Visioli, *Digital Control Engineering*, Second. Oxford: Academic Press, 2013.

[52] S. A. Agustin and K. D. Jadhav, "Structural analysis of elliptical pressure vessels with circular cross section," *Int. J. Chem. Sci.*, vol. 14, no. 3, pp. 1633–1640, 2016.

[53] D. Wright, "Thin Shells of Revolution - Heads," 2005. [Online]. Available: http://www-mdp.eng.cam.ac.uk/web/library/enginfo/textbooks_dvd_only/DAN/pressVessels/shells/shells.html. [Accessed: 10-Jan-2016].

[54] W. M. Lai, E. Krempl, and D. Rubin, "Introduction to Continuum Mechanics," 3rd ed., Butterworth-Heinemann, 1993, pp. 225–230.

[55] Camozzi, "Series LR*D2 digital proportional servo valves." Datasheet

[56] Camozzi, "Series MX-PRO electronic proportional regulator," *Datasheet*.

[57] SMC, "Compact Direct Operated 2/3 Port Solenoid Valve for Water and Air Series VDW." SMC Corporation, Tokyo, pp. 1–20.

[58] SMC Corporation, "Pilot Operated 2 Port Solenoid Valve Series VX21/22/23." SMC Corporation, pp. 1–27, 2011.

[59] Piab Group, "piINLINE® MICRO." [Online]. Available: https://www.piab.com/en-US/products/vacuum-pumps/decentralized-vacuum-ejectors/piinline-micro-/. [Accessed: 29-Jul-2019].

[60] K. Ogata, *Modern Control Engineering*, Fifth. New Jersey: Prentice Hall, 2010.

[61] M. S. Fadali and A. Visioli, *Digital Control Engineering*, Second. Oxford: Academic Press, 2013.

[62] V. Hanta and A. Procházka, "Rational approximation of time delay," *Inst. Chem.*

Technol. Prague. Dep. Comput. Control Eng. Tech., vol. 5, no. 166, p. 28, 2009.

[63] B. A. Olshausen, "Aliasing," 2000. [Online]. Available: http://redwood.berkeley.edu/bruno/npb261/aliasing.pdf. [Accessed: 25-Feb-2019].

[64] STMicroelectronics, "STM32F4DISCOVERY." .

[65] Arduino, "Compare board specs," 2019. [Online]. Available: https://www.arduino.cc/en/products/compare. [Accessed: 01-Dec-2019].

[66] Prolific, "PL2303TA USB to Serial Bridge Controller." 2012.

[67] RS Components, "31ISB0010G01R000 | Gems Sensors ATEX Gauge for Fluid, Gas Pressure Sensor, 10bar Max Pressure Reading , 8 → 24 V dc, G1/4, IP67 | RS Components." [Online]. Available: https://za.rs-online.com/web/p/pressure-sensors/7970940/. [Accessed: 15-Jul-2019].

[68] Analog Devices, "AD7705/AD7706 3 V/5 V, 1 mW, 2-/3-Channel, 16-Bit Sigma-Delta ADCs Data Sheet (Rev. C)," pp. 1–44, 2006.

[69] Analog Devices, "Evaluation Board for The AD7705/06 3V/5V, 450uA, 2/3-Channel 16-Bit, Sigma Delta ADC." pp. 12–16, 1998.

[70] "ASTM D412-16, Standard Test Methods for Vulcanized Rubber and Thermoplastic Elastomers—Tension." ASTM International, West Conshohocken, PA, 2016.

[71] D. J. Dunn, "Stability of Pneumatic and Hydraulic Valves." [Online]. Available: http://www.freestudy.co.uk/control/t13.pdf. [Accessed: 03-Jan-2019].

[72] SMC Corporation, "Electro-Pneumatic Regulator / Electronic Vacuum Regulator," *ITV Ser. datasheet*.

[73] Burr-Brown, "RCV420: Precision 4mA to 20mA Current Loop Receiver." pp. 1–10, 1997.

[74] Gems Sensors And Controls, "31IS Series and 32IS Heavy Duty Series Intrinsically Safe Industrial Pressure Transmitters," *31ISB0010G01R000 datasheet*.

[75] ST Microelectronics, "World's smallest Time-of-Flight ranging and gesture detection," no. VL53L0X datasheet. p. May 2016 [Revised April 2018].

[76] Adafruit, "Arduino library for Adafruit VL53L0X." [Online]. Available: https://github.com/adafruit/Adafruit_VL53L0X. [Accessed: 31-Oct-2018].

[77] J. Cook and J. Freudenberg, "Embedded Software Architecture." pp. 1–14, 2007.

Appendix A

Mechanical Drawings

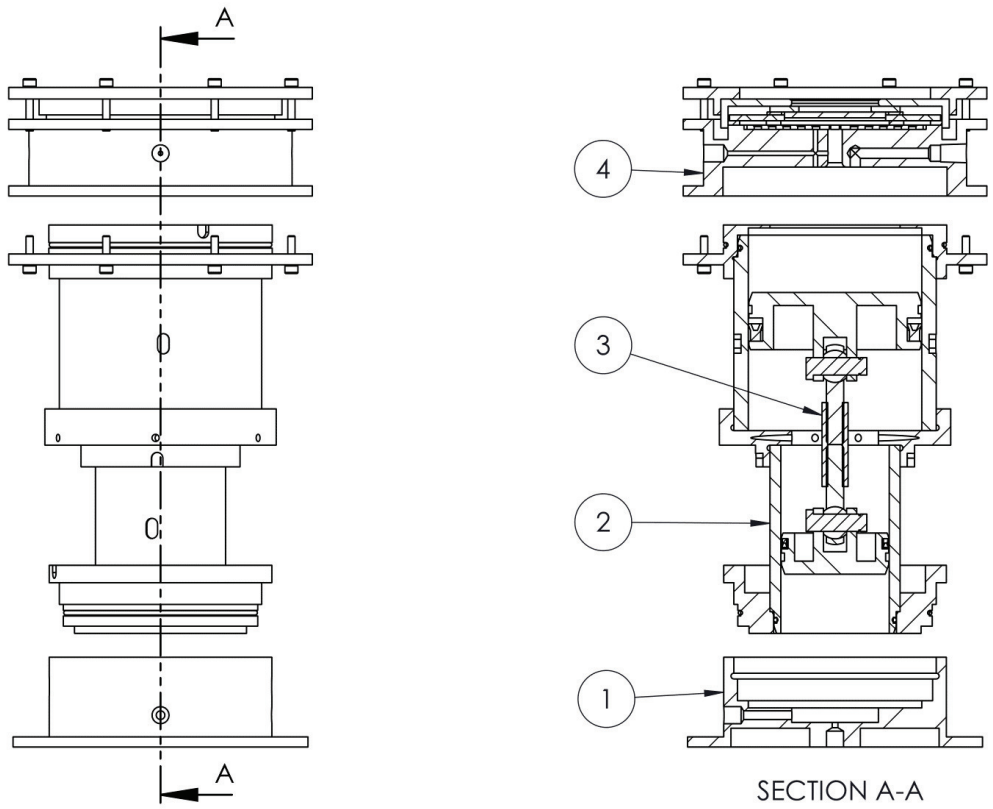

ITEM NO.	PART NUMBER	DESCRIPTION	QTY.	DWG.
1	Base_asm	PNEUMATIC SUPPLY BASE (ADAPT TO - M140X2 MAX COMPATIBLE)	1	P1
2	Piston_Cylinder_asm	SEALED, PISTON CYLINDERS	1	A1
3	Piston_Head_asm	DOUBLE ENDED FREE PISTON	1	A2
4	Manifold_asm	SAMPLE CLAMPING AND PRESSURISATION INTERFACE	1	A3

A4 Landscape	University of Cape Town Department of Mechanical Engineering			
	Title: Bulge_Tester_asm			
Assembly Drawing	Scale: 1:4	Date: 2019/08/08	Sheet1	of 1
	Drawn By: DUSTIN FISCHER		Drawing Number R1	

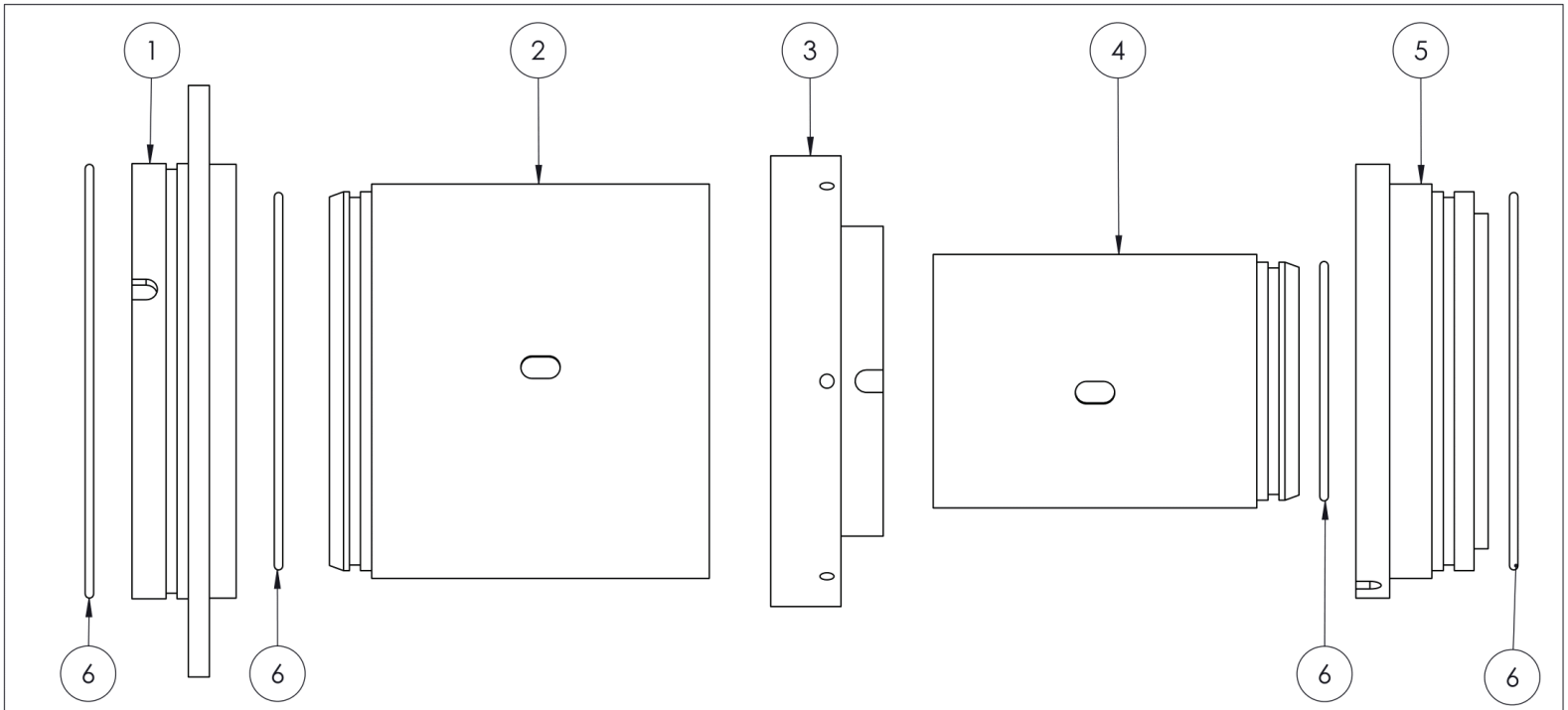

ITEM NO.	PART NUMBER	NOTES	QTY.	DWG.
1	Piston_Cyl_(M140x2)_Head_Adapter	TIGHTEN / ∅155 MM C-SPANNER	1	P2
2	Piston_Cyl_(M140x2)	TIGHTEN / ∅140 MM C-SPANNER	1	P3
3	Piston_Cyl_(M140x2)_(M90x2)_Adapter	TIGHTEN / ∅110 MM C-SPANNER	1	P4
4	Piston_Cyl_(M90x2)	TIGHTEN / ∅90 MM C-SPANNER	1	P5
5	Piston_Cyl_(M90x2)_Base_Adapter	TIGHTEN ∅154 MM C-SPANNER	1	P6
6	Radial O-ring Seal	ID 128mm - OD 134mm	4	-

A4 Landscape	University of Cape Town Department of Mechanical Engineering			
	Title: Piston_Cylinder_asm			
Assembly Drawing	Scale: 1:10	Date: 2019/08/08	Sheet1	of 1
	Drawn By: DUSTIN FISCHER		Drawing Number A1	

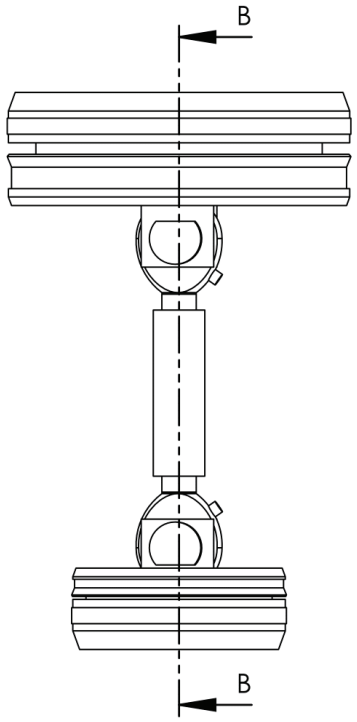

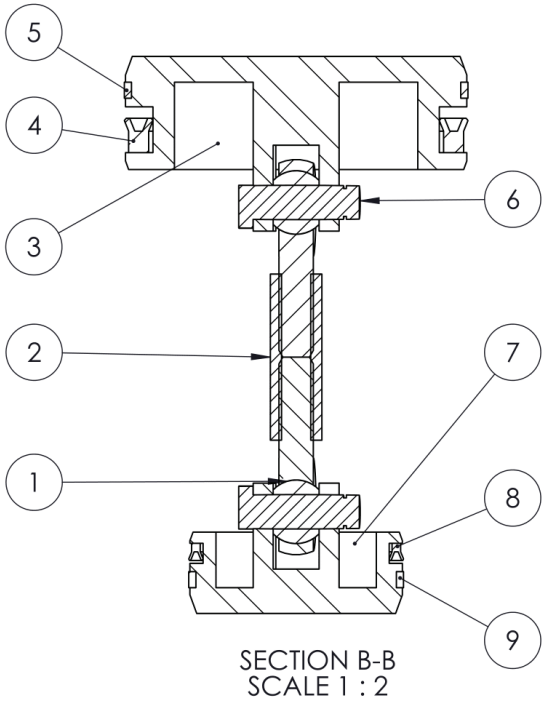

SECTION B-B
SCALE 1 : 2

ITEM NO.	PART NUMBER	NOTES	QTY.	DWG.
1	Rod_End_Bearing	M12x1.75; 1xCW & 1xCCW	2	-
2	Piston_Head_Conn_Rod	M12x1.75; 1xCW & 1xCCW	1	P7
3	Piston_Head_120OD	PISTON, LOW PRESSURE	1	P8
4	Piston_Head_120OD_Flare_Seal	RUBBER, U-SEAL	1	-
5	Piston_Head_120OD_Wear_Ring	PTFE, 5mm THICK	1	-
6	Piston_Head_Thru_Pin	EXTERNAL CIRCLIP ON END	2	P9
7	Piston_Head_75OD	PISTON, HIGH PRESSURE	1	P10
8	Piston_Head_75OD_Flare_Seal	RUBBER, U-SEAL	1	-
9	Piston_Head_75OD_Wear_Ring	PTFE, 5mm THICK	1	-

A4 Landscape	University of Cape Town Department of Mechanical Engineering			
	Title: Piston_Head_asm			
Assembly Drawing	Scale: 1:2.5	Date: 2019/08/08	Sheet1	of 1
	Drawn By: DUSTIN FISCHER		Drawing Number A2	

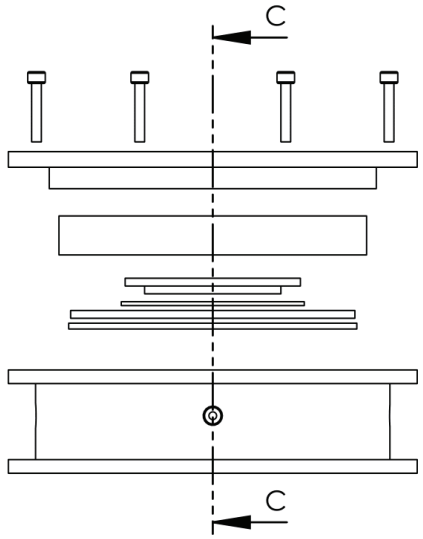

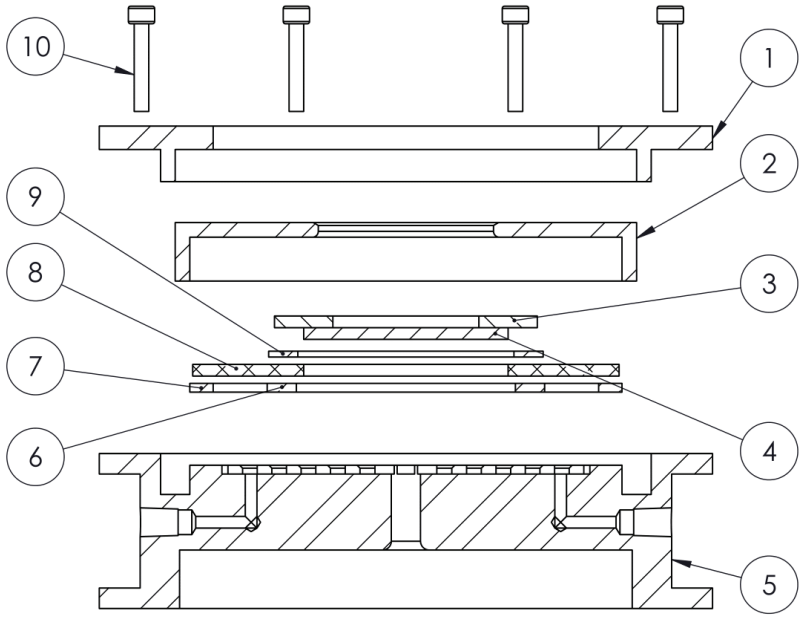

SECTION C-C
SCALE 1 : 2

ITEM NO.	PART NUMBER	NOTES	QTY.	DWG.
1	Head_Cap	LOAD TRANSFERRING CAP	1	P11
2	Head_sample_adapter_D60	ADAPTER: CUSTOM SAMPLE ∅ WINDOW	1	P12
3	misc_sample_wood_holder	LOAD TRANSFERRING SAMPLE BACKING	1	-
4	misc_sample_D70	MISC. MATERIAL SAMPLE	1	-
5	Head_Plate	ORIFICE / MANIFOLD / SUPPLY INTERFACE	1	P13
6	mis_perspex_bearing	PERSPEX BEARING RING: CUSTOM SAMPLE ∅	1	-
7	misc_gasket_outer	SILICONE RUBBER ANNULUS: 5MM THICK	1	-
8	misc_sample_interface	PERSPEX INTERFACE RING: CUSTOM SAMPLE ∅	1	-
9	misc_gasket_inner	SILICONE RUBBER ANNULUS: 3MM THICK	1	-
10	misc_M6_bolt	M6X1: LENGTH > 30MM	8	-

A4 Landscape	University of Cape Town Department of Mechanical Engineering			
	Title: Manifold_asm			
Assembly Drawing	Scale: 1:3	Date: 2019/08/08	Sheet1	of 1
	Drawn By: DUSTIN FISCHER		Drawing Number A3	

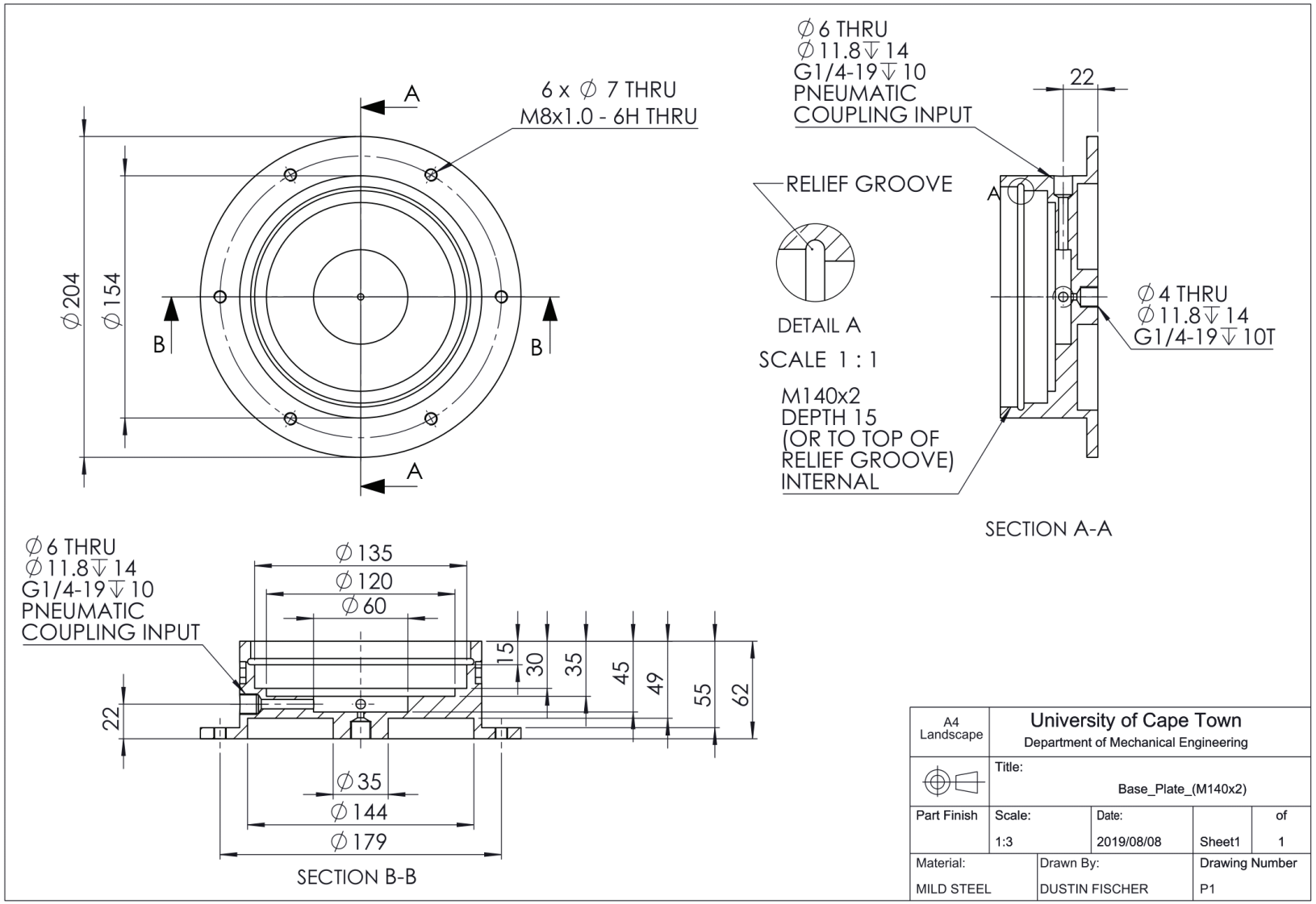

A4 Landscape	University of Cape Town Department of Mechanical Engineering			
	Title: Base_Plate_(M140x2)			
Part Finish	Scale: 1:3	Date: 2019/08/08	Sheet1	of 1
Material: MILD STEEL	Drawn By: DUSTIN FISCHER		Drawing Number P1	

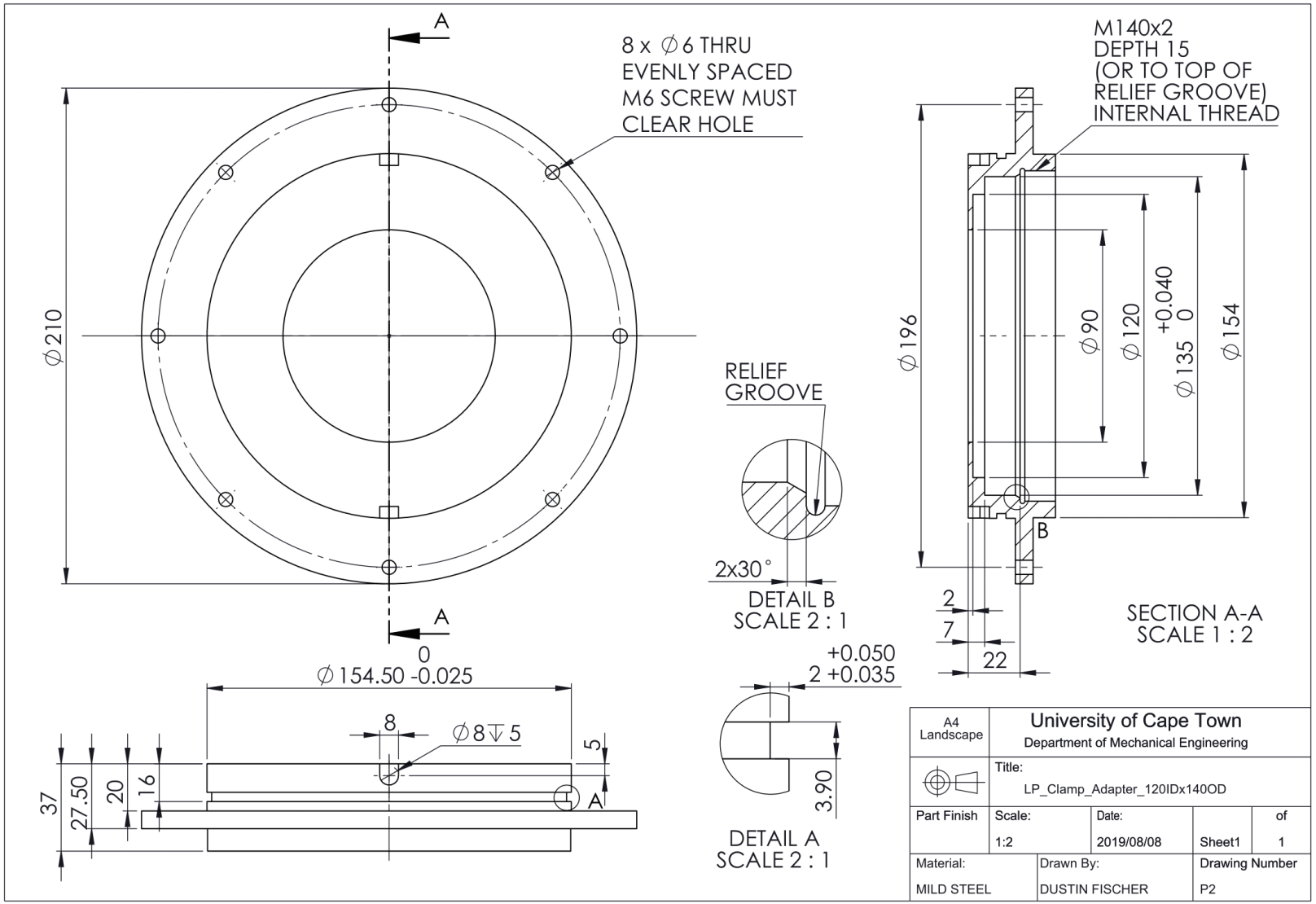
A
8 x ∅6 THRU
EVENLY SPACED
M6 SCREW MUST
CLEAR HOLE
∅210
A
0
∅154.50 -0.025
8
∅8↧5
5
37
27.50
20
16
A
RELIEF
GROOVE
2x30°
DETAIL B
SCALE 2 : 1
+0.050
2 +0.035
3.90
DETAIL A
SCALE 2 : 1
M140x2
DEPTH 15
(OR TO TOP OF
RELIEF GROOVE)
INTERNAL THREAD
∅196
∅90
∅120
+0.040
∅135 0
∅154
B
2
7
22
SECTION A-A
SCALE 1 : 2
A4
Landscape
University of Cape Town
Department of Mechanical Engineering
Title:
LP_Clamp_Adapter_120IDx140OD
Part Finish
Scale:
1:2
Date:
2019/08/08
Sheet1
of
1
Material:
MILD STEEL
Drawn By:
DUSTIN FISCHER
Drawing Number
P2

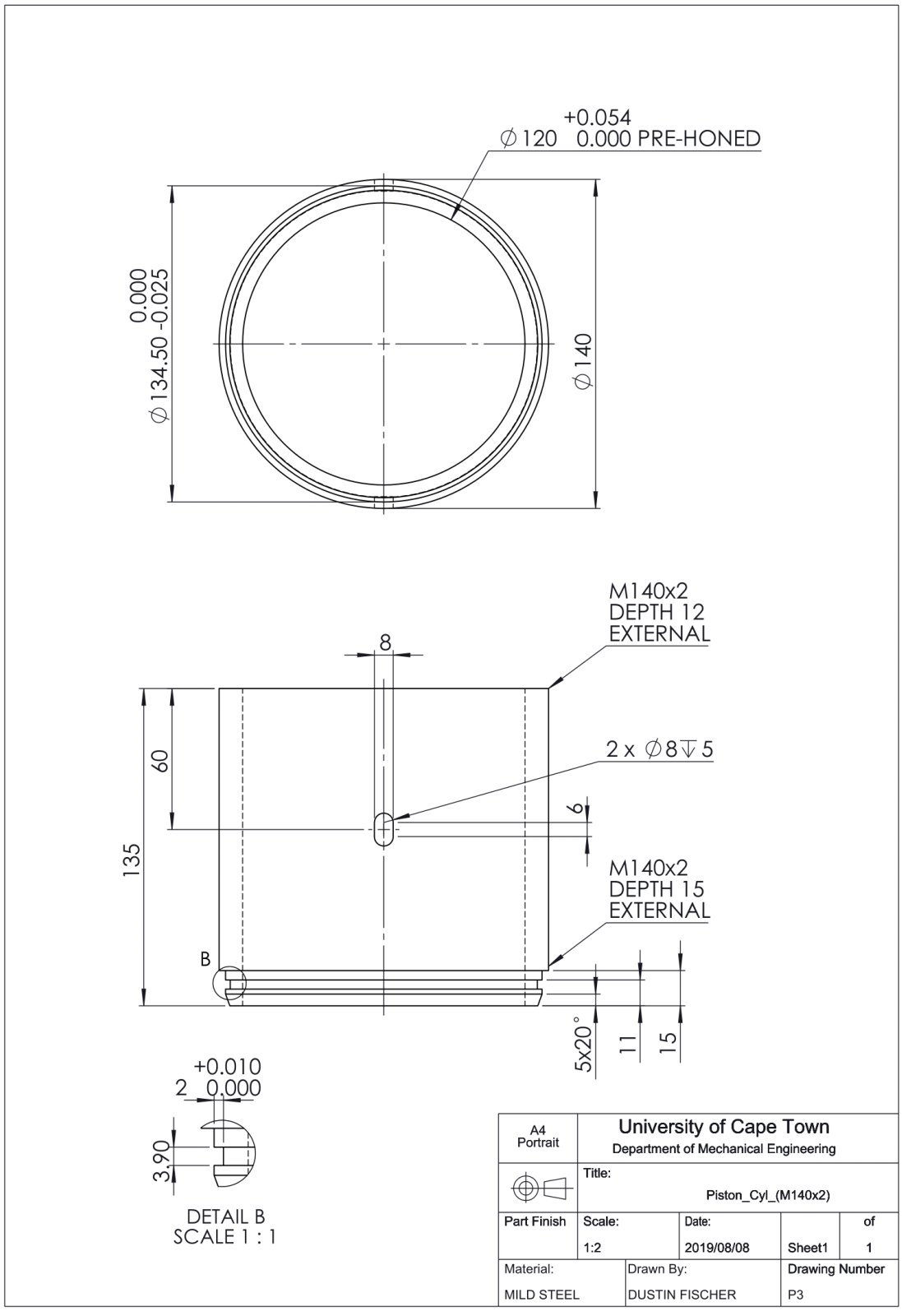
+0.054
∅120 0.000 PRE-HONED
0.000
∅134.50 -0.025
∅140
M140x2
DEPTH 12
EXTERNAL
8
2 x ∅8↧5
60
6
135
M140x2
DEPTH 15
EXTERNAL
B
5x20°
11
15
+0.010
2 0.000
3.90
DETAIL B
SCALE 1 : 1
A4
Portrait
University of Cape Town
Department of Mechanical Engineering
Title:
Piston_Cyl_(M140x2)
Part Finish
Scale:
1:2
Date:
2019/08/08
Sheet1
of
1
Material:
MILD STEEL
Drawn By:
DUSTIN FISCHER
Drawing Number
P3

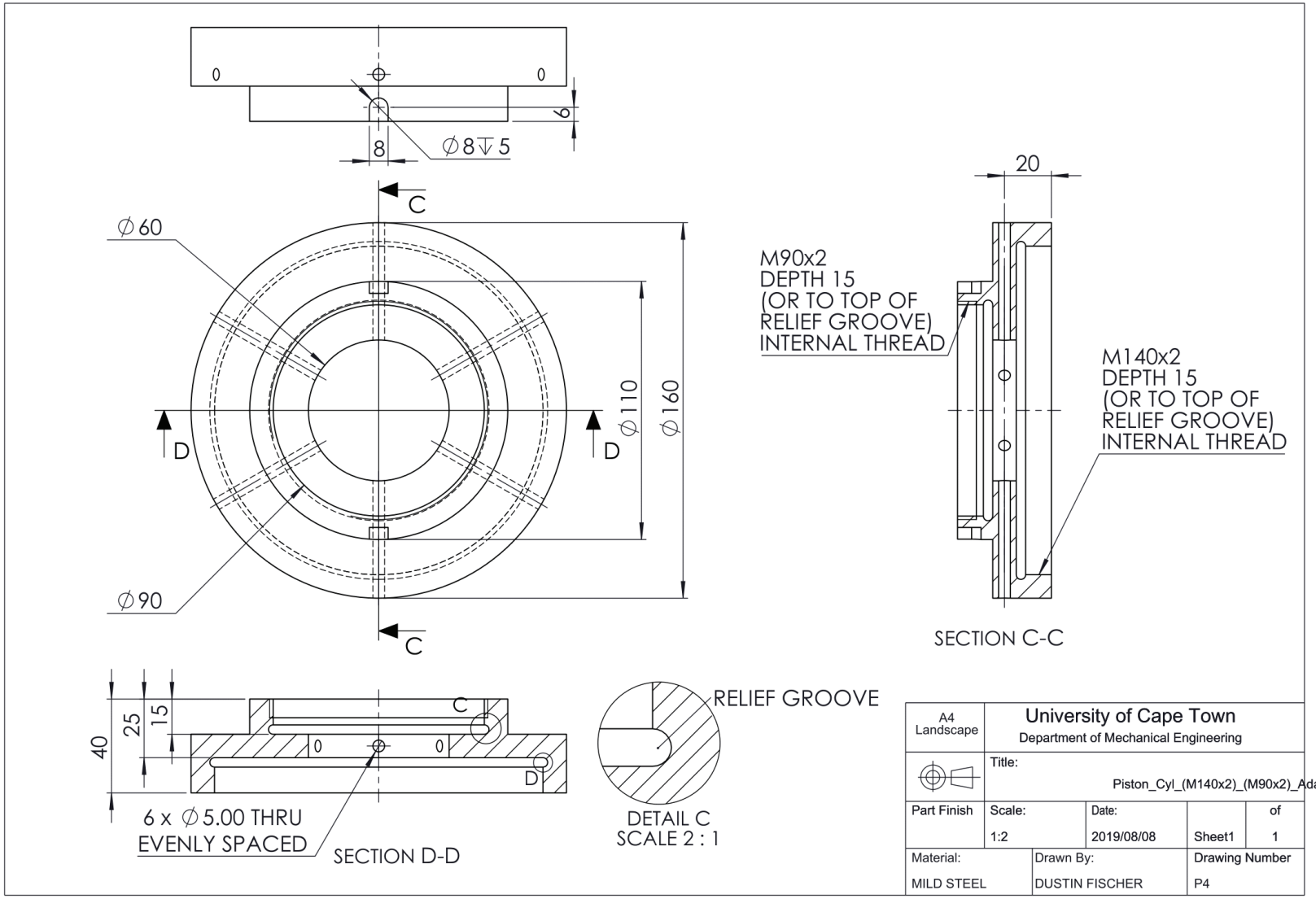
8
⌀8↧5
6
C
⌀60
⌀110
⌀160
D
D
⌀90
C
20
M90x2
DEPTH 15
(OR TO TOP OF
RELIEF GROOVE)
INTERNAL THREAD
M140x2
DEPTH 15
(OR TO TOP OF
RELIEF GROOVE)
INTERNAL THREAD
SECTION C-C
40
25
15
C
D
6 x ⌀5.00 THRU
EVENLY SPACED
SECTION D-D
RELIEF GROOVE
DETAIL C
SCALE 2 : 1
A4
Landscape
University of Cape Town
Department of Mechanical Engineering
Title:
Piston_Cyl_(M140x2)_(M90x2)_Adap
Part Finish
Scale:
1:2
Date:
2019/08/08
Sheet1
of
1
Material:
MILD STEEL
Drawn By:
DUSTIN FISCHER
Drawing Number
P4

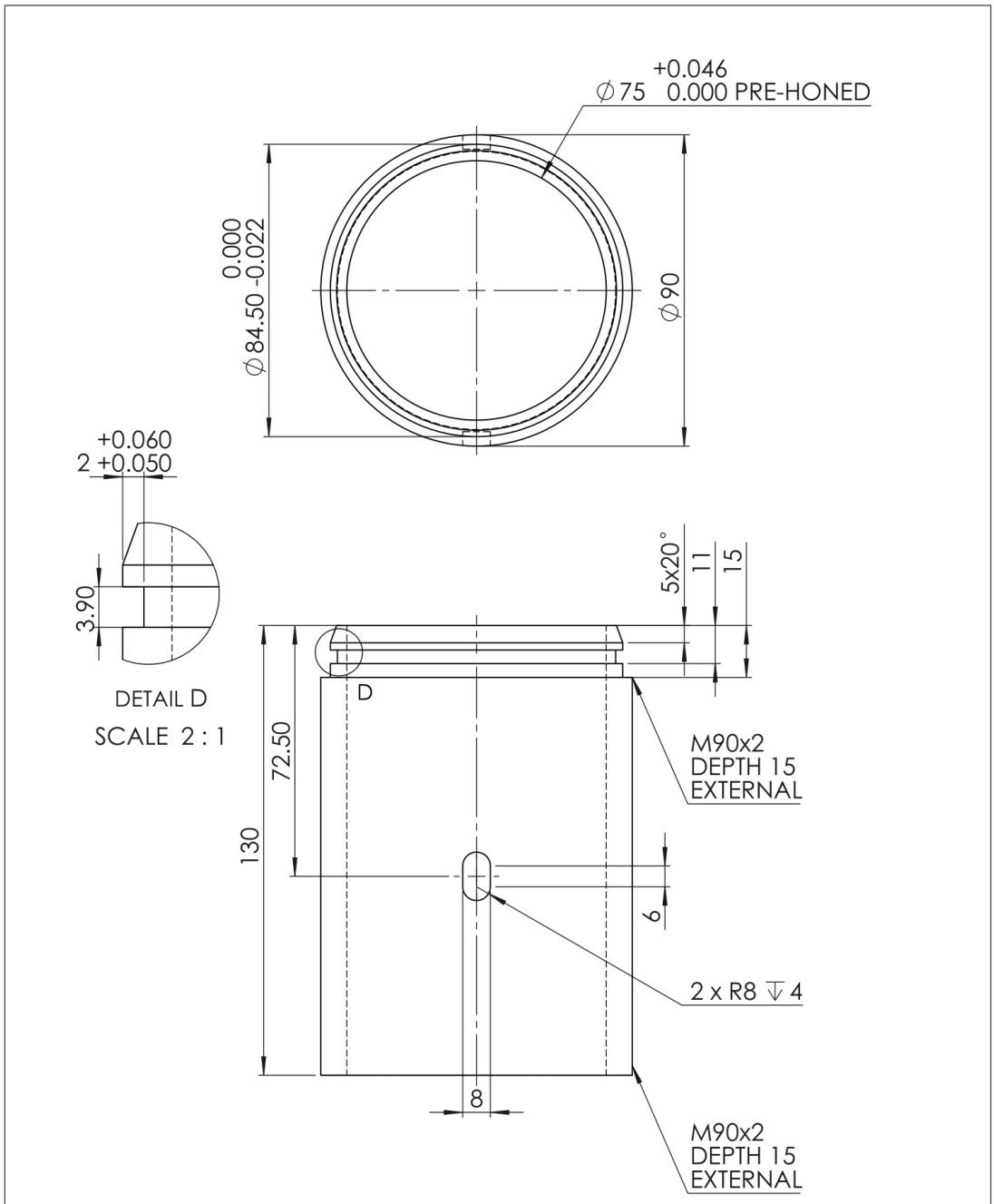

A4 Portrait	University of Cape Town Department of Mechanical Engineering			
	Title: Piston_Cyl_(M90x2)			
Part Finish	Scale: 1:1.5	Date: 2019/08/08	Sheet1	of 1
Material: MILD STEEL	Drawn By: DUSTIN FISCHER		Drawing Number P5	

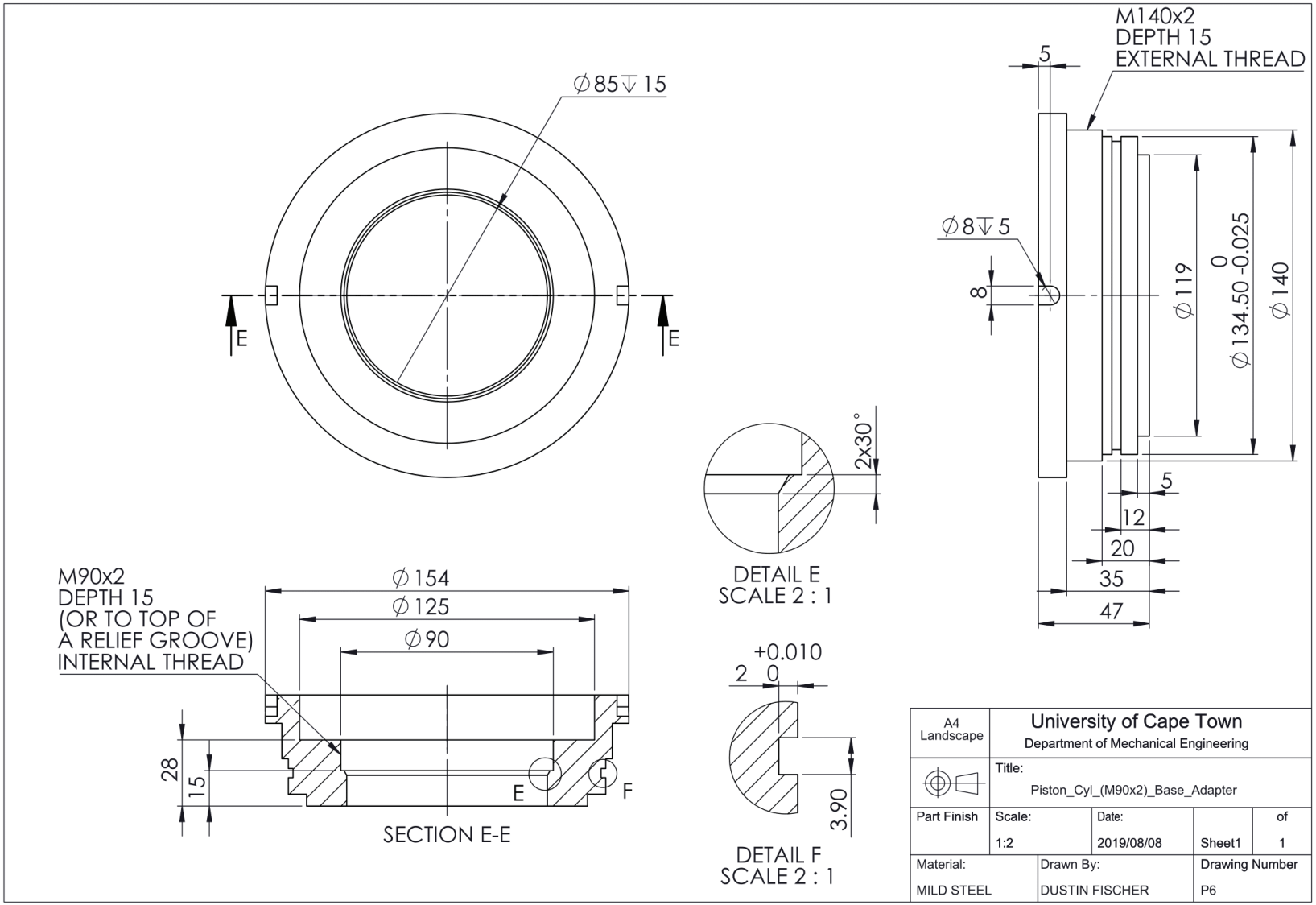
M140x2
DEPTH 15
EXTERNAL THREAD
5
∅85↧15
∅8↧5
8
∅119
∅134.50 0 -0.025
∅140
5
12
20
35
47
E
E
2x30°
DETAIL E
SCALE 2 : 1
M90x2
DEPTH 15
(OR TO TOP OF
A RELIEF GROOVE)
INTERNAL THREAD
∅154
∅125
∅90
28
15
E
F
SECTION E-E
+0.010
2 0
3.90
DETAIL F
SCALE 2 : 1
A4
Landscape
University of Cape Town
Department of Mechanical Engineering
Title:
Piston_Cyl_(M90x2)_Base_Adapter
Part Finish
Scale:
1:2
Date:
2019/08/08
Sheet1
of
1
Material:
MILD STEEL
Drawn By:
DUSTIN FISCHER
Drawing Number
P6

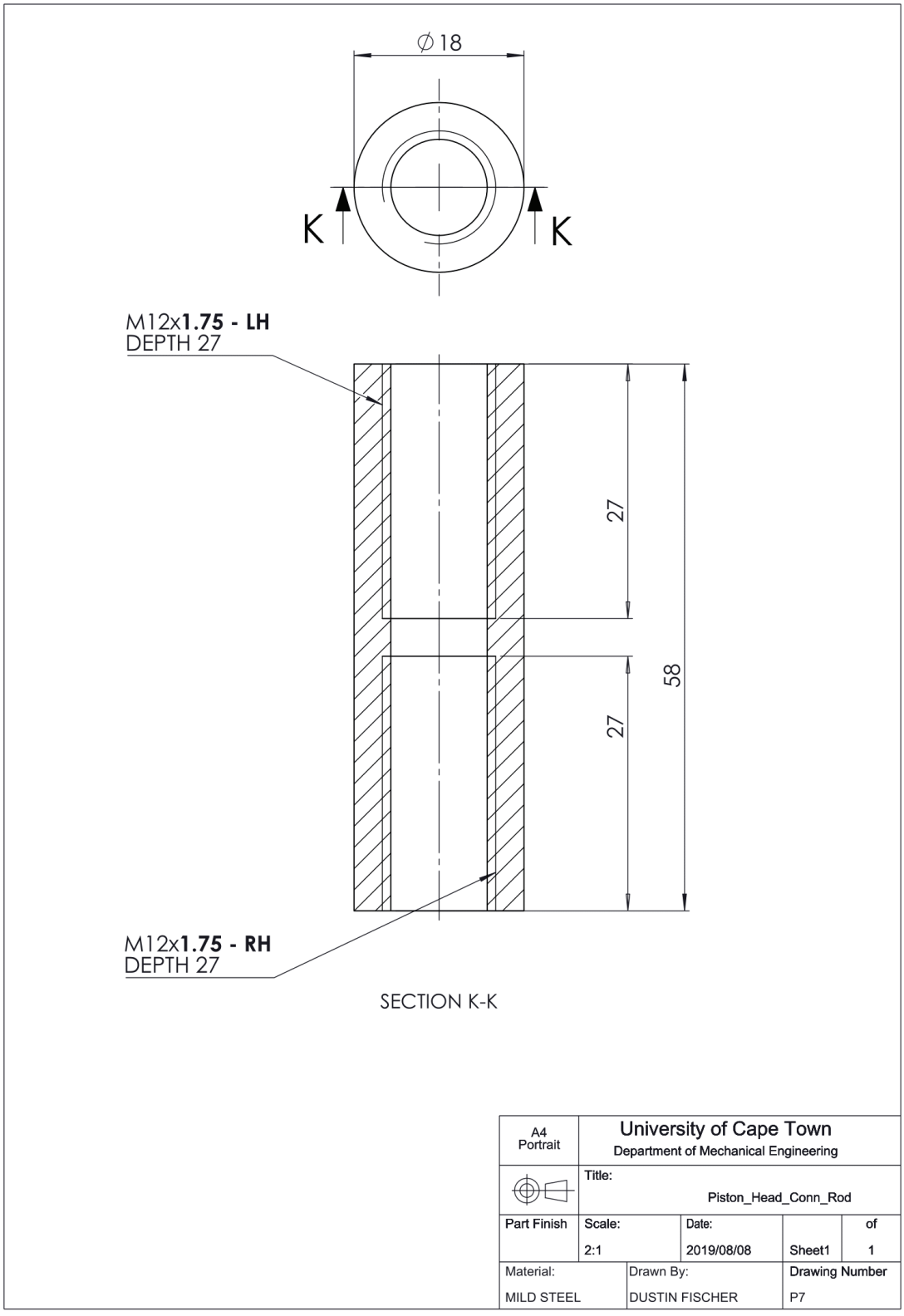

A4 Portrait	University of Cape Town Department of Mechanical Engineering			
	Title: Piston_Head_Conn_Rod			
Part Finish	Scale: 2:1	Date: 2019/08/08	Sheet1	of 1
Material: MILD STEEL	Drawn By: DUSTIN FISCHER		Drawing Number P7	

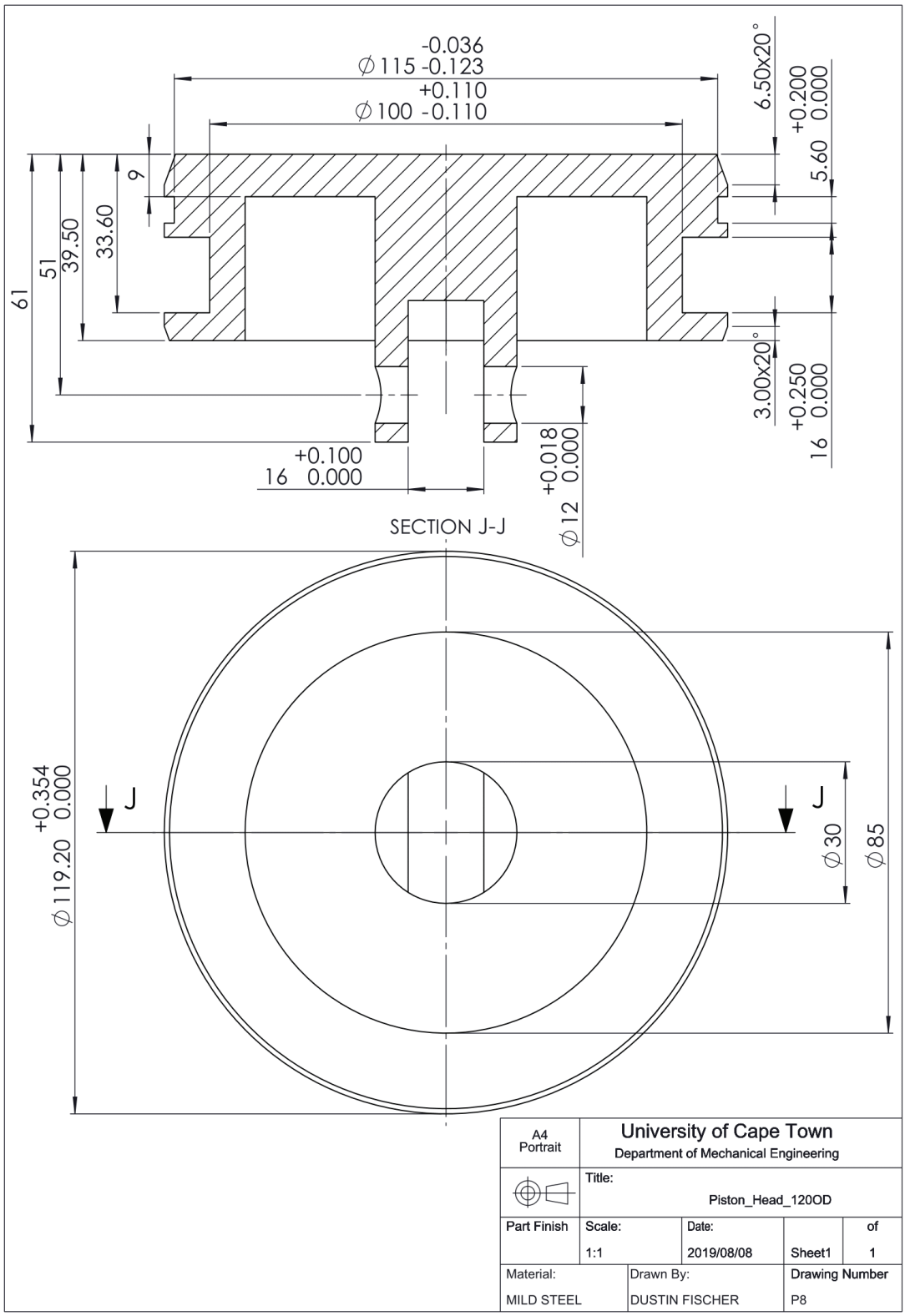
-0.036
∅115 -0.123
+0.110
∅100 -0.110
6.50x20°
+0.200
0.000
5.60
9
33.60
39.50
51
61
3.00x20°
+0.250
0.000
16
+0.100
16 0.000
+0.018
0.000
∅12
SECTION J-J
+0.354
0.000
∅119.20
J
J
∅30
∅85
A4
Portrait
University of Cape Town
Department of Mechanical Engineering
Title:
Piston_Head_120OD
Part Finish
Scale:
1:1
Date:
2019/08/08
Sheet1
of
1
Material:
MILD STEEL
Drawn By:
DUSTIN FISCHER
Drawing Number
P8

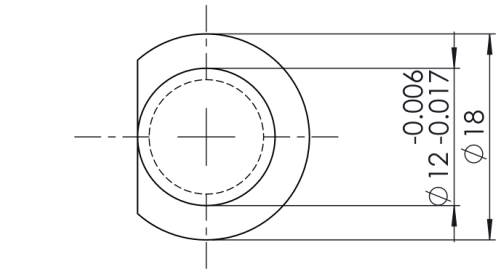

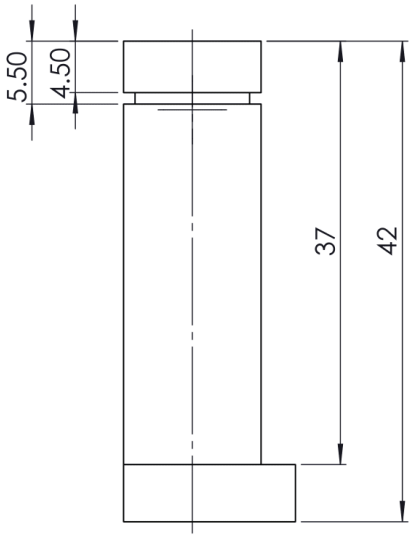

A4 Portrait	University of Cape Town Department of Mechanical Engineering			
	Title: Piston_Head_Thru_Pin			
Part Finish	Scale: 2:1	Date: 2019/08/08	Sheet1	of 1
Material:	Drawn By: DUSTIN FISCHER		Drawing Number P9	

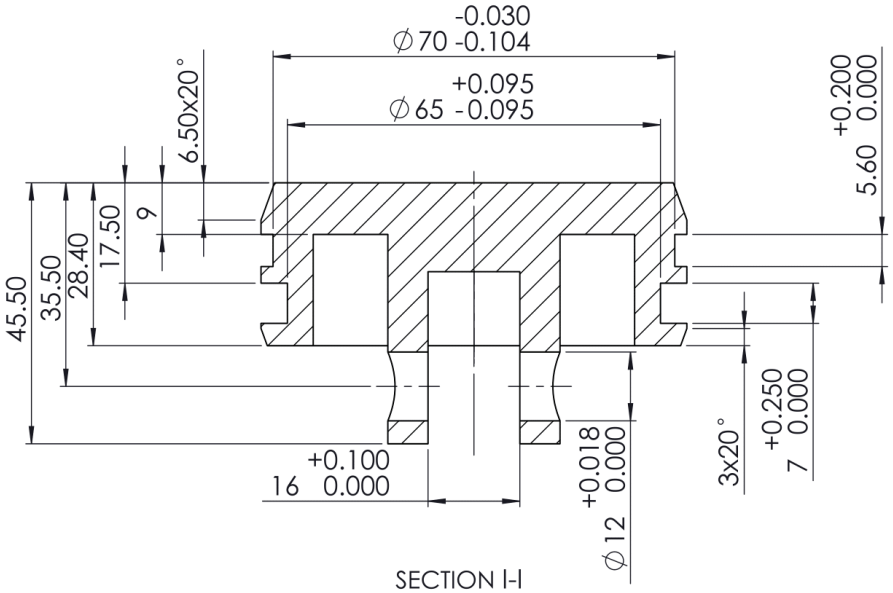

SECTION I-I

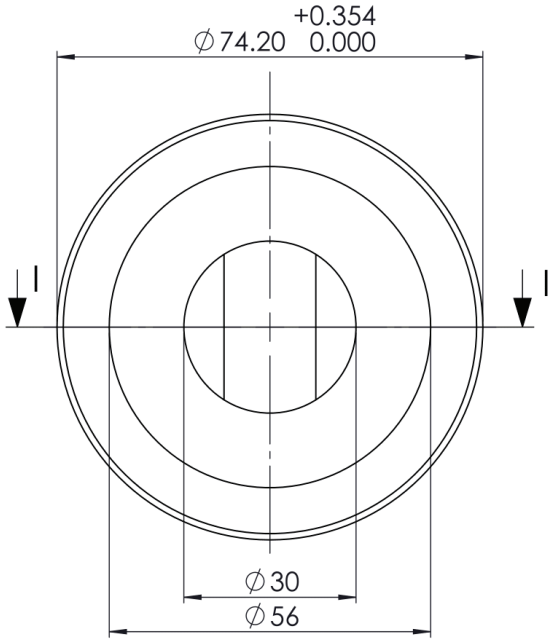

A4 Portrait	University of Cape Town Department of Mechanical Engineering			
	Title: Piston_Head_75OD			
Part Finish	Scale: 1:1	Date: 2019/08/08	Sheet1	of 1
Material: MILD STEEL	Drawn By: DUSTIN FISCHER		Drawing Number P10	

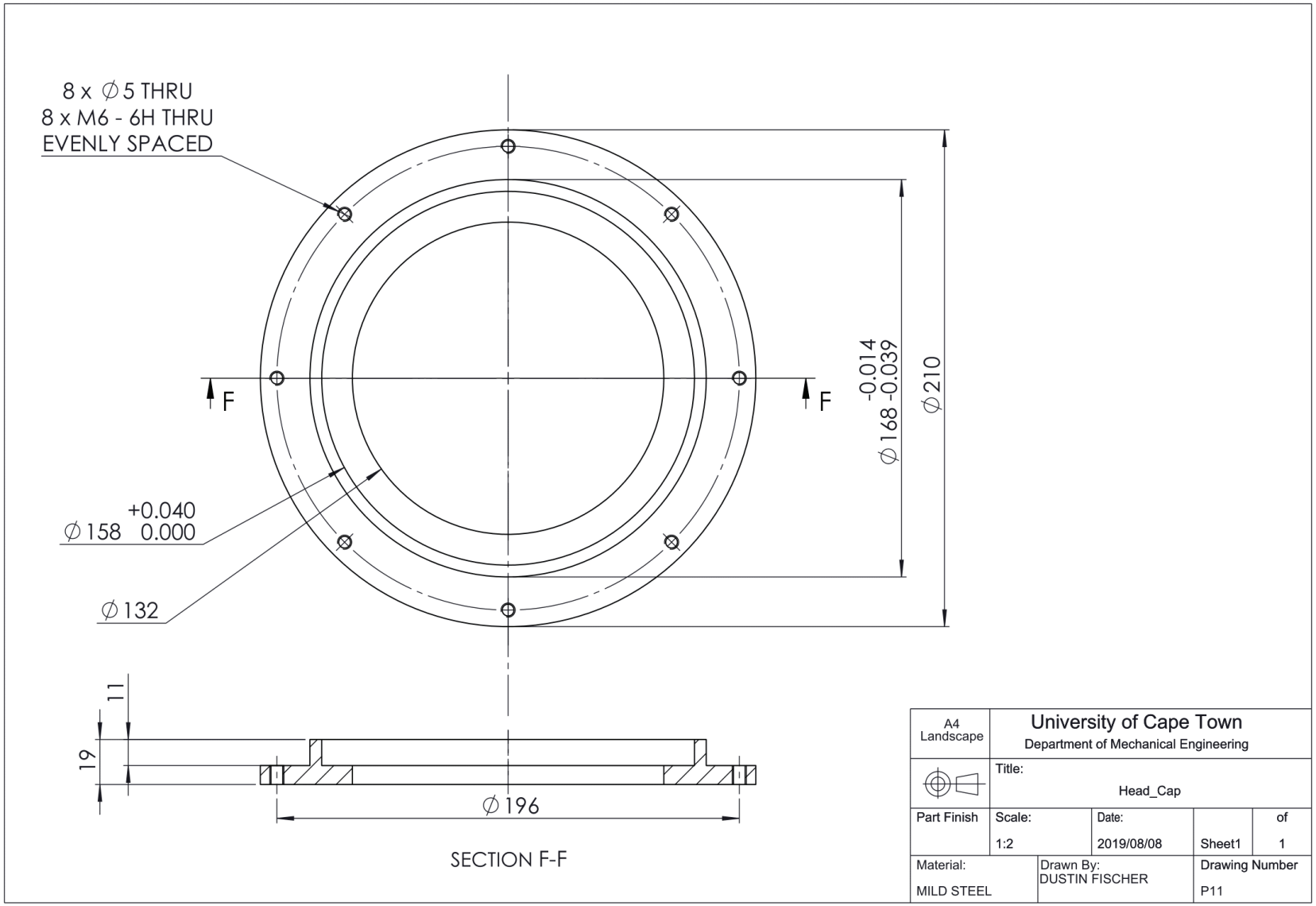
8 x ∅5 THRU
8 x M6 - 6H THRU
EVENLY SPACED
F
F
∅210
-0.014
∅168 -0.039
+0.040
∅158 0.000
∅132
11
19
∅196
SECTION F-F
A4
Landscape
University of Cape Town
Department of Mechanical Engineering
Title:
Head_Cap
Part Finish
Scale:
1:2
Date:
2019/08/08
Sheet1
of
1
Material:
MILD STEEL
Drawn By:
DUSTIN FISCHER
Drawing Number
P11

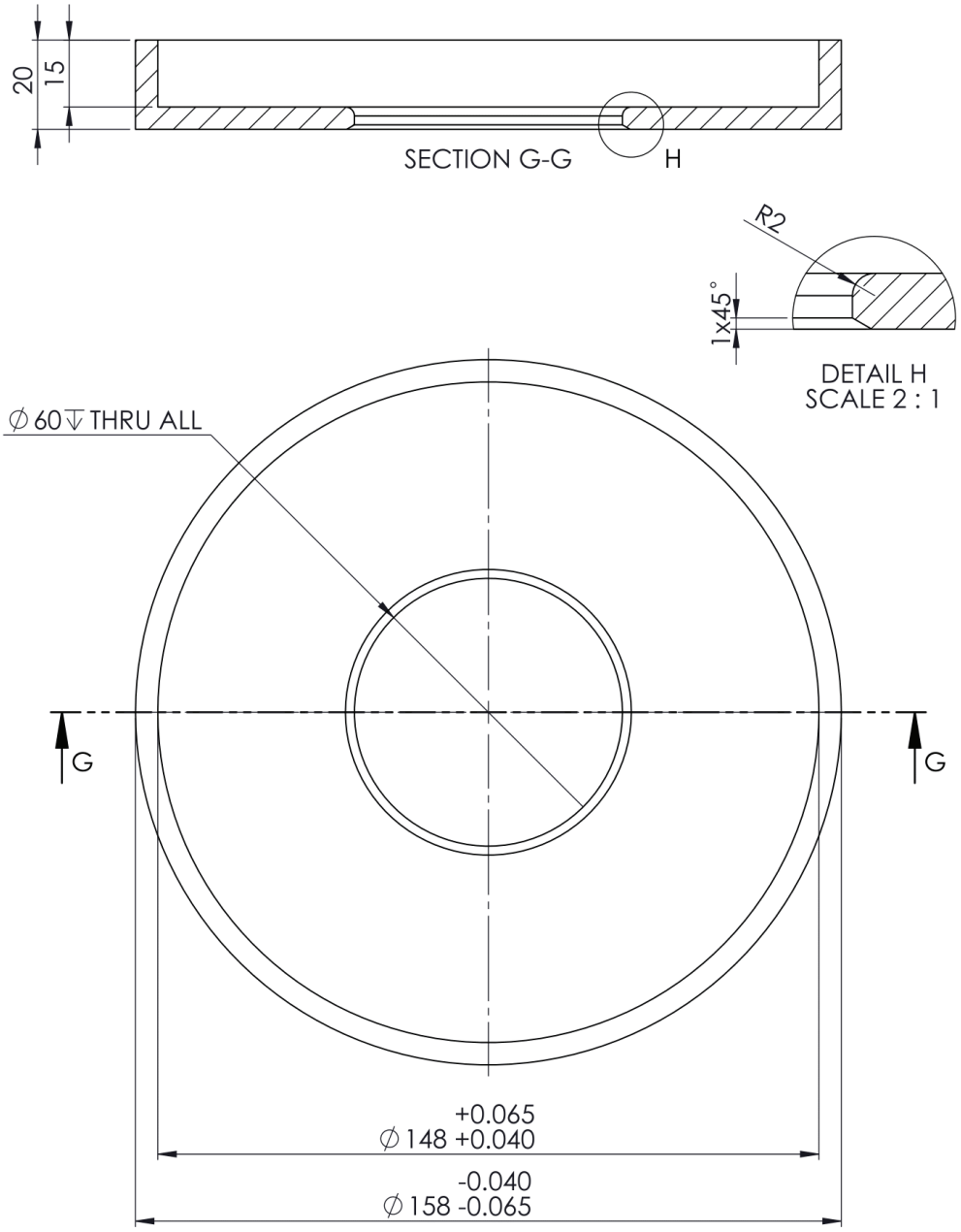

A4 Portrait	University of Cape Town Department of Mechanical Engineering			
	Title: Head_sample_adapter_D60			
Part Finish	Scale: 1:1.25	Date: 2019/08/08	Sheet1	of 1
Material: MILD STEEL	Drawn By: DUSTIN FISCHER		Drawing Number P12	

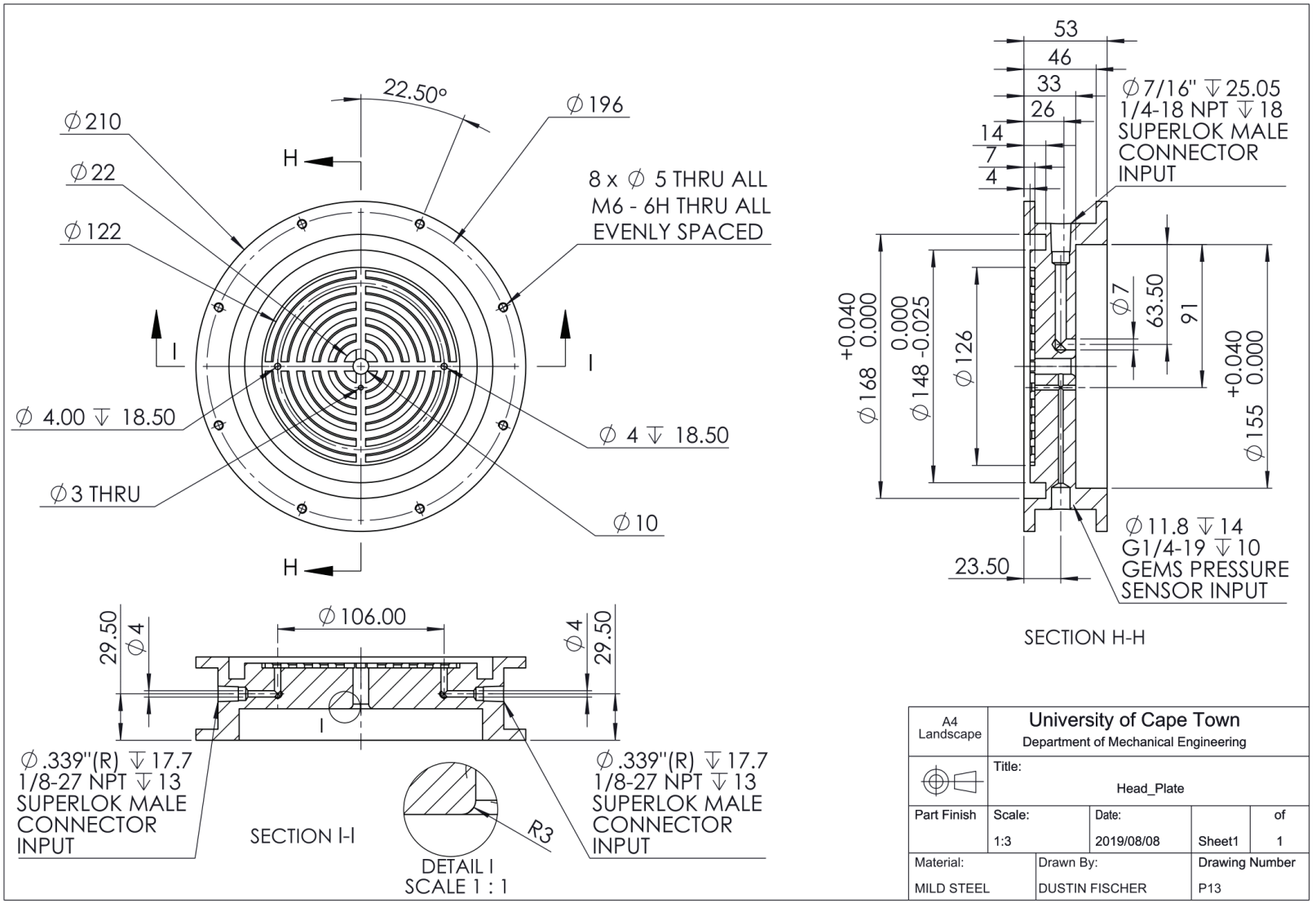
22.50°
∅210
∅22
∅122
∅196
8 x ∅ 5 THRU ALL
M6 - 6H THRU ALL
EVENLY SPACED
H
I
∅ 4.00 ↧ 18.50
∅3 THRU
∅ 4 ↧ 18.50
∅10
∅106.00
29.50
∅4
∅.339"(R) ↧17.7
1/8-27 NPT ↧13
SUPERLOK MALE
CONNECTOR
INPUT
SECTION I-I
R3
DETAIL I
SCALE 1 : 1
53
46
33
26
14
7
4
∅7/16" ↧25.05
1/4-18 NPT ↧18
SUPERLOK MALE
CONNECTOR
INPUT
+0.040 0.000
∅168
0.000 -0.025
∅148
∅126
∅7
63.50
91
+0.040 0.000
∅155
23.50
∅11.8 ↧14
G1/4-19 ↧10
GEMS PRESSURE
SENSOR INPUT
SECTION H-H
A4 Landscape
University of Cape Town
Department of Mechanical Engineering
Title:
Head_Plate
Part Finish
Scale: 1:3
Date: 2019/08/08
Sheet1
of 1
Material: MILD STEEL
Drawn By: DUSTIN FISCHER
Drawing Number P13

Appendix B

Additional Feedback Control Design Details

This appendix provides additional information relating to the design of the analog and subsequent discrete proportional-integral (PI) feedback control system. This includes a transfer function model description of a general pressure vessel system, measurement of physical control system parameters, fundamental root locus feedback control system design methodology that was used, and a fully worked solution of the sampled and quantised physical plant transfer function.

B.1 Deformable Pressure Vessel Model

A schematic representation of a pneumatically pressurised vessel is illustrated in Figure B-1. The proceeding pneumatic system modelling approach, which is illustrated in Figure B-1 (a), was described by Ogata [60]. Figure B-1(b) shows an analogous electrical Resistive-Capacitive (RC) series circuit equivalent which is used in this section to elucidate the approach described in [60].

A small actuated pressure stimulus p_i disturbs the system which is originally in equilibrium at pressure $\bar{P}$. Gas flow $\dot{m}$ flows through a pneumatic resistance R into the pressure vessel which has a pneumatic capacitance C. This results in a dynamic pressure rise p_o in the pressure vessel.

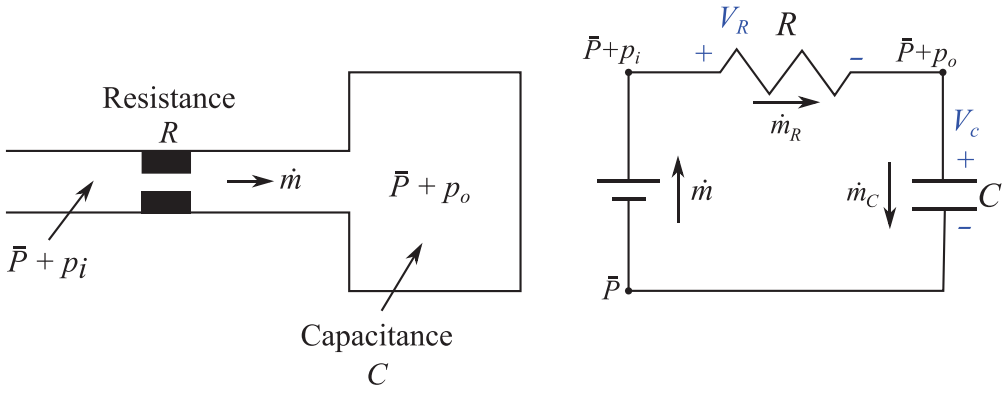

(a) (b)

Figure B-1: Schematic of a pneumatic pressure vessel (a) physical configuration - reproduced from [60] (b) electrical RC circuit equivalent

Pneumatic flow resistance is defined as the rate of change of pressure with flow

$$R = \frac{d(p_i - p_o)}{d\dot{m}} \tag{B.1}$$

Flow resistance changes with increasing flow rate but can be estimated as constant about an operating point. Flow through the resistance is then analogous to electrical current flow through a resistor $I_R = V_R/R$

$$\dot{m}_R = \frac{p_i - p_o}{R} \tag{B.2}$$

Pneumatic capacitance is defined as the rate of change of mass with pressure

$$C = \frac{dm}{dp} \tag{B.3}$$

For small changes in state its value can also be approximated as constant about an operating point. Flow into the vessel is then analogous to electrical current flow in a capacitor $I_C = C\ (dV_C/dt)$

$$\dot{m}_C = C\frac{dp_o}{dt} \tag{B.4}$$

Without additional mass storage, the flows given by (B.2) and (B.4) must balance, thus giving the following equation

$$\frac{p_i - p_o}{R} = C\frac{dp_o}{dt} \tag{B.5}$$

Taking the Laplace transform of (B.5) gives

$$\frac{P_i(s) - P_o(s)}{RC} = sP_o(s) \quad \cancel{-p_o(t=0)} \tag{B.6}$$

Rearranging (B.6) gives a first-order transfer function model for the pneumatic pressure vessel system shown in Figure B-1, which describes the pressurisation in the Laplace domain.

B.1.1 With a Deformable Boundary

The bulge testing apparatus would have a deformable boundary due elasticity of the test specimen. If the system shown in Figure B-1(a) is a pressure vessel with deformable walls, then flow into the vessel can be decomposed into a volume change term at constant density ρ, and a compressible term at constant volume V respectively [71]

$$\frac{dm}{dt} = \frac{d(\rho V)}{dt} = \rho\frac{dV}{dt} + V\frac{d\rho}{dt} \tag{B.7}$$

This leads to a form equivalent to (B.4) which shows capacitance is comprised of an incompressible volume change term C_v, and an isochoric gas compressibility term C_ρ

$$\frac{dm_C}{dt} = \frac{dp_o}{dt}\left(\rho\frac{dV}{dp_o} + \mathrm{V}\frac{d\rho}{dp_o}\right) = (C_v + C_\rho)\frac{dp_o}{dt} \tag{B.8}$$

B.1.2 Bulge Testing Configuration with Segregated Pressure Chambers

The pressure vessel schematic for the bulge testing apparatus is shown in Figure B-2 (a). Pressure in the lower cylinder drives the piston and multiplies the pressure in the upper cylinder by the piston gain k such that

$$p_o' = kp_o \tag{B.9}$$

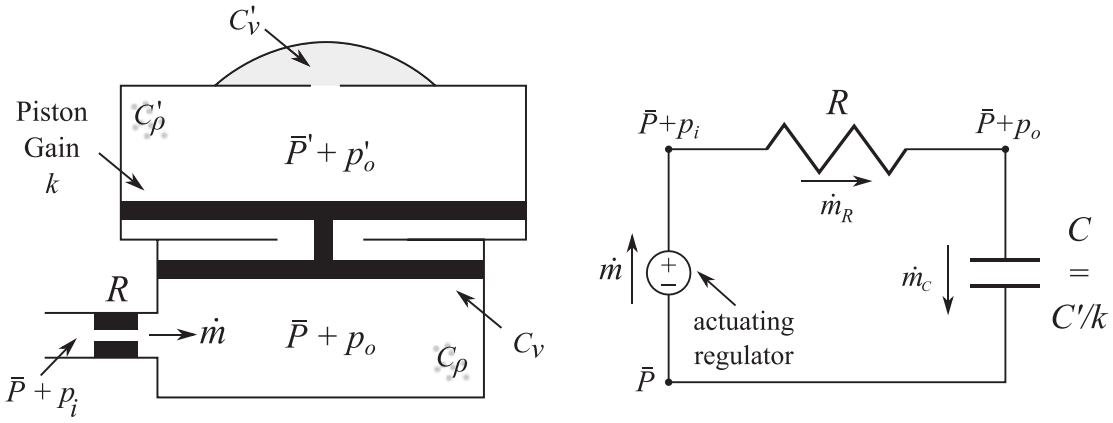

(a) (b)

Figure B-2: Schematic of the bulge testing apparatus pressure vessel system model
(a) physical configuration (b) pneumatic RC circuit electrical equivalent

The upper cylinder could be pneumatically or hydraulically pressurised. In the case of the latter the capacitance from compressibility is zero. The analogous electrical RC series circuit equivalent for the lower cylinder is illustrated in Figure B-2 (b). Flow into the lower cylinder is affected by the capacitance of the upper cylinder. Although the upper cylinder has a fixed fluid mass, flow into the system ($\dot{m}_c$) is affected by the upper cylinder such that

$$\dot{m}_c = C' \frac{dp_o'}{dt} \tag{B.10}$$

Or equivalently,

$$\dot{m}_c = (C'/k) \frac{dp_o}{dt} \tag{B.11}$$

Capacitance of the lower cylinder depends on the capacitance of the upper cylinder, where

$$C = C'/k \tag{B.12}$$

The input transfer function for the lower cylinder is obtained by combining (B.6) with (B.12)

$$\frac{kP_o(s)}{P_i(s)} = \frac{k}{(RC')s + k} \tag{B.13}$$

B.2 Measurement of Control System Delay Parameters

The step response measurement of the pressure sensor's first-order measurement time-constant $\tau_m \approx 20ms$ is shown in Figure B-1. This was performed *ad hoc* opening a solenoid valve and measuring the time response, which was assumed to have zero output delay.

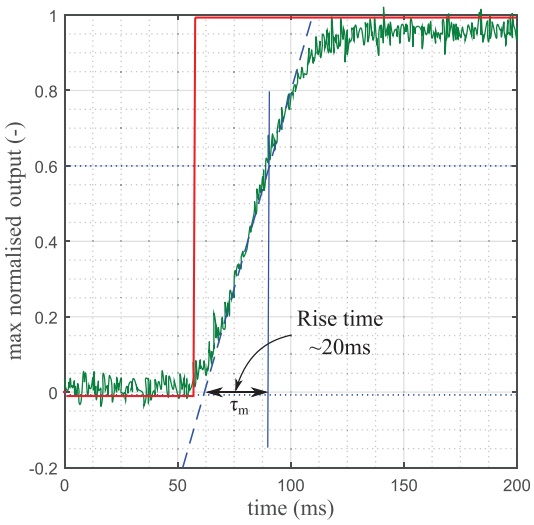

Figure B-3: Step response measurement of the pressure sensor

The step response measurement for the pressure regulator actuator's output delay $T_d \approx 50ms$ is shown in Figure B-4. This was performed by comparing a step voltage to the regulator's control input and measuring the output pressure response with the pressure sensor.

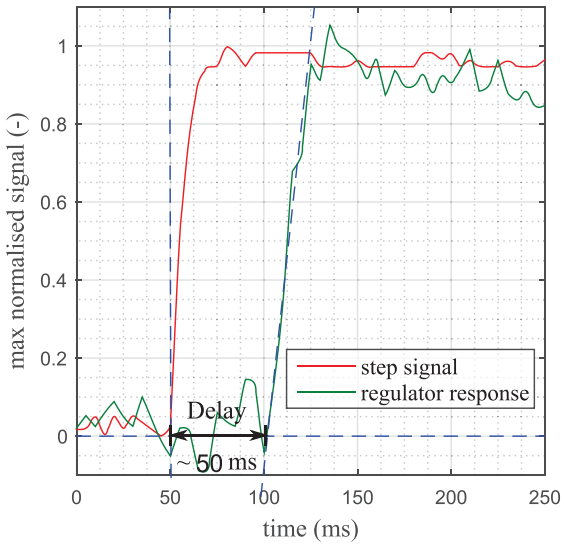

Figure B-4: Step response measurement of the pressure regulator actuator

B.3 Root Locus PI Controller Design Methodology by Pole-Zero Addition

A closed loop system, which has loop gain $L(s)$ and free proportional loop gain parameter k, is described by the transfer function

$$\frac{Y(s)}{U(s)} = \frac{kL(s)}{1 + kL(s)} \tag{B.14}$$

The poles of (B.14) are described in the s-plane by the characterisitc equation

$$1 + kL(s) = 0 \tag{B.15}$$

Root-locus design is driven by the placement of a single pair of conjugate poles $s_{cl} = \sigma \pm j\omega$ which dominate the transient dynamics of the closed-loop system. This assumes that the closed-loop system dynamics can be second-order approximated. Therefore, (B.15) may be estimated by a second-order system characteristic equation

$$s^2 + 2\xi\omega_n s + \omega_n^2 = 0 \tag{B.16}$$

where the damping ratio ξ, and natural frequency ω_n are second-order parameters that estimate the dynamics of (B.14). Dominant poles are manually located in the stable s-plane (i.e. to the left of the $j\omega$-axis) where specified second-order dynamics per (B.16) are met.

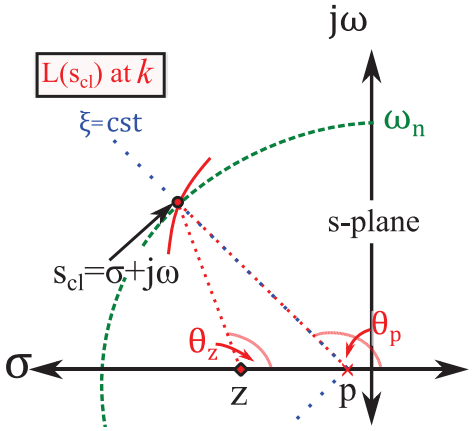

Figure B-5: Pole-zero diagram for a compensated closed loop system with loop gain $kL(s)$

Adapted from information presented in [51]

Dominant pole location was done by adding a compensating pole-zero pair (p, z) to satisfy performance specifications (ξ, ω_n). Figure B-5 illustrates a pole-zero compensated system in which a controller angle contribution ϕ is added to the original poles of the root locus for $L(s)$ to meet performance specifications at s_{cl}, where

$$\begin{aligned} \phi &= \theta_p - \theta_z \\ &= (\angle s_{cl})_{|p} - (\angle s_{cl})_{|z} \end{aligned} \tag{B.17}$$

B.4 Discrete Transfer Function for the Combined Plant, DAC, and ADC

The analog plant transfer function for the bulge testing apparatus with transport delay T_d was shown in the report to be

$$P(s) = \frac{e^{-sT_d}}{\tau_p s + 1} \tag{B.18}$$

The system was sampled by the ADC at a period of T seconds. Separating the delay term from (B.18) and taking the z-tranform gives

$$\mathbb{Z}\{e^{-sT_d}\} = z^{-\frac{T_d}{T}} \tag{B.19}$$

The ADC sampling and DAC output zero-order hold were combined with remaining analog process transfer function $P'(s) = 1/(\tau_p s + 1)$ to obtain the discrete sampled and held plant transfer function

$$\begin{aligned} G'_{zas}(z) &= (1 - z^{-1})\, \mathbb{Z}\left\{\frac{P'(s)}{s}\right\} \\ &= (1 - z^{-1})\, \mathbb{Z}\left\{\frac{1/\tau_p}{s(s + 1/\tau_p)}\right\} \end{aligned} \tag{B.20}$$

Taking partial fractions of the z-transform argument

$$\begin{aligned} \frac{(1/\tau_p)}{s(s + 1/\tau_p)} &= \frac{A}{s} + \frac{B}{s + 1/\tau_p} \\ &= \frac{A(s + 1/\tau_p) + Bs}{s(s + 1/\tau_p)} \end{aligned} \tag{B.21}$$

and comparing the LHS and RHS numerators of (B.21) to solve for A and B at $s = 0$ and $s = -1/\tau_p$ respectively gives

$$\frac{P'(s)}{s} = \frac{1}{s} - \frac{1}{s + 1/\tau_p} \tag{B.22}$$

Taking the z-transform of (B.22) gives

$$\begin{aligned} \mathbb{Z}\left\{\frac{P'(s)}{s}\right\} &= \mathbb{Z}\left\{\frac{1}{s}\right\} - \mathbb{Z}\left\{\frac{1}{s + 1/\tau_p}\right\} \\ &= \left(\frac{1}{1 - z^{-1}}\right) - \left(\frac{1}{1 - z^{-1}e^{-T/\tau_p}}\right) \end{aligned} \tag{B.23}$$

Substituting (B.23) into (B.20) and combining with (B.19) gives the zero-order held and sampled discrete transfer function equivalent for the plant given by (B.18)

$$\begin{aligned} G_{zas}(z) &= \left(z^{-\frac{T_d}{T}}\right)\left(\frac{1 - e^{-T/\tau_p}}{z - e^{-T/\tau_p}}\right) \\ &= delay(z)\left(\frac{1 - e^{-T/\tau_p}}{z - e^{-T/\tau_p}}\right) \end{aligned} \tag{B.24}$$

which is valid for $\forall z$ which satisfy

$$e^{-T/\tau_p} < |z| < 1 \tag{B.25}$$

Appendix C

Instrumentation Configurations and Calibration

This appendix provides supplementary detail for the electronic instrumentation and equipment that were integrated with the bulge testing device. Information is provided for the electronic pressure regulator (EPR) actuator, pressure transducer sensor, and analog to digital converter (ADC) that were used. Functional detail, specifications, calibrations, and supporting electronic circuitry schematics are provided.

C.1 Electronic Pressure Regulator

C.1.1 Camozzi MX-PRO Series Proportional Regulator Description

A Camozzi MX-PRO series EPR was chosen as the primary pneumatic actuator for the piston-cylinder bulge testing device. A basic functional schematic for the device is shown in Figure C-1, and Table C-1 provides relevant device specifications from the datasheet. The device regulates a 10bar inlet pressure to a 0.5 – 10 bar outlet pressure, corresponding to a 0.5 – 10V analog control input signal. A Camozzi K8P micro regulator module automatically balances the control signal with an internally measured pressure signal continuously toggling solenoid valves which controls a pilot valve between the MX-PRO regulator and the K8P micro regulator.

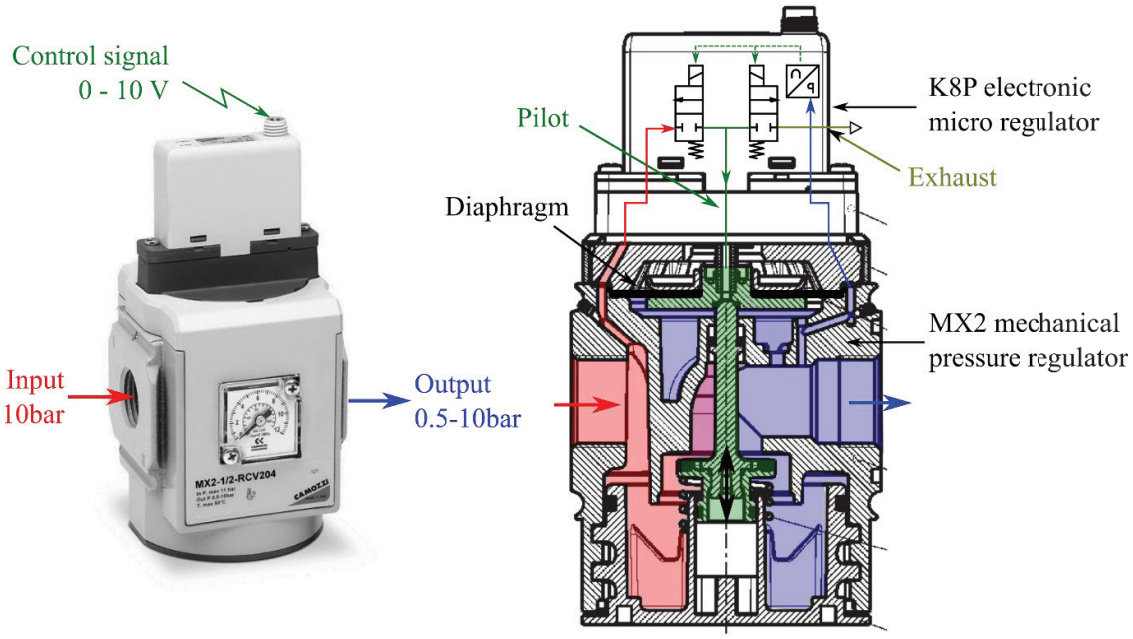

Figure C-1: Camozzi MX-PRO series EPR functional schematic. Adapted from [56] and [72]

Table C-1: Camozzi MX-PRO Electronic Proportional Regulator

Extracted from component datasheet [56]

Description	**Symbol**	**Value**	**Unit**
Inlet pressure	P_i	11 (max)	bar
Regulated pressure	P_o	0.5 – 10	bar
Control input	V_{cmd}	0 - 10	V_{DC}
Control ripple	$\tilde{v}_{cmd}$	<20	mV
Sensibility	S_{cmd}	50	mV
Supply voltage	V_s	19 - 28	V_{DC}
Pressure port	-	G1-2	inch

C.1.2 Electronic Circuitry Schematic

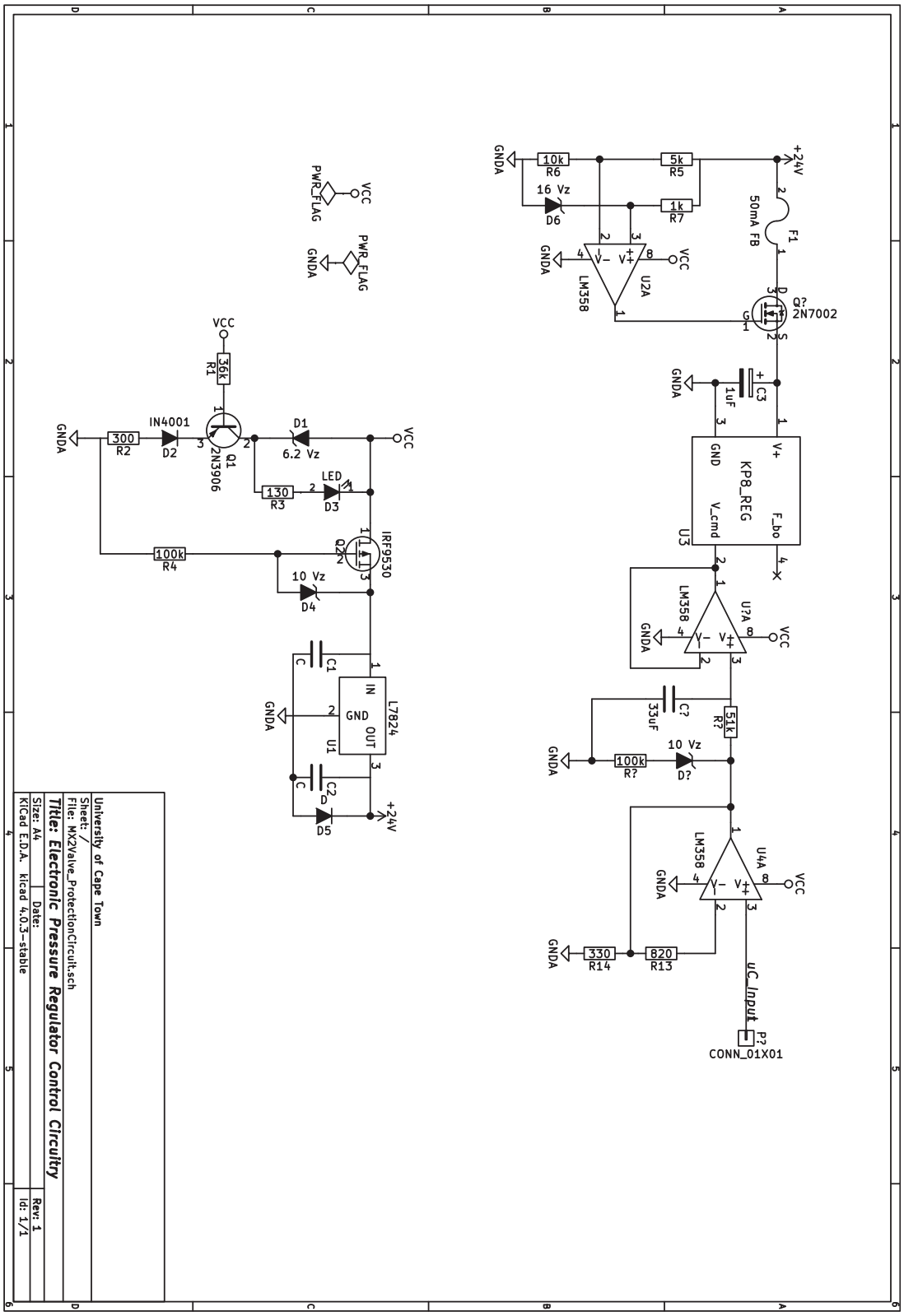

C.1.3 Electronic Circuitry Discussion

The Camozzi EPR device is rated for a 19 - 28V DC supply input and analog command signal input. Positive polarity protection was included on the circuit supply input V_{CC} using a P-channel power MOSFET to prevent damage from a potential reverse polarity error. The loop supply was decoupled from the EPR supply with a relay switch. The switch remains in a normally closed position only if the voltage comparator senses $V_{CC} < 24V$. Loop supply for the EPR circuitry is thus constrained as such

$$0V \leq V_{CC} < 24V \tag{C.1}$$

The operating range for the EPR's analog command input voltage signal is given

$$0.5V \leq V_{CMD} < 10V \tag{C.2}$$

The command signal was set using a 10bit DAC contained in the STM32F4-Discovery MCU evaluation board platform. The full-scale range for the DAC's voltage signal output is given

$$0V \leq V_{DAC} \leq 2.95V \tag{C.3}$$

A simple non-inverting voltage gain amplifier configuration was used to level-shift the buffered DAC output to comply with the full-scale EPR input. The compliance gain was evaluated from the conventional non-inverting op-amp gain expression as follows

$$\begin{aligned} A_{amp} &= \frac{V_{out}}{V_{in}} = 1 + \frac{R_{13}}{R_{14}} \\ &= \frac{\lceil V_{CMD} \rceil}{\lceil V_{DAC} \rceil} = \frac{10}{2.95} = 3.4 \end{aligned} \tag{C.4}$$

This required an amplifier resistor ratio R_2/R_1 close to 2.4. A non-precision R_2 and R_1 resistor combination of value 35kΩ and 15kΩ respectively ($A_{amp} \approx 3.33$).

A 10V Zener diode was placed on the command signal input to ensure the input voltage saturates at 10V. The EPR's command input has a low ripple voltage tolerance ($< 20mV$). A low-pass RC filter was placed on the buffered DAC output to mitigate amplification of possible high frequency voltage noise components which had been observed *in situ*.

C.1.4 Calibration

The device was calibration tested twice to assess the physcial performance of the device against the equipement specifications. The control signal voltage was set using a variable power supply with a 100mV output resolution. The corresponding output pressure was measured using a 10bar master pressure gauge with 0.25% accuracy.

Figure C-3 shows the first calibration results up to a regulated pressure of 3bar in order to demonstrate the low-end scale behaviour for the device. The device has a 50mV sensibility which should correspond to a 50mBar (5kPa) output resolution for the device; the calibration results suggest that the actual minimum realisable output is lower at around 0.2bar.. Comparison of the targeted and measured signals indicate that the device performs adequately according to the output resolution specification. Some sporadic failed conversions were observed resulting in occasional 10kPa resolution.

Respective full scale calibration testing results are shown in Figure C-3 and Figure C-4. The results indicate adeqaute linear behaviour. At low pressures (less than 3bar) a nonlinear offset error between 0 and -150 mBar (-15 kPa) was observed which appeared to improve at higher pressures.

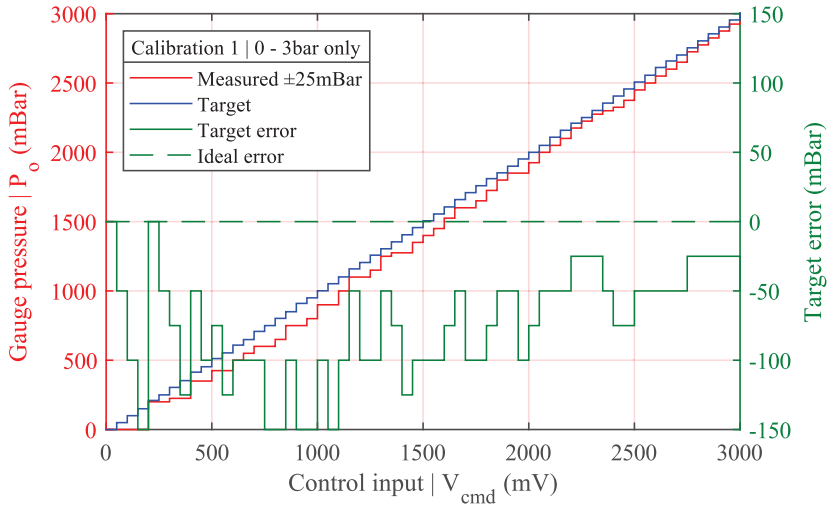

Figure C-2: Camozzi MX-PRO series EPR calibration (#1): 0-3 bar output

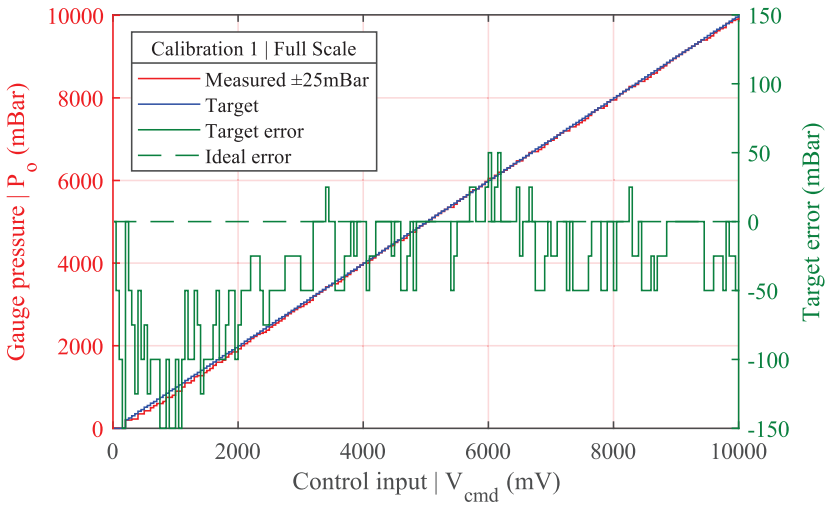

Figure C-3: Camozzi MX-PRO series EPR calibration (#1): 0-10 bar full-scale output

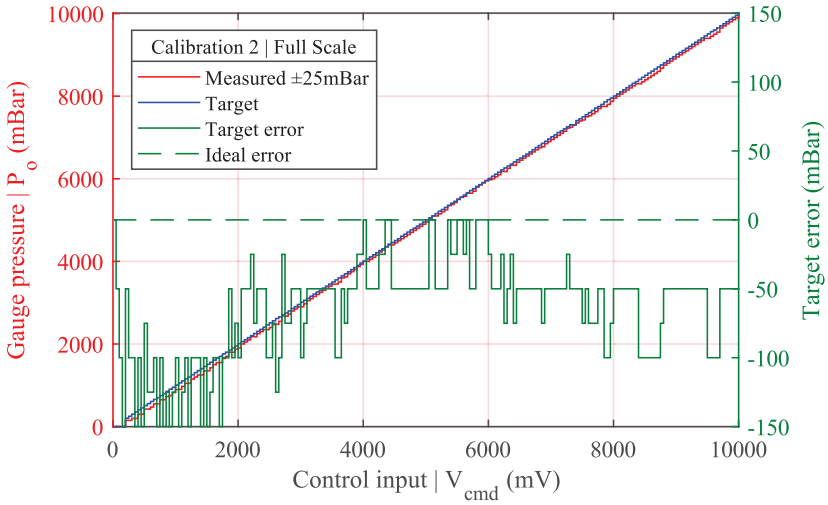

Figure C-4: Camozzi MX-PRO series EPR calibration (#2): 0-10 bar full-scale output

C.2 Pressure Transducer Sensor

C.2.1 Gems Series 31IS Transducer Description

A Gems Sensors and Controls 31ISB0010G01R000 analogue pressure transducer sensor was chosen for the bulge testing apparatus prototype in this project. A brief functional schematic for the device is shown in Figure C-5. The device converts a 0 - 10bar input pressure (pneumatic or hydraulic) to a 4 – 20mA output current signal; a 0mA output signal indicates the presence of a device or measurement line fault. The 4-20mA current signal passes through a mandatory load resistor R_L, and the signal is converted to a sensible 0-5V output using a

Texas Instruments RCV420 precision-resistor load current converter [73] to convert the 4-20mA output signal to a sensible 0-5V output signal. Table C-2 provides salient device specifications from the equipment datasheet.

Table C-2: GEMS 31ISB0010G01R000

Pressure transducer specifications [74]

Description	**Symbol**	**Value**	**Unit**
Pressure range	P_s	0 - 10	bar
Measurement output	I_M	4 - 20	mA
Supply voltage	V_s	8 - 24	V
Load resistor	R_L	$50(V_s - 8)$	Ω
Accuracy	-	0.25	% full scale
Pressure port	-	G1-4	inch

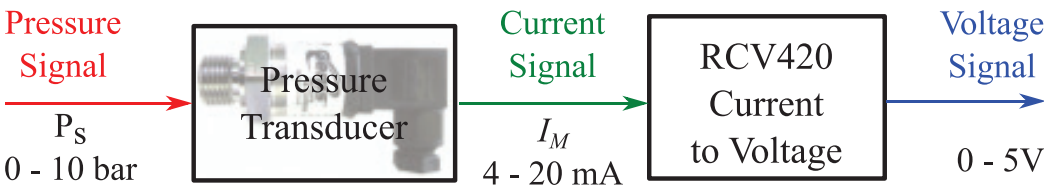

Figure C-5: Pressure transducer voltage sensing configuration

C.2.2 Electronic Circuitry Schematic

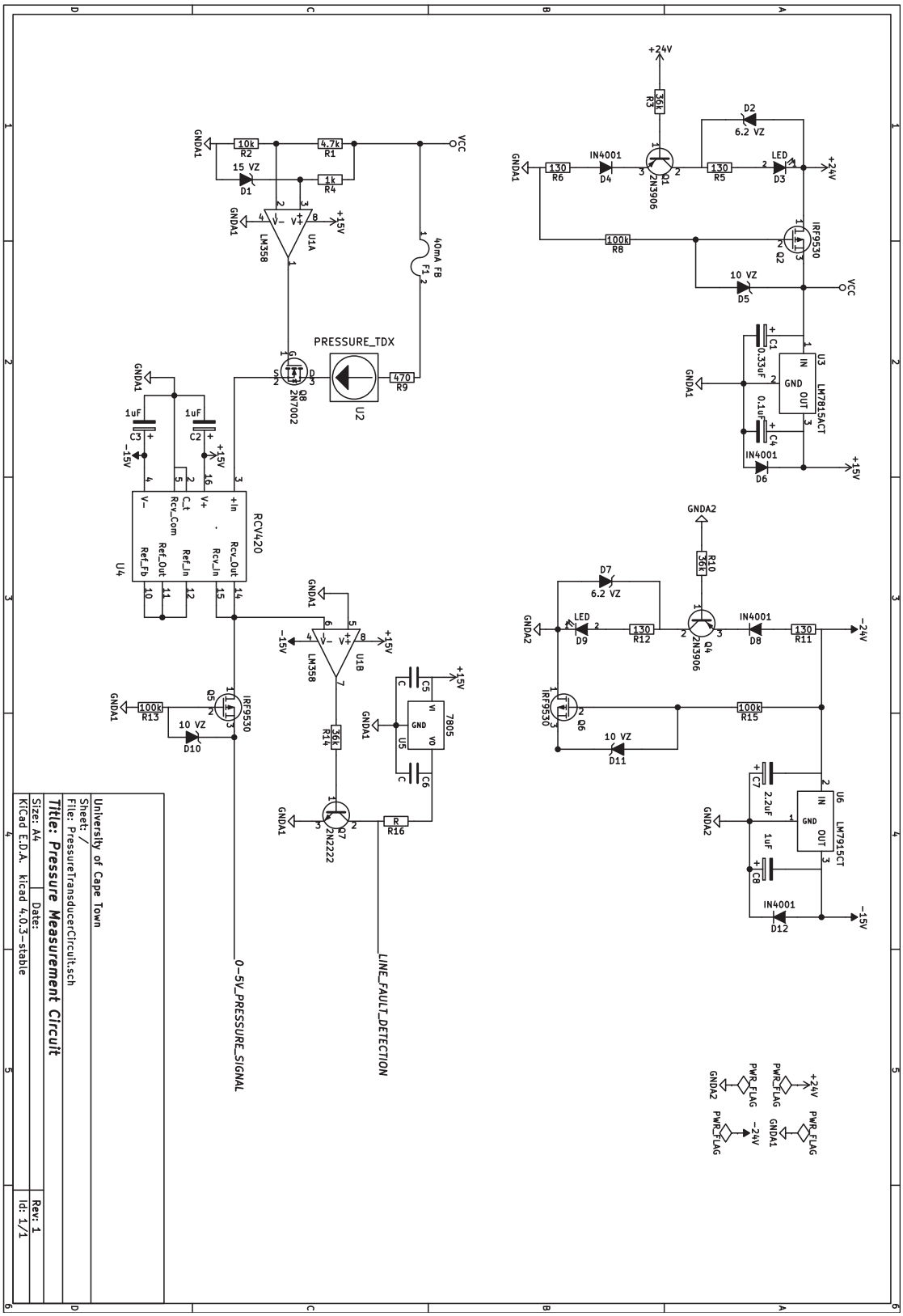

C.2.3 Electronic Circuitry Discussion

Incorrect polarity on either the RCV420 IC or the tansducer supply inputs could be potentially fatal to the component. P-channel power MOSFET tansistors were used for reverse polarity protection to prevent damage from potential user supply input errors. Incorrect polarity on the input the gate-source voltage will be positive and charge will not be permitted to flow. Positive polarity protection was also included on the converted sensor voltage ouput to protect the ADC from the potential negtive voltage in open circuit.

The RCV420 IC requires a bipolar ±15V supply which requires regulation of the loop voltage. A ±24V bipolar power supply limitation and a 2V loss across each voltage regulator were assumed. Accordingly, the bipolar voltage supply requirements are

$$\begin{aligned} 17V \leq\ & V_{CC}^{+} \leq 24V \\ -24V \leq\ & V_{CC}^{-} \leq -17V \end{aligned} \tag{C.5}$$

An op amp logic output comparator was combined with a transistor switch to prohibit charge flow to the sensing components if the total positive loop supply voltage exceeds 24V.

The sensing voltage loop is shown in Figure C-6. Overcurrent protection was required for the 75Ω precision resistor on the RCV420, which is maximum rated for 40mA continuous current. A load resistor with resistance R_L is placed in series with the transducer and precision resistor to restrict the amount of current that can flow. A 4-20mA transducer requires a minimum compliance voltage V_{PT} to operate, and typically tolerates a wide range of voltage input. Voltage across the transducer depends on the current and loads in the path. The total loop supply V_{CC}^{+} is equal to the sum of potential drops along the path shown. The loop supply must be sufficient to tolerate the load voltage drops and still supply sufficient voltage to the transducer, therefore this implies that

$$V_{CC}^{+} - V_{PT} \geq I(R_L + 75) + 0.7 \tag{C.6}$$

The maximum load resistor value is then evaluated the at 40mA rated current and stipulating that the lowest tolerable transducer compliance voltage $\lfloor V_{PT} \rfloor$ occurs at this point

$$R_L \leq \frac{V_{CC}^{+} - \lfloor V_{PT} \rfloor - 0.7}{40mA} - 75 \tag{C.7}$$

The sensible compliance voltage can then be practically measured and adjusted at zero-scale ($I = 4mA$) using a potentiometer to match the appropriate transducer supply voltage given by

$$V_{PT} = V_{CC}^{+} - 4(R_L + 75) - 0.7V \tag{C.8}$$

A 40mA fast blow fuse was added for additional protection against a short circuit across the between the transducer terminals.

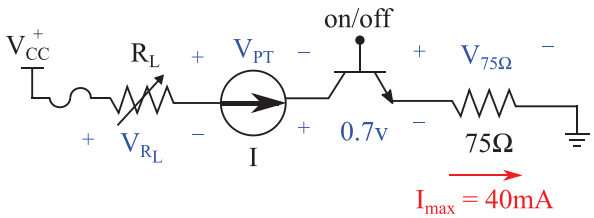

Figure C-6: Pressure sensing loop path

The bipolar ±24V input is grounded separately on each input (GNDA1 and GNDA2) (instead of a single common connection point between the two potentials). The two grounds are sourced from a single ground point but are split at the supply input. This was found to create a small potential difference between the two grounds which may be potentially problematic. This was not investigated further as the solution worked acceptably well for the project's application.

C.2.4 Calibration

The device was calibration tested twice to assess the physcial performance of the device against the equipement specifications. Input pressure was set using an adjustable pressure regultor and accurately measured using a 10bar master pressure gauge with 0.25% accuracy (i.e. 2.5 kPa or 25mBar accuracy). The corresponding output voltage signal was measured using an oscilloscope.

Calibration results are shown in Figure C-7 with corresponding linear fits. For an input pressure range of 0 – 10bar the device (inlucding the addtional current to voltage conversion circuitry) was expected to ouput a corresponding 0 – 5V signal. This corresponds to a proprtional voltage-pressure relationship

$$V(p) = 0.5(V/bar) \times p \tag{C.1}$$

where V is the output voltage and p is the inlet pressure. The results indicated the equipment operated with appropriate linearity. A positive zero-scale offset voltage error was present and was found to vary between indivudual applications. The offset error was therefore measured automatically prior to each usage and subsequently removed programatically.

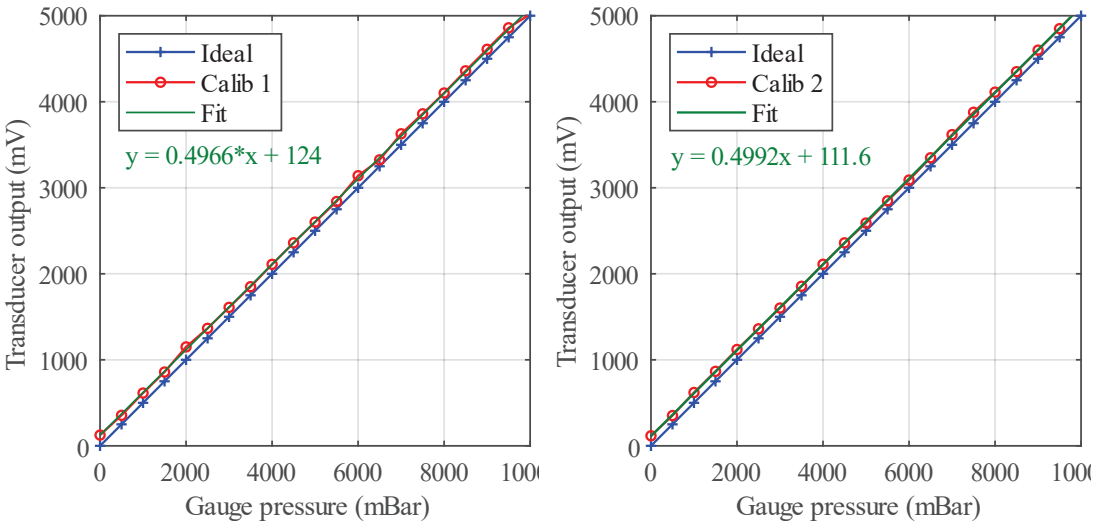

Figure C-7: GEMS 31ISB0010G01R000 pressure transducer calibration results

C.3 Analog to Digital Converter Electronic Circuitry Schematic

The following electronic circuitry schematic is for a PCB which was designed and fabricated to interface and operate with the AD7706 ADC IC chip used for the project. The design is adapted from a manufacturer evaluation board schematic given in [69].

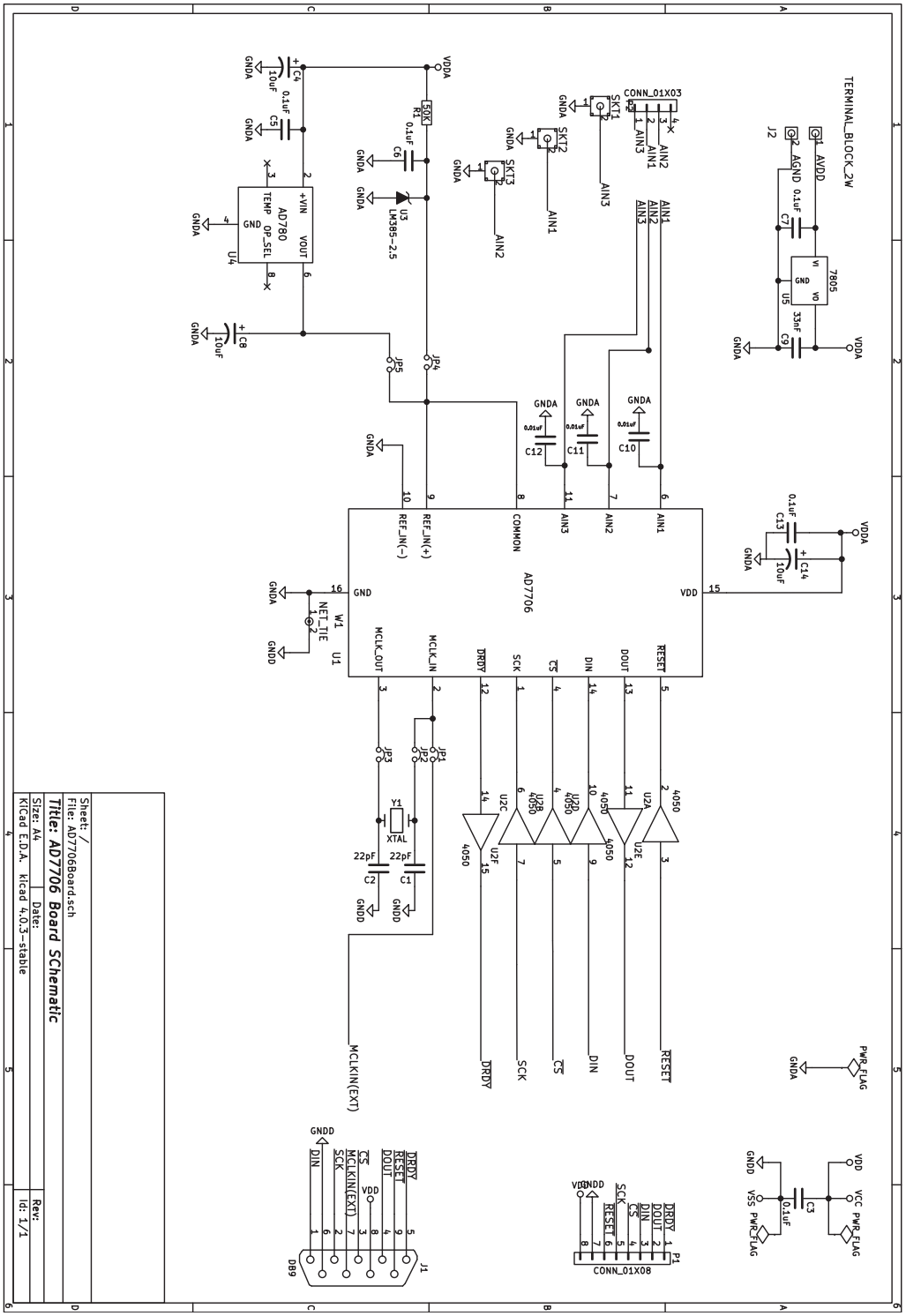

The electronic circuitry schematic for the PCB which was fabricated for the adapted evaluation board design is shown in Figure C-8.

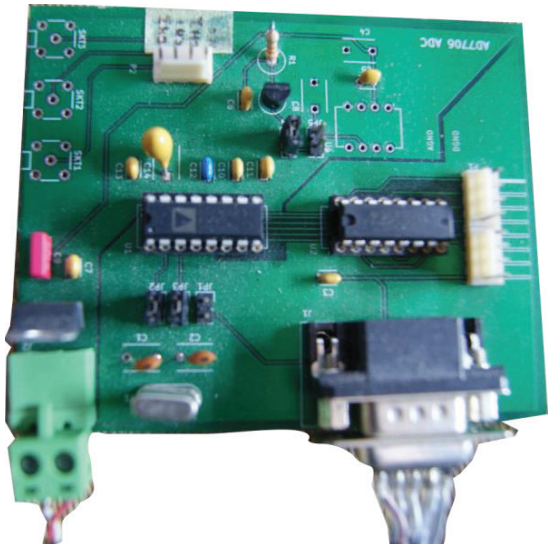

Figure C-8: Fabricated evaluation board for the AD7706 ADC IC

Appendix D

Interfacing and Operating Procedures

This appendix provides detailed operating procedures for the bulge testing device and associated testing platform. The user interface and step-by-step procedures are described.

Once the testing is instructed to resume, the back-end of the interface continues to receive test data from the controller (pressure data for the main application). The GUI displays and updates the received data as it is received in packets and decoded. When the microcontroller initiates its own test termination proceedings, the PC interface is notified. The test data is then collated and written to a single .csv file and stored in a filing system.

D.1 Operating Procedures

D.1.1 Initial Assembly

The fully assembled mechanical components of the bulge testing device, separate from the electronic and host PC controller interface, is shown in Figure D-1. The term bulge testing device in this context will be used to refer to the assembly shown.

Figure D-1: Fully assembled bulge testing device, with piston-cylinder apparatus connected to the base platform

The device requires manual (re)assembly of the mechanical piston-cylinder each time the bulge testing device is unused for extended periods of time, or a cylinder configuration other than the current configuration is used. The relevant mechanical components for the current prototype device configuration are labelled and shown in Figure D-2. The given numbering matches numbering shown in subsequent subassemblies using the numbered components.

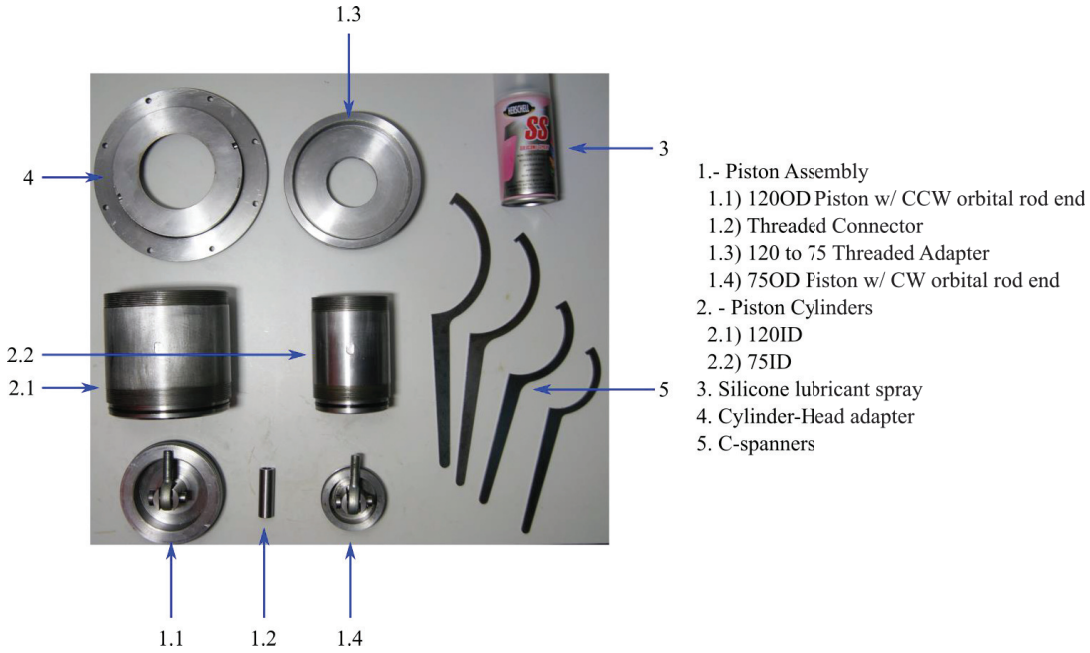

Figure D-2: Components for the piston-cylinder apparatus

The assembly of the piston-cylinder apparatus should be done separately from the base platform and merged only in the final stages of assembly. Assembly of the device is as follows:

1. Assemble the piston subassembly, with cylinder-cylinder adapter (1.3) (Locate rod end bearings with through-pins and fasten with circlips) included – see Figure D-3
2. Insert the piston cylinder subassembly into matching cylinders and tighten by hand as much as possible - see Figure D-4
3. Carefully insert the piston-cylinder subassembly into the base adapter on the base platform
4. Locate the cylinder-head adapter (4) on top of the piston-cylinder subassembly, tighten all concentric components with appropriately sized C-spanners, careful not to overtighten – see Figure D-5
5. Locate the orifice head on top of the cylinder-head adapter (4), affix with 6x15mm M8x1.75 bolts lined up with matching holes around the circumference

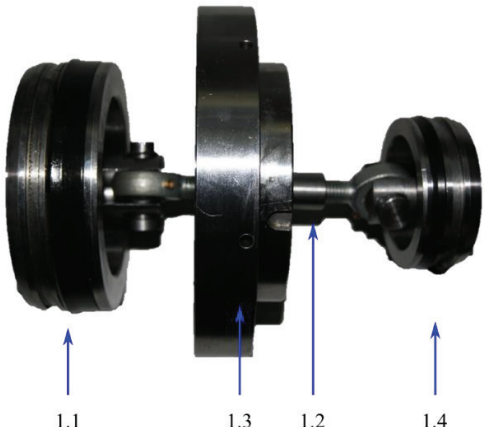

Figure D-3: Piston subassembly

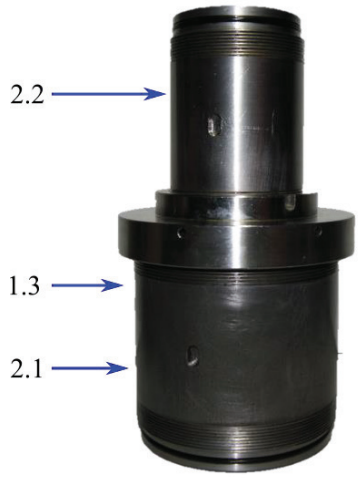

Figure D-4: Piston-cylinder subassembly

Figure D-5: Bulge testing device assembly

D.1.2 Current Sample Prepration and Clamping

Currently, the sample locating and clamping method is *ad hoc* and requires revision as it is not suitable for skin tissue, as samples need to be glued to a rigid annulus that can transmit sealing/clamping forces without defomring the specimen. The relevant components for the sample clamping assembly are shown in Figure D-6. The steps for assembling are as follows:

1. Mount and bond a material specimen to a slightly (~10mm) larger outer diameter laser cut wooden ring, and seal appropriately around the perimeter of the bonded interface - see (6.1)
2. Locate components in the order (6.1 -> 6.2) -> 6.3
3. Locate (step 2 result) on the orifice head
4. Locate the clamping cap concentrically with (step 3) – see Figure D-7
5. Tighten 8x25mm M8x1.75 in diamterically opposite pairs, in equal measures, to clam unifomrly around the cirmference

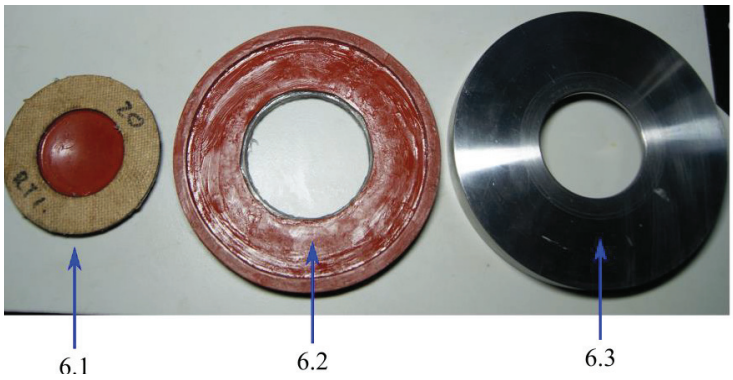

6. Sample Clamp Assembly
6.1) 50OD sample
6.2) *Ad hoc* gasket
6.3) 50OD sample adapter die

Figure D-6: Components for sample clamp assembly

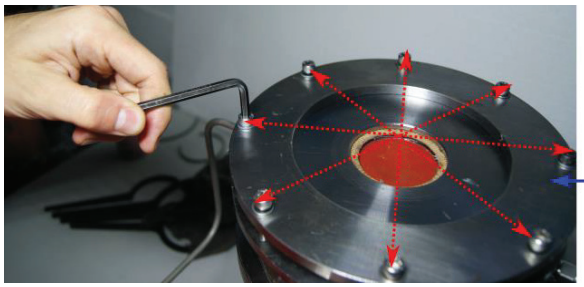

Figure D-7: Tightening of clamping cap bolts in diametrically opposite pairs

D.1.3 Test Configuration

The integrated testing environment for the platform is shown in Figure D-8 (not shown is the pressurised gas cannister to the left).

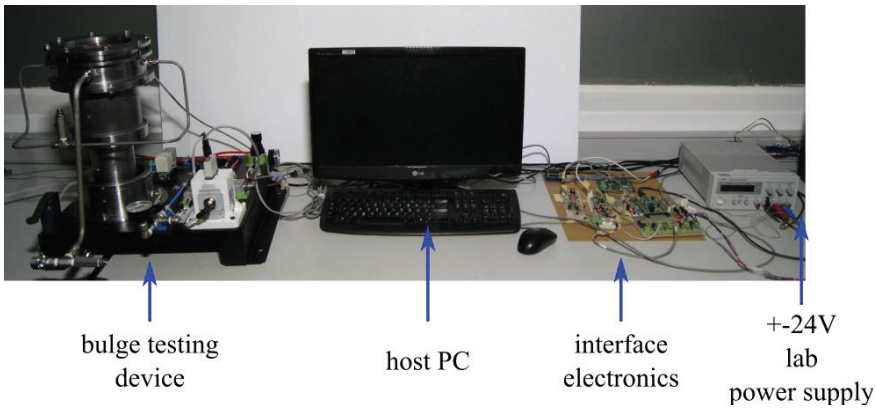

Figure D-8: Integrated testing environment

Configuration of a test once the user is ready to initiate testing proceedings requires the following steps:

1. Configure the isolating ball valves shown in Figure D-9 as follows
    a. Open
    b. Closed
    c. Set to desired needle valve restriction
    d. (control line) Open
    e. (vacuum line) Closed
2. Ensure pressure regulators are configured for their respective pressures
3. Turn on gas pressure supply
4. Connect the serial comm's USB cable from the interface electronics to the host PC (connected to the UART to USB converter)
5. Connect the MCU USB power cable to any 5V USB power supply
6. Ensure all electronic power connections are appropriately secured and switch on the ±24V power supply
7. Open the bulge testing software from the root folder in MATLAB and run the '*NewBulgeTest.m*' script from the command window
8. User will be presented with the graphical context menu shown in Figure D-10; enter all fields appropriately and click *Apply*. Note:
    a. The USB Serial COM port can be found from COM port devices in the Windows device manager named 'Prolific USB Converter'
    b. The '*Run Pretest*' radio button must only be selected if the feedback controller parameters need to be designed; this will initiate a pretesting routine to evaluate the first order rise time of the system configuration

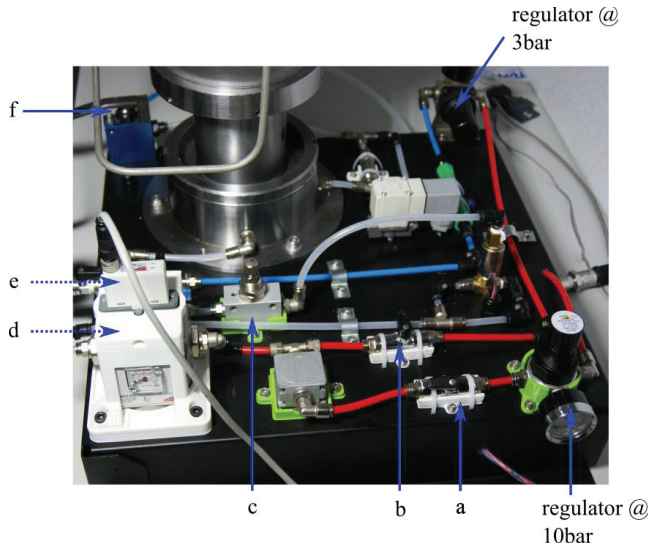

Figure D-9: Manual pneumatic controls reference

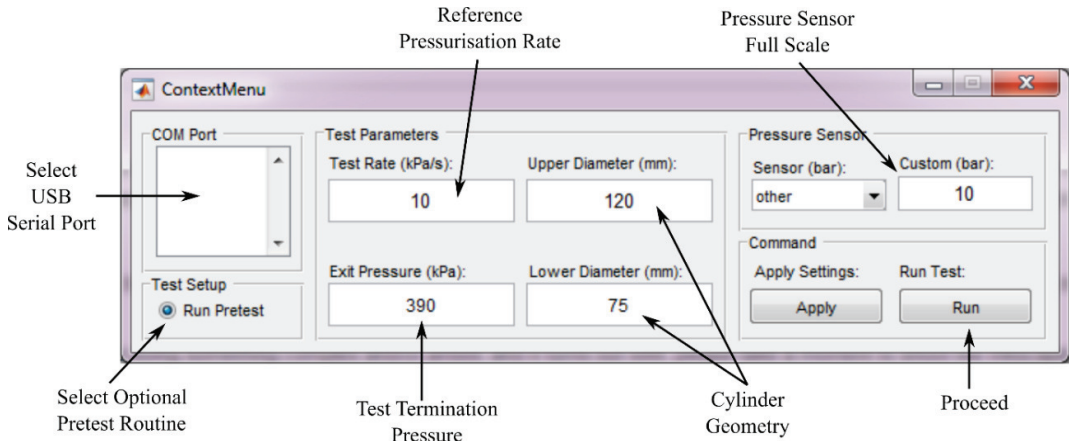

Figure D-10: Initial settings context menu

D.1.4 Initiating a Test

9. When ready to proceed, click *Run* which will initiate the automated initiation and calibration routine in the following order (takes about 30s):
    a. Identify the latency between the MCU and Host PC serial comms
    b. Configure and calibrate the ADC; measure the zero-scale offset reading of the pressure transducer as well
    c. Configure the DAC output
    d. Configures all serial and auxiliary data buffers
    e. Relay calibration data for transmitted data from the MCU to the PC

10. [**If** the '*Run Pretest*' radio button was selected a small automatically controlled pressure will be applied for 5s (about 5kPa) and then purged via the solenoid valves. The MATLAB pretest routine will analyse the pressure-time response and fit a first order system response to the data. This will then suggest feedback controller parameters (for the next step) for the fitted system response]
11. [Open an exposed (to atmosphere) valve in the top chamber, return the piston to the floor by closing the control line valve (d) and opening the vacuum line valve (e) (see Figure D-9)]
12. The user will be prompted with another context menu as shown in Figure D-11 once the controller gain and s-domain zero-locus parameters have been designed and/or selected (using the controller design chart presented in sect X)
13. Enter the appropriate feedback controller parameters – these must be carefully entered, then press apply
14. Check that valves are still as per (step 1)

D.1.5 Running the Test

15. Click '*Continue'*, which will initiate the pressurisation tests

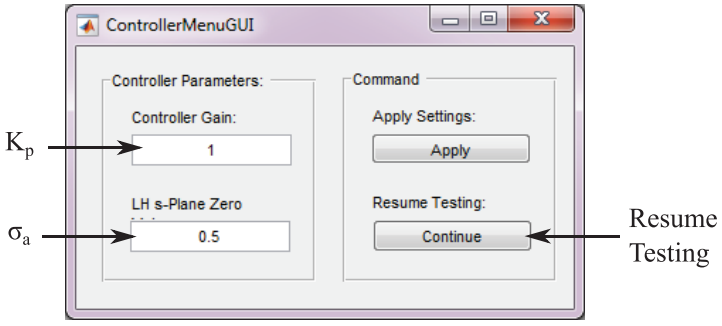

Figure D-11: Controller specification context menu

16. A small pressure will be applied (about 5kPa, for 5s) to establish a baseline pressure level
17. The feedback controller will automatically switch over and begin pressurisation at the specified rate

18. Data will automatically be sent from the MCU to the PC in fixed packet sizes (about 100ms worth)
19. Data is saved on the PC in sequential file chunks in increments
20. Once the test has been terminated (see proceeding), the sequential file chunks will be collated into a single comma separated .txt file with <time>, <data> header, where the data is pressure in Pa
21. The saved file is stored in a new folder in the program source folder (where it was run from) as follwoing:
    - <path to source code>/BulgeTestData/testdata_<current_date> (<number of test performed at current date>)
    - eg. <user name> /<source folder>/BulgeTestData/test_data_09011991 (5)

Terminating a Test

1. A test will automatically terminate if:
    a. Termination pressure is reached (specified in initial configuration)
    b. A rapid drop in pressure is registered:
        i. By sample rupture, or by
        ii. Manual exhaust override (toggling *f* in Figure D-9)
2. A test terminates with the following procedure:
    a. Termination is triggered by one of the above
    b. Pressure in the system is exhausted by the solenoid valves
    c. Notification of the termination is sent to MATLAB
    d. MATLAB registers termination notification, stops listening for new data, collates the exsiting data into a single test_data file, and terminates the program

Note: the MCU can be hard reset at any time by pressing the black reset button. Thereafter the user must restart from (step 1) of *Test Configuration*

Appendix E

Miscellaneous Software Routines

This appendix describes necessary software routines which were implemented to identify and monitor the running system. This includes a first-order system time response identification routine which was used for specification of custom feedback controller parameters. Also presented is a rupture detection routine algorithm which was implanted to identify the rapid pressure drop that is associated with bulge specimen rupture.

E.1 First Order Time Constant Identification Routine

A first order system has an exponentially decaying step response given by the equation

$$y(t) = \ y_f + (y_0 - y_f)e^{-t/\tau} \tag{E.1}$$

where τ is the rise time taken to reach 63% of the final state y_f from the initial state y_0 . The normalised response is obtained by dividing (E.1) by y_f

$$\hat{y}(t) = \ 1 + (\hat{y}_0 - 1)e^{-t/\tau} \tag{E.2}$$

Typical first order responses given by (E.1) and (E.2) are illustrated in Figure E-1(a). Rearranging the terms in (E.2) give the normalised argument expression

$$\hat{X} = \frac{\hat{y}(t) - 1}{\hat{y}_0 - \ 1} = e^{-t/\tau} \tag{E.3}$$

Taking the natural logarithm of the above expression, an augmented linear response with time is obtained

$$-ln\left(\hat{X}\right) = t/\tau \tag{E.4}$$

The inverse of the gradient of the line is equal to the rise time of the system. The augmented response in (E.4) is illustrated in Figure E-1(b). The response deviates from linearity as $\hat{X} \to 0$. The normalised order response is thus cropped between $\hat{y}_L < \hat{y}(t) < \hat{y}_U$ so that a linear best fit can be fitted to the cropped linear portion of the augmented response.

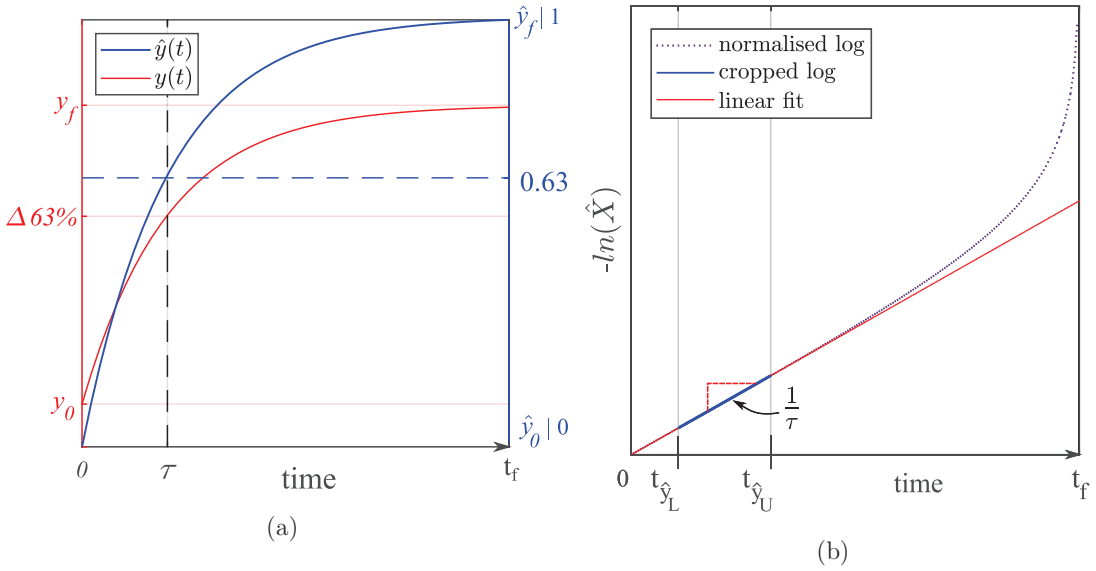

Figure E-1: First order system responses

(a) step (b) augmented log linear

E.1.1 Implementation

An example of an open-loop pressure step response that was obtained using the bulge testing apparatus is illustrated in Figure E-2. The first second was left inactive to determine an average baseline offset. The following pseudocode outlines the automatic curve fitting procedure that was integrated within the pretest routine to identify the first order response time of the system. The fitted data results are shown compared to the physical step response data in Figure E-2.

```
 This code evaluates the first order response time of a system from
a step input response by finding the inverse gradient of the linear
portion of then log argument equivalent of the step response given
by(E.4).

 START
     extract time and step response data vectors
     subtract minimum step response value from step response vector
    divide step response vector by maximum step response value
     set y0 equal to average of the data vector for 0s<time<1s
     set yf equal to 1
     remove 0.4<= step response <=0.8 from data vector
     remove 0.4<= step response <=0.8 from time vector
     evaluate log argument for the data vector
     fit linear best fit to the transformed time and data vectors
     set tau equal to the inverse of the fitted line gradient
 STOP
```

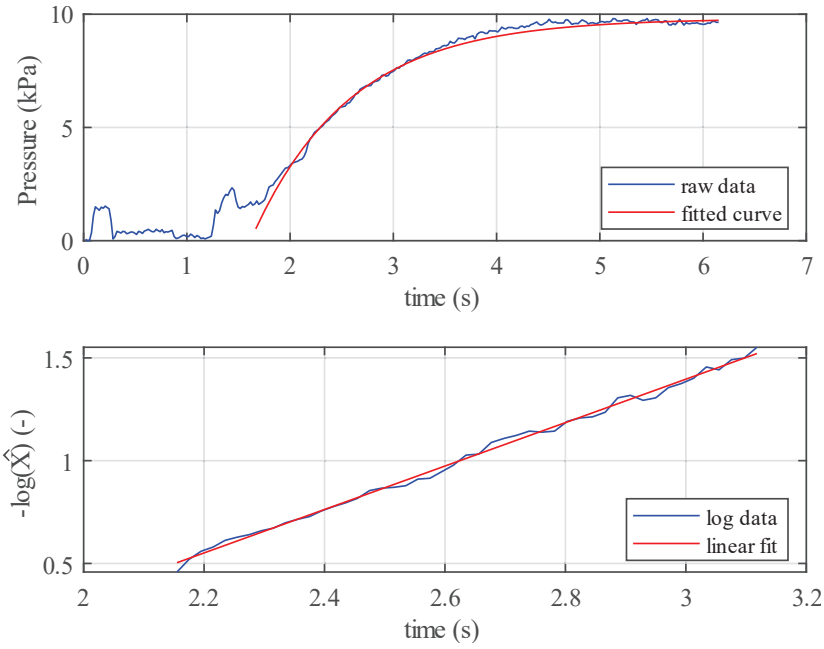

Figure E-2: Example of a fitted first order step response

E.2 Rapid Pressure Drop Detection

Rupture detection was implemented in the embedded software control system in order to arrest piston travel post rupture, and to try and mitigate fluid loss from the bulge chamber if a hydraulic medium were to be used.

Rupture was defined in the software as a short, sustained pressure drop of at least half compared to a historical maximum window. The most significant bit(s) (MSB) of a 150ms current measurement buffer-window (9 samples @ 60Hz sampling rate) were extracted by masking the Least Significant Bits (LSB) of the 16bit values and checked against a running 500ms historical maximum-MSB buffer-window.

The basic flow of the monitoring algorithm is shown in Figure E-3 for an unsuccessful (rising pressure) and a successful (rapid drop) buffer-window check. For rupture to be identified, the highest current buffer MSB must be at least one lower than the lowest historical MSB to trigger test termination. If new maximum values are recorded, they are copied to the historical buffer and older values are shifted out.

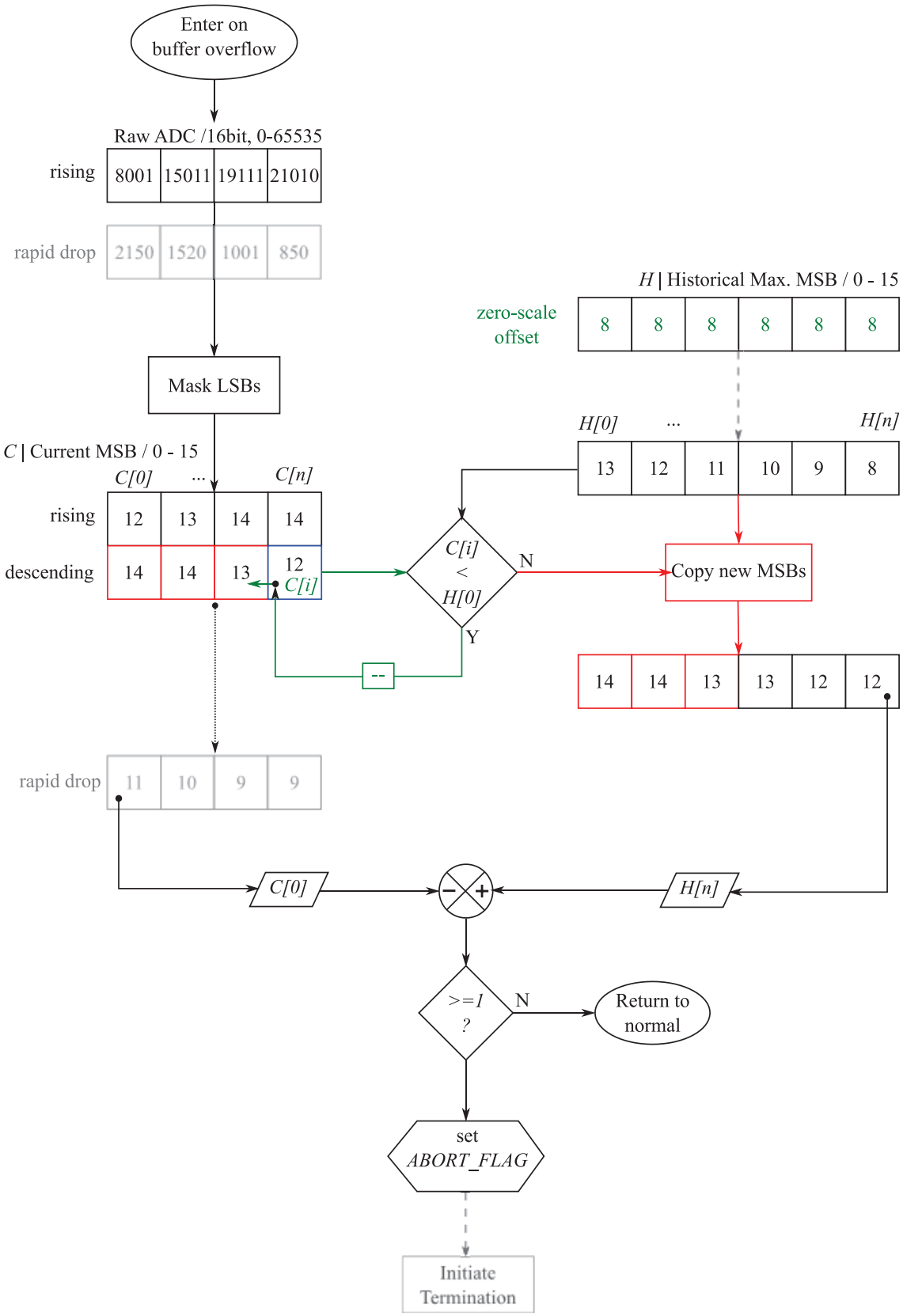

Figure E-3: Flow diagram of periodic rupture detection algorithm

Appendix F

Additional Control System Testing Detail

This appendix provides supplementary data and results for the pressurisation rate control system performance evaluation tests that were described in Chapter 6. Assessment of the repeatable functionality of critical elements of the control system which were not fully addressed in the report are presented. Details of the feedback controller configurations that were used for the tests are provided. Finally, comparison of the feedback controller setpoint error signals for the formal rate control tests is presented to supplement the analyses presented in the report.

F.1 Repeatability Tests

Repeatability tests were repeated three times each for four pressurisation rates as per the control system testing methodology described in (§6.x), with the flow restriction valve ¾ shut. The custom feedback controller design parameters are given in Table F-1. The fitted first-order plant response time measurements were consistent within a 20% range of each other.

The results shown in behaviour is demonstrated by the results shown in Figure F-1 demonstrate predictable and repeatable behaviour, indicating that the feedback control algorithms were working as intended:

- Seamless transition from open-loop to closed-loop feedback control was observed
- Consistent rate tracking of a specified rate was observed for all instances
- No manual intervention was required to supply or purge air supply paths, indicating effective automation of the solenoid valves control
- Successful execution of termination protocols was achieved for all tests upon reaching the termination pressure
- Complete and collated data sets for all tests indicated repeatable automation of the data management between the embedded controller and host interfaces.

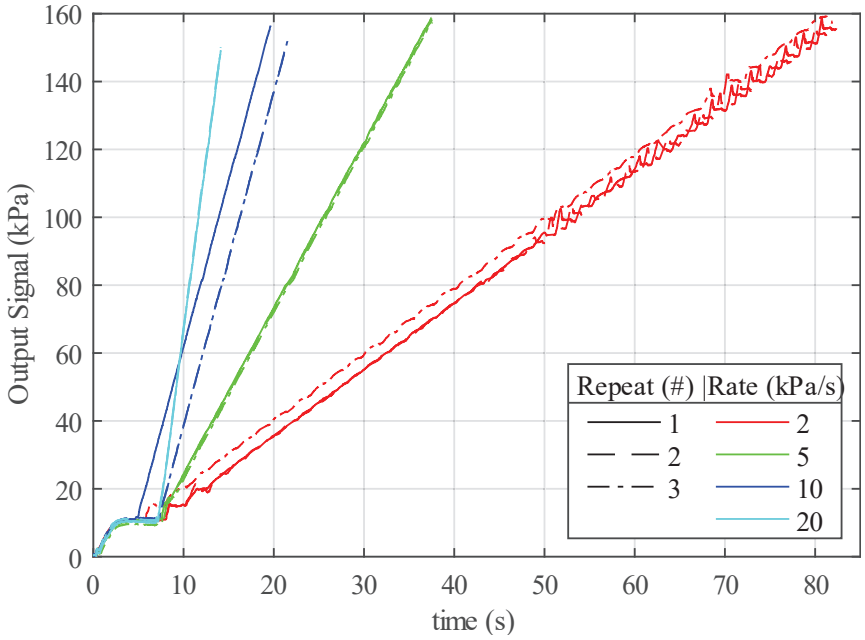

Figure F-1: Control system repeatability test results

Table F-1: Feedback controller parameters for rate control repeatability tests

(#)	Plant Response | τ_p (s)					Controller Gain | K_p (-)				Zero Locus | σ_a (-)			
	Rate (kPa/s)	2	5	10	20	2	5	10	20	2	5	10	20
1		0.94	1.03	0.99	1.02	2.79	3.08	2.95	3.05	1.32	1.27	1.29	1.27
2		0.92	0.94	0.87	1.00	2.72	2.79	2.65	2.99	1.33	1.32	1.35	1.28
3		0.86	0.85	1.01	1.01	2.53	2.50	3.02	3.02	1.36	1.36	1.28	1.28

F.2 Automated Rupture Detection Tests

Results are shown in Figure F-2 for four bulge tests performed on neoprene rubber sheet samples which were intentionally taken to rupture to test the automated rupture detection functionality that was implemented with the bulge testing platform. The associated rapid pressure drop was successfully identified by the embedded rupture detection routine. The termination routine successfully actuated solenoid valves to purge pressurised air, and notification of termination was received by the PC interface to collate test data. The data buffers were also instructed to flush remaining data. However, only one of the four tests produced the pressure drop data which indicated that the efficacy of the final buffer flush was flawed; n worst-case data loss of about 200ms was estimated.

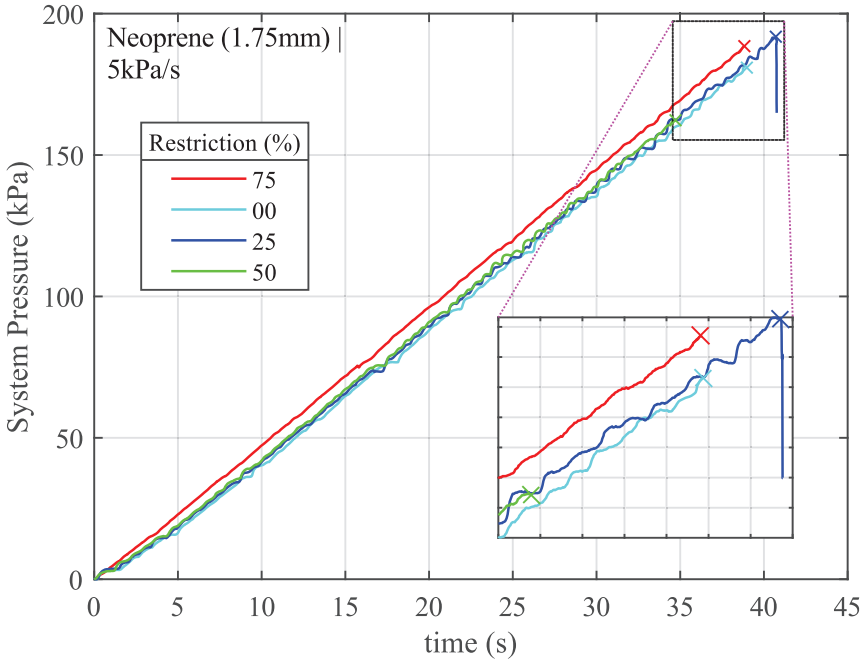

Figure F-2: Practical example of automated rupture detection

F.3 Rate Control Test Data

Supplementary data for the main rate control tests which were presented in (§6.3) are presented subsequently.

F.3.1 System Identification and Feedback Controller Specification

The pretest first-order system identification results are shown in Figure F-3 for the rate control tests. The feedback controller gains and zero-locus parameters were selected for a damping ratio of $\xi = 0.7$ and are summarised in Table F-2.

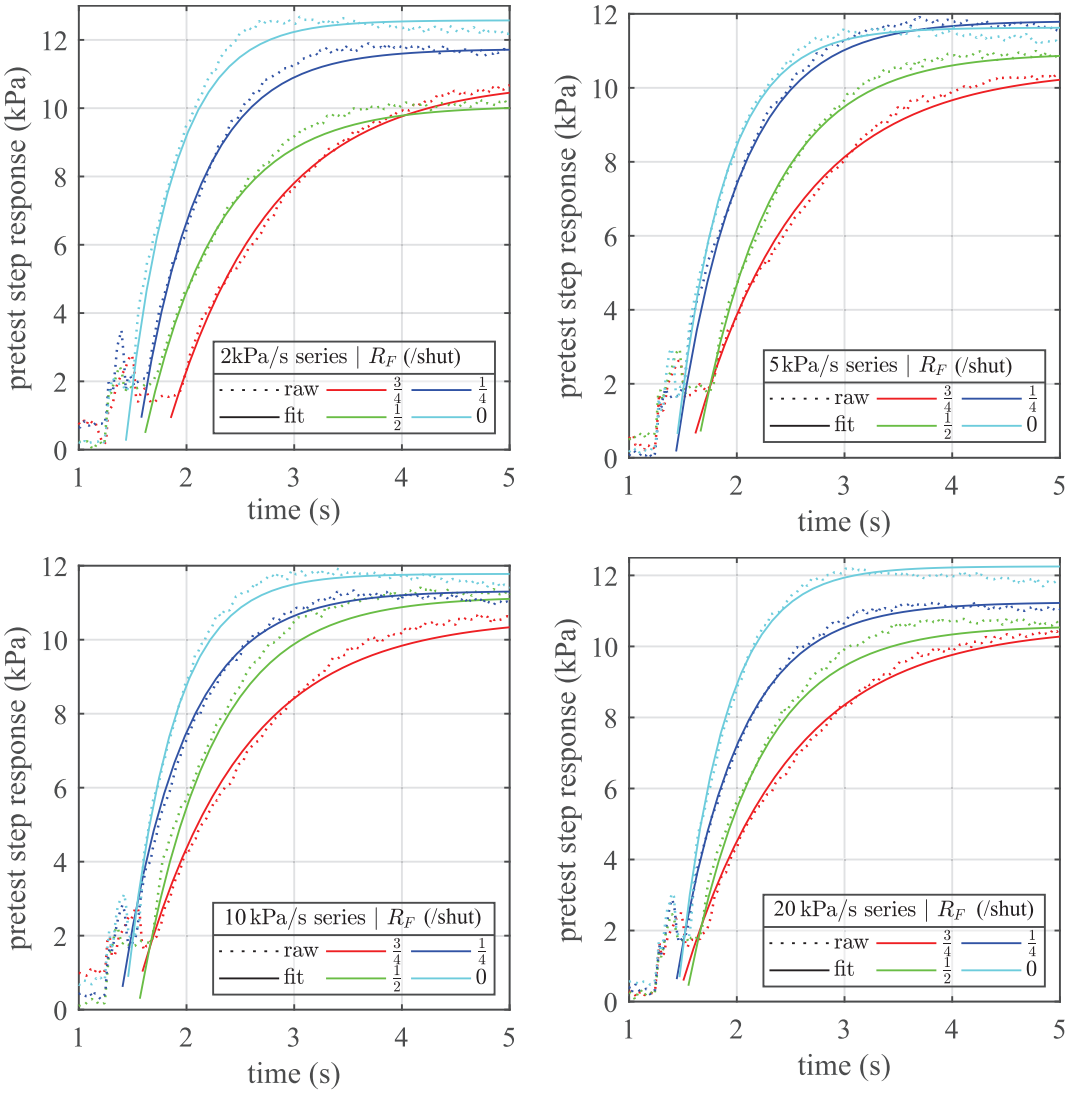

Figure F-3: First-order system identification results for the rate control test pretests

Table F-2: Feedback controller parameters for the rate control tests

R_F	$\dot{p}_t$ (kPa/s)	Plant Response | τ_p (s)				Controller Gain | K_p (-)				Zero Locus | σ_a (-)			
		2	5	10	20	2	5	10	20	2	5	10	20
0		0.43	0.44	0.42	0.43	1.11	1.17	1.10	1.11	1.49	1.49	1.51	1.50
¼		0.55	0.58	0.58	0.58	1.53	1.62	1.61	1.60	1.43	1.42	1.42	1.42
½		0.68	0.68	0.67	0.66	1.94	1.95	1.91	1.89	1.38	1.37	1.38	1.38
¾		0.97	0.98	0.95	1.00	2.87	2.92	2.84	2.97	1.31	1.30	2.1.31	1.30

F.3.2 Absolute Error Signal Comparisons

The absolute normalised error signal analyses for the rate control test are shown in Figure F-4. The constant 4τ lines indicate the predicted time to steady-state assuming first order system response.

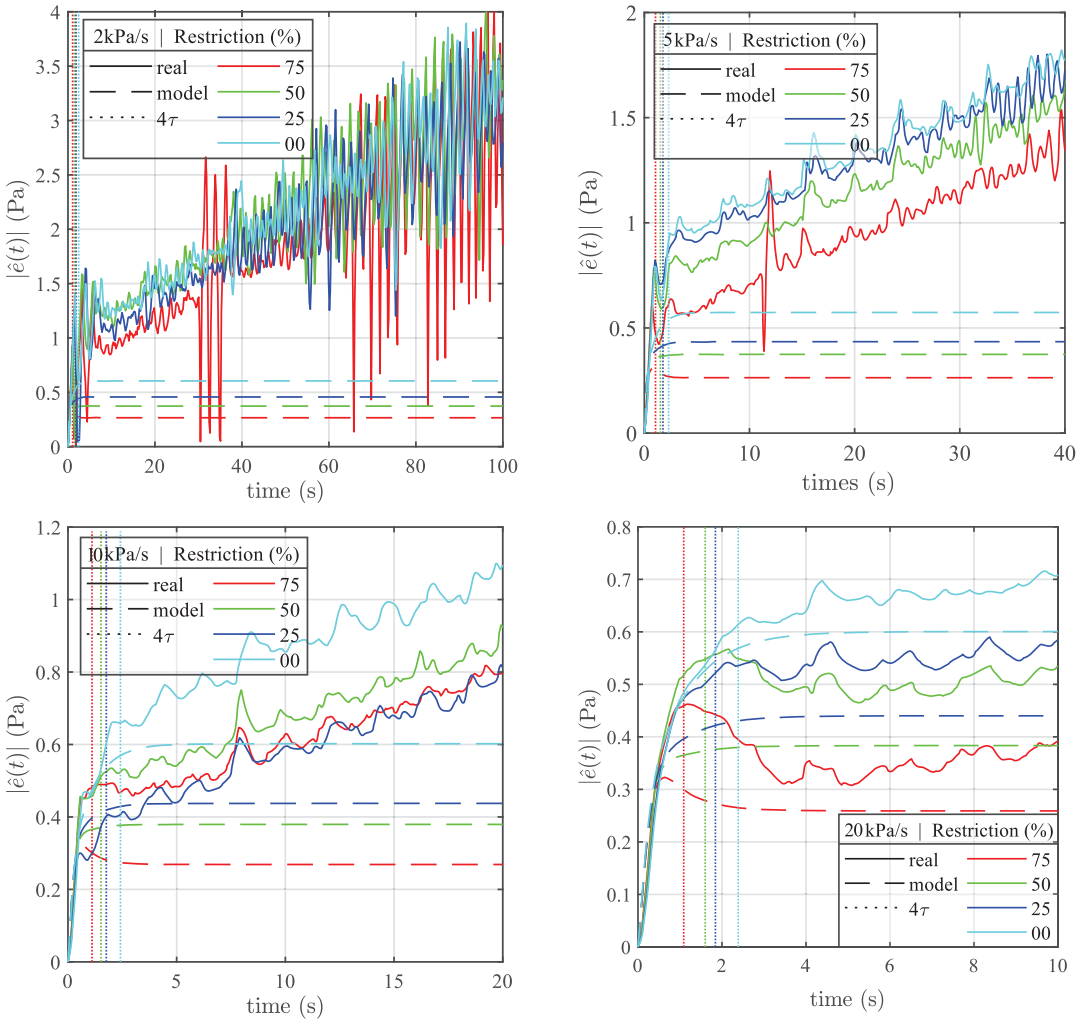

Figure F-4: Absolute normalised setpoint error signal histories for the rate control tests

Appendix G

Additional Mechanical Bulge Testing Detail

This appendix provides supplemental detail and data to support the mechanical material tests that are described in Chapter 6. Tensile specimen geometries that were used for standard uniaxial tensile tests as well as for the equibiaxial bulge tests that were performed using the bulge testing apparatus are presented. Methodology for the *ad hoc* laser displacement sensor measurement of the bulge specimen deflection is described. Fitted material data for uniaxial tensile tests and equibiaxial bulge tests that were performed are presented as well.

G.1 Tensile Test Specimen Geometries

G.1.1 Uniaxial Tensile Test Specimens

The uniaxial tensile tests specimen geometry is shown in the schematic in Figure G-1. The corresponding dimesions are given in Table G-1. Specimens were cut to 'Die A' from the ASTM D412-16 [70] uniaxial tensile test standard for vulcanised rubber and thermoplastic elastomers. Specimens were cut from a single sheet of rubber.

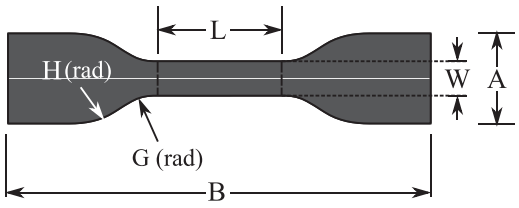

Figure G-1: Uniaxial tensile test specimen schematic. Adapted from [70]

Table G-1: Uniaxial tensile bulge test specimen dimensions

Dim	(mm)
gauge	50
L	59
A	25
W	12
B	140
G	14
H	25

G.1.2 Circular Bulge Test Specimens

The equibiaixal bulge tensile tests specimen geometry is shown in Figure G-2. The corresponding dimesions are given in Table G-2. Solid circular samples with diameter B were cut from the same sheet as the uniaxial specimens and glued to a 4mm thick laser cut wooden masonite annulus.

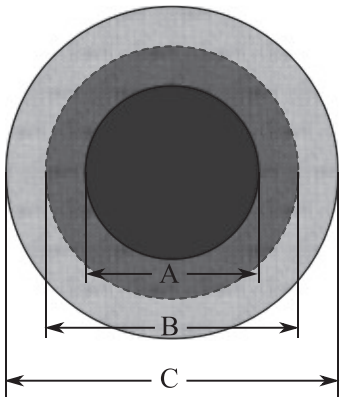

Figure G-2: Equibiaxial bulge test specimen schematic

Table G-2: Equibiaxial bulge test tensile specimen dimensions

Dim	∅(mm)
gauge	50
A	50
B	70
C	90

G.2 Bulge Deformation Measurement Using Laser Displacement Sensor

Vertical bulge apex deflection measurement was performed using an ST Microelectronics VL53L0X infrared laser time-of-flight sensor. The schematic shown in Figure G-3 illustrates a planar, white reflective disc target that was used to cover the sensor's 25° field of view. Table G-3 was extracted from the sensor datasheet and shows the possible range configuration modes for the sensor. The platform target displacement measurement δ was made relative to an initial static range measurement average h made over a period of 5 seconds prior to each use.

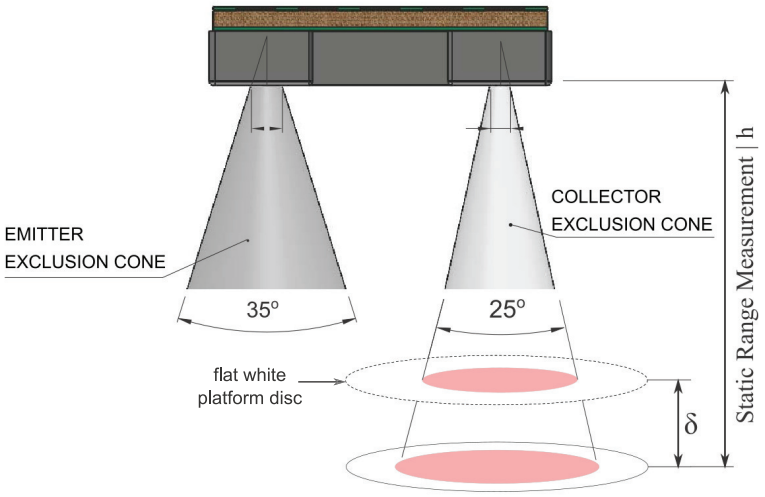

Figure G-3: Schematic of displacement measurement using the VL53L0X time-of-flight laser distance sensor. Image adapted from sensor data sheet [75]

Table G-3: Summary of the configuration modes available for the VL53L0X time-of-flight laser distance sensor. Extracted from sensor data sheet [75]

Range profile	Range timing budget	Typical performance	Typical application
Default mode	30 ms	1.2 m, accuracy	Standard
High accuracy	200 ms	1.2 m, accuracy < +/- 3 %	Precise measurement
Long range	33 ms	2 m, accuracy	Long ranging, only for dark conditions (no IR)
High speed	20 ms	1.2 m, accuracy +/- 5 %	High speed where accuracy is not priority

Interfacing with the sensor's API was done with a dedicated Arduino microcontroller through the open source 'Adafruit VL53L0X Library' for Arduino [76]. High accuracy mode was chosen for measurements up to a maximum range of 150mm. Figure G-4 shows extended static range measurements were that collected on three occasions. Deflection measurement conversions were performed at the prescribed rate of 5Hz. Measurements agreed with the 3% range accuracy specification. The device allowed for a 0.25mm resolution.

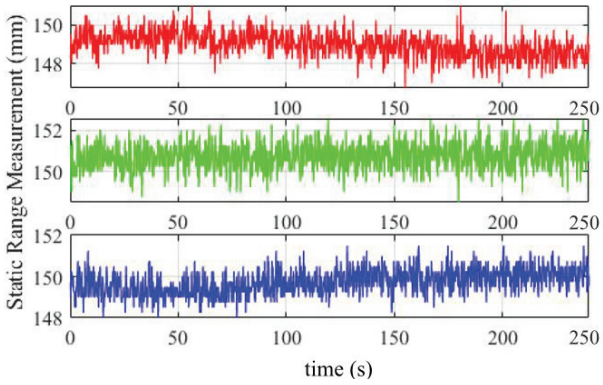

Figure G-4: Static range measurements made using the VL53L0X sensor

Noise caused by poor sensor resolution was smoothed by applying a moving average filter to an N-sample size window. The filter has discrete transfer function

$$\frac{\bar{\delta}(z)}{\delta_{raw}(z)} = \left(\frac{1}{N}\sum_{k=0}^{N-1} z^{-k}\right) \tag{G.5}$$

Some representative pressure-deflection responses are illustrated in Figure G-5.

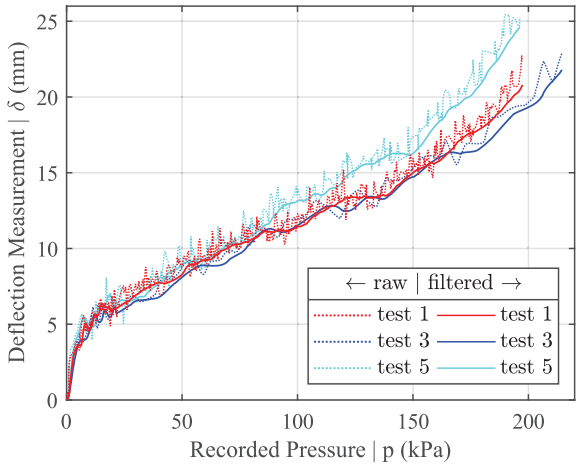

Figure G-5: Comparison of raw and moving average filtered deflection-pressure responses

G.3 Neoprene Mechanical Bulge Tests

Mechanical bulge tests data which is supplemental to the uniaxial tensile tests and equibiaxial bulge test results that are described in (§6.4) are presented. Results presented are for 1.75mm thick neoprene rubber sheet samples.

G.3.1 Mooney-Rivlin Fits for Experimental Data

Mooney-Rivlin data fits for all uniaxial tensile tests are shown in Figure G-6. The individual and average uniaxial model parameter coefficients are presented in Table G-4. Mooney-Rivlin data fits for all equibiaxial bulge test is shown in Figure G-7. The individual and average biaxial model parameter coefficients are presented in Table G-5.

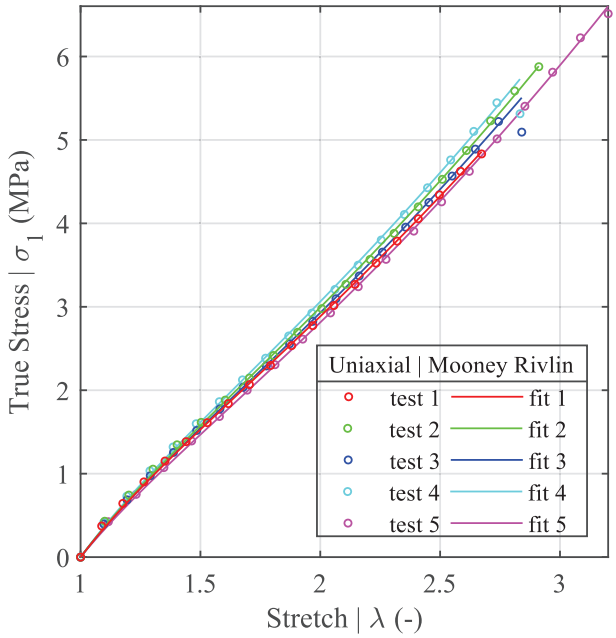

Figure G-6: Comparison of the uniaxial test Mooney-Rivlin data fits

Table G-4: Fitted Mooney-Rivlin coefficients for the uniaxial tensile tests

#	Uniaxial Data Fit [a]	
	C_1 (kPa)	C_2 (kPa)
1	216.5	370.6
2	219.2	436.4
3	210.2	416.4
4	217.1	420.9
5	200.1	424.0
	212.7	413.7

[a] $R^2 \geq 0.995$

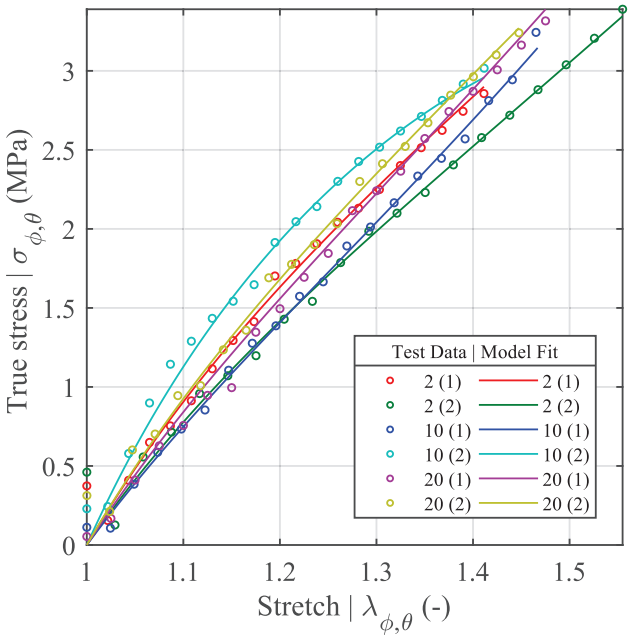

Figure G-7: Comparison of the equibiaxial bulge test Mooney-Rivlin data fits

Table G-5: Fitted Mooney-Rivlin coefficients for the equibiaxial bulge tests

#	Bulge Data Fit [a]	
	C_1 (kPa)	C_2 (kPa)
2(1)	899.8	-33.4
2(2)	730.9	5.6
10(1)	577.6	109.1
10(2)	1410.2	-281.3
20(1)	717.0	66.9
20(2)	881.9	-3.0
	869.6	-22.7

[a] $R^2 \geq 0.985$